# MODELING OF POLYMER BRUSH GRAFTED NANOPARTICLES FOR ALGAL HARVESTING

by

Jason Goins

A thesis submitted to the Faculty and the Board of Trustees of the Colorado School of Mines in partial fulfillment of the requirements for the degree of Master of Science (Chemistry).

Golden, Colorado

Date _____

Signed: _____

Jason Goins

Signed: _____

Dr. David Wu

Research Advisor &

Department Head of Chemistry

## ABSTRACT

Microalgae derived biofuel shows great potential as a replacement to petroleum based fuels. However, industrial scale and economical production of fuel from microalgae suffer from an expensive dewatering step brought on by the organism's specific cell properties. A retrievable, paramagnetic nanoparticle polyelectrolyte brush (NPPB) has been designed as a flocculation agent to provide a low cost method in collecting algal biomass in biofuel production. In conjunction with experiment, subsequent theoretical investigations have been conducted in order to understand experimental observations and inform future design. A strategy has been implemented to provide informative descriptions for the relationship between flocculation agent parameters and dewatering efficiency.

We studied the effect altering the degree of polymerization and monomer charge fraction had on the harvesting efficiency by considering flocculation as the criteria for harvesting. As the number of charges on the polymer backbone of the NPPB is increased, less NPPB concentrations are required to achieve equal harvesting efficiencies. This is a result of needing less NPPB to completely screen the effective charge on the algae surface. However, the Debye length limits the amount of charge on the algae surface one NPPB can screen. Using the free energy calculations for the complete set of pair interactions between the NPPB and the algae, we determined how many adsorbed NPPB were required in order for the force between coated algae to become attractive at some algae surface separation. This corresponded to the NPPB bridging two algae surfaces. NPPB with higher monomer charge fractions and degree of polymerizations led to a stronger bridging bond and larger bridging gap that could outweigh the algae pair repulsion. Optimized structures maximize these effects.

TABLE OF CONTENTS

ACKNOWLEDGEMENTS

First I would like to acknowledge my friends and family. Without their constant support and love I would not be where I am today. Next I would like to thank my research group who has provided a much-needed springboard for me to test my ideas and present my work. The mentorship of my advisor, Dr. David Wu, was always invaluable. Both he and the group continued to challenge me.

I would also like to thank our experimental collaborators, Dr. Liangju Kuang and Dr. Hongjun Liang, for being available to answer my questions and lend their experimental results for comparison. Their help, as well as the guidance from Dr. Matthew Posewitz, have been very helpful in the implementation of this project.

Finally, without financial support I would not have had the opportunity to do any of this. I am very thankful to the United States Air Force who financially supported my work and gave me the opportunity to continue my studies. Also, I would like to thank the Department of Chemistry at Colorado School of Mines University for accepting me into their program and providing the facilities and space necessary to complete my project.

# CHAPTER 1
# INTRODUCTION

The advantages and disadvantages of microalgal biofuel will be discussed in this chapter. An experimental solution to the expensive dewatering step will also be presented and parallel theoretical studies are proposed to understand experimental observations.

## 1.1. Background

The exponential growth of the world population has applied a stress on our natural resources. With a projected 9.6 billion people on the planet by 2050 [1], three imminent and major concerns facing humanity are rising energy demands, sufficient food production, and the damaging effect these strains play on the environment [2]. One proposed solution to these threats is to wane the global dependence of fossil fuels in meeting energy demands, which currently supply about 80% of global energy needs and negatively impact climate change by contributing to the accumulating carbon dioxide in the atmosphere [3]. World leaders instead are encouraging a bioeconomy, which would require the replacement of petroleum-based transport fuels with biomass as an energy source [4]. However, the syphoning of biomass resources away from food supply further handicaps the ability of agriculture to keep up with the population demand [5].

Instead, biofuel derived from microalgae is gaining attention as an encouraging biomass based approach to solving these problems [6,7,8]. Figure 1.1 provides a diagram displaying the current harvesting model for the production of biofuel from microalgae. Like other biomass liquid fuels, microalgae biofuel is a renewable and carbon neutral alternative to fossil fuels. Furthermore, the end product can be used in existing technologies, avoiding the hurdle of overhauling the entire transportation infrastructure. In addition, the biology of microalgae cells endows to it additional advantages over other biodiesel sources, which we outline here.

Microalgae are photosynthetic unicellular microorganisms that can grow in either fresh or salt water. Different species of microalgae are well adapted to even thrive in harsh environments [9]. Therefore the creation of microalgae farms does not compete with agriculture biomass for arable land. Microalgae species also have a great propensity to grow at rates exponentially faster than other forms of biomass, with the ability of doubling their biomass 1-3 times per day [9,10]. Also with a high protein content inside the cell, Figure 1.1 shows that an offset in the cost of biofuel algaculture are high valued

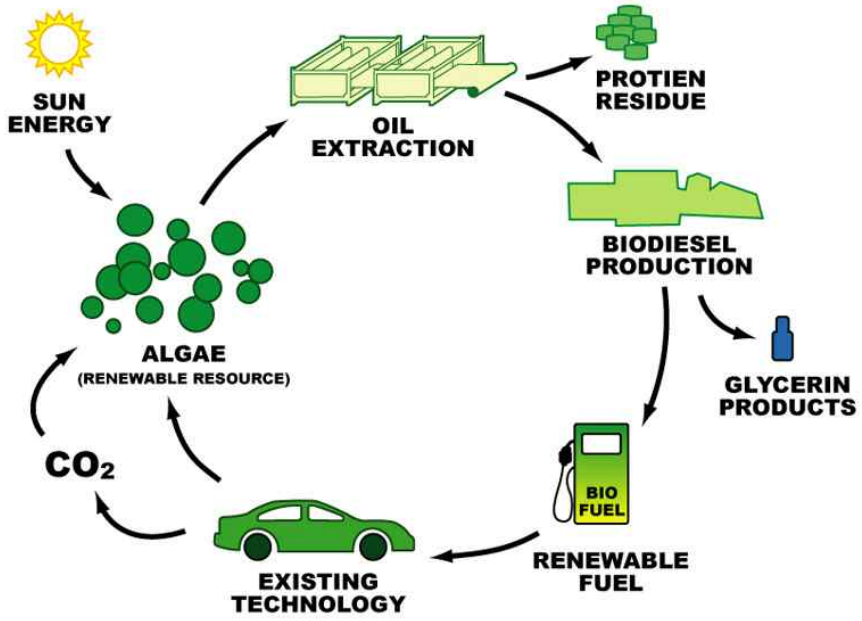


Figure 1.1. Algae to biodiesel cycle. Taken from [11].

derivatives of the protein that can be converted to plastics or biochemicals [6,12]. Finally, though not exhaustively, microalgae are more efficient producers of lipids that serve as the precursors to liquid fuel. Unlike other biomass organisms, microalgae do not waste nutrients or space on large, non-photosynthetic parts such as a stem. This and other intrinsic factors allow microalgae to produce more oil per area and mass than other biofuel sources. While a lipid content excess of 80% (by wt.) has been reported for several strains of algae [13], 20-50% values are normal for many species [14]. With this in mind, corn requires roughly 300 times the land area to produce an equivalent amount of oil as microalgae assuming 30% lipid content by weight.

Despite all this potential, algae biodiesel must become cost competitive with petroleum-derived fuels in order to take a significant market share in the transportation fuel market. In order for this to happen, a three-fold increase in the scale of production followed by a ten-fold decrease in its cost is required [6]. Figure 1.2 outlines the challenges facing scientists today in achieving this goal. While commercial sized production processes are beginning to garner attention [15,16], a major inhibitor is the cost of down-stream processing [17]. More specifically, the dilute nature of microalgae suspensions and the small size of the individual cell create a costly, energy intensive barrier for dewatering and subsequent harvesting of lipid content [18,19,20]. Hence large amounts of water are needed to be pumped in the production process in order to create enough biomass material for industrial scale energy production. Simple dewatering techniques such as screening and filtration are also unfeasible. Instead, to simplify the dewatering process microalgae cultures must be concentrated by a factor of 100 times (see Figure 1.3) to an algae slurry. Flocculation is a popular technique to achieve this required pre-concentration.

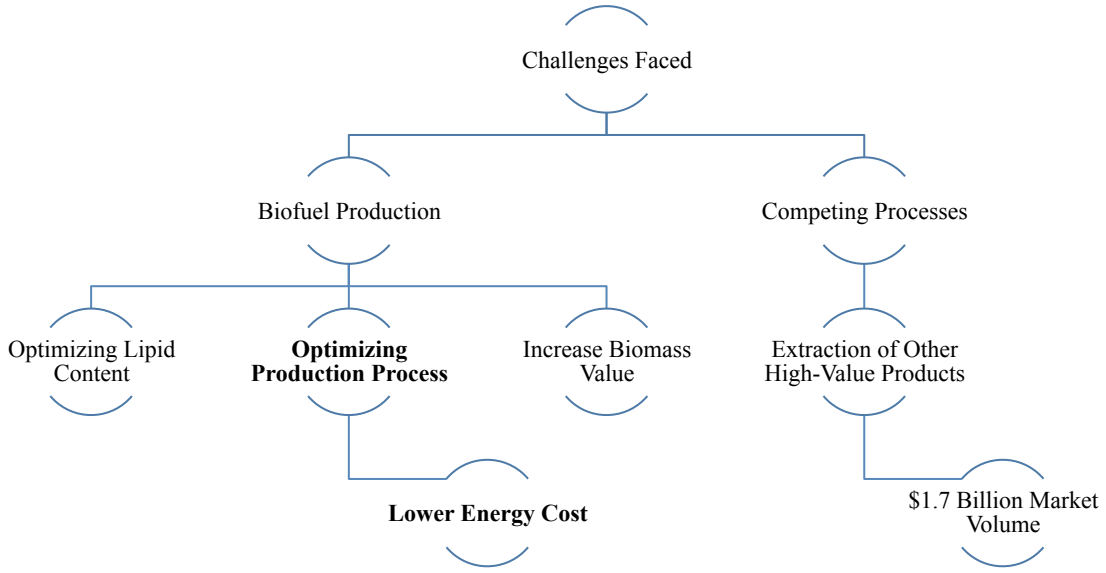


Figure 1.2. Breakdown of the current challenges facing the microalgae biodiesel industry from being cost competitive with petroleum fuels. In bold is the section that garners our attention. Adapted from [6].

Flocculation is defined as the process of forming larger aggregates from dilute cultures and provides several advantages over other conventional dewatering schemes. Flocculation is both quick and efficient, and is free of energy intensive steps during the concentration process. Furthermore, flocculation agents can be synthesized from inexpensive and readily available material. Schlesinger and coworkers [21] have shown that the amount of agent needed is logarithmically proportional to the number of algae cells and that for denser cultures the cost of flocculant should be able to reach values of less than a $1.00 per ton of algae. However, detractors of flocculation emphasize that the process requires endless material costs, energy intensive separation of buoyant algal flocculant and possible downstream contamination of the product. Researchers have investigated a wide variety of flocculation methods to solve these problems. Many of these solutions involve flocculants that are designed to screen the like-charge repulsion between microalgae surfaces that deter the cells from forming aggregates [22].

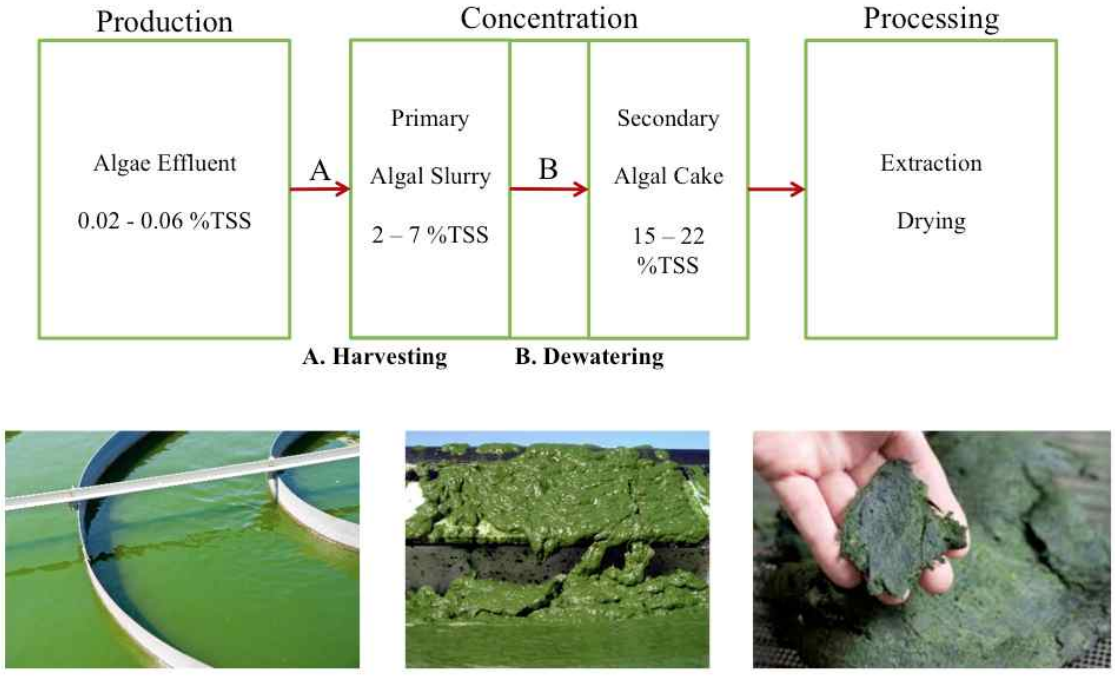


Figure 1.3. The concentration of microalgae cultures prior to lipid ex-traction. %TSS stands for total suspended solid. Pictured at bottom from left to right is the original algae effluent, followed by the algae slurry and then algal cake. Adapted from [18].

In the context of these attempts, our experimental collaborators have chosen to study the efficacy of using a nanoparticle cationic polymer brush [23]. We hypothesize that the cationic charge along the polymer backbone serves to screen algal surface like-charge repulsion, allowing flocculation, while the solid nanoparticulate core provides low-cost opportunities to retrieve and reuse the agent in a closed loop process. The design of such an agent must follow from these requirements and include low cost materials and synthetic methods.

Figure 1.4 shows the three-component design of the flocculation agent. Paramagnetic iron oxide nano-crystals form the solid core. These nano-crystals are readily prepared at large scales [24] and provide an easily scaled process for retrieval via magnets.

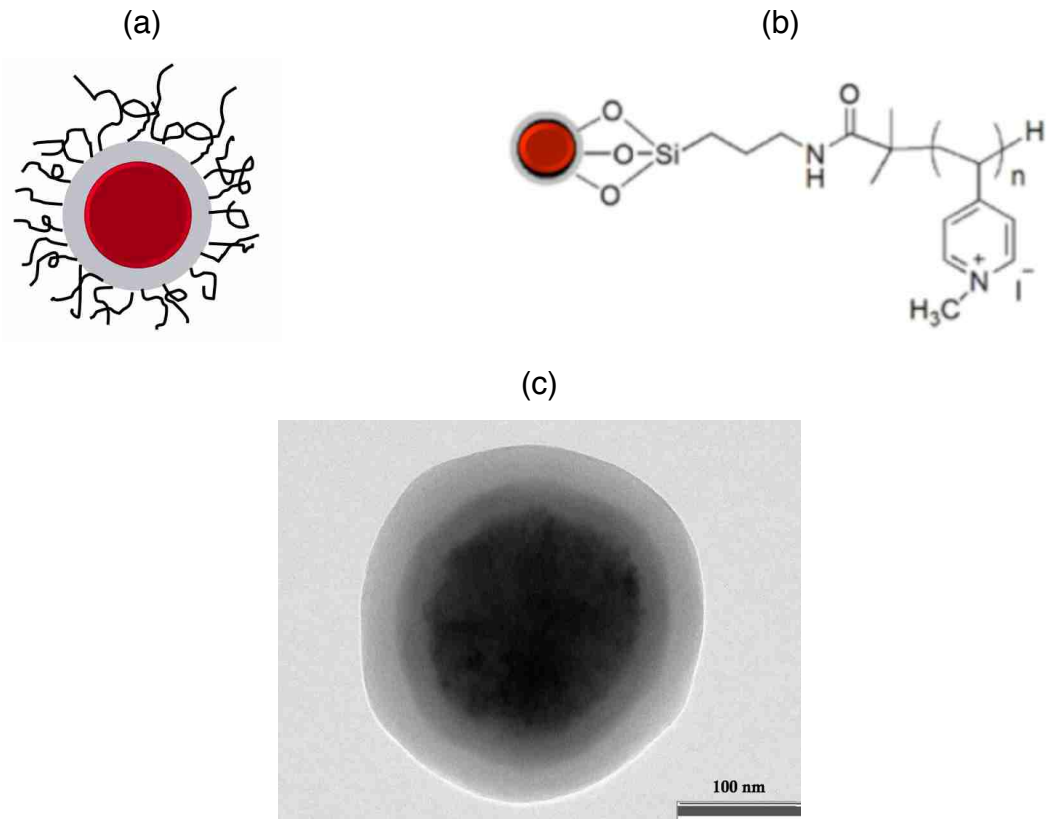


Figure 1.4. The flocculation agent. (a) Three-component design of the flocculation agent. From inside to out: paramagnetic iron oxide nanoparticle, silica coat, and cationic polymer. (b) Chemical structure of the agent: $Fe_3O_4$@$SiO_2$@P4MVP. (c) TEM image of a cross section of the nanoparticle flocculant.

The silica layer prevents the iron oxide core from leaching while exploiting well-studied silane-polymer chemistry for the grafting of the cationic polymer to the core. The cationic polymer, poly(4-vinyl-N-methylpyridine iodide) (P4MVP), is grafted to the silica layer via the “graft to” approach where the polymers are first grown individually and then an end-functionalized chain attaches onto an active site on the surface. The activity of the cationic charge on P4MVP is pH dependent, which allows reversible binding to a negatively charged algae surface.

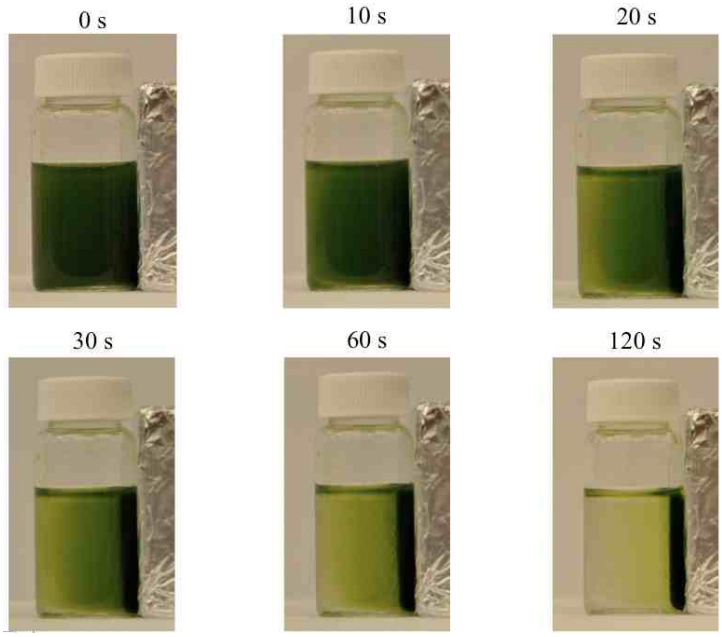


Figure 1.5. Experimental testing of the flocculation agent [23]. The set up involves *Chlamydomonas* algae and flocculation agent in a capped vial placed next to a magnet. At time 0 seconds the flocculation agent is added.

This design successfully fulfills the desired requirements and is both effective and efficient. Figure 1.5 shows a lab scale test of the flocculation agent and displays the effectiveness of the flocculation agent in concentrating algae. In less than two minutes, almost all the algae are precipitated out of solution. Since only the nanoparticle is magnetic, algae-agent binding must have occurred. In another experiment, our experimental collaborators measured the concentration of algal cells before and after harvesting by the flocculation agent using a Z2 Coulter cell and particle counter. Over 99.5% of the cells were dewatered using a mass ratio of 24:1 algae to flocculation agent, showing the efficiency of the process. While these measurements were made in lab-scale, the de-

sign has facile scale up potential. A proposed model involves a continuous cycle where the nanoparticle polyelectrolyte brush is mixed into a flow of algal cultures and allowed to attach to the algal cells. The clusters of flocculant-algae are then precipitated out via an external magnetic field and recovered by controlling the pH.

Due to the tailorable properties of the polymer brush, it serves as an excellent candidate to study how changing different experimental parameters affects the harvesting efficiency of algal cells (see Section 1.3 for a brief review on polymer brushes). We can then use what we learn from these experiments to optimize the process. Experimentalists are able to control the chemical composition of the monomer units along the chain, molecular weight, grafting density, polymer length, branching, and bridging. All these parameters can be tuned to give the brush distinct and well-controlled functionalities.

Figure 1.6 summarizes experimental results where different structural parameters of the flocculation agent were altered. We see in Figure 1.6a that as the degree of polymerization is increased, the optimal dosage required to reach almost 100% harvesting efficiency is lowered. Once the degree of polymerization is greater than 200, this trend plateaus. There must be some requirement with a cutoff around that value to cause little change in the harvesting efficiency once the degree of polymerization goes from 198 to 245. In other words, once a degree of polymerization reaches approximately 200, adding more repeating units onto chains results in little difference in being able to harvest algae cells. Furthermore, from the controls we see that higher harvesting efficiencies require the brush structure and not just free polymer or the nanoparticle core. Experimental observation of increased harvesting efficiencies must be due to changing the structure of the brush. A similar phenomenon is seen when varying the monomer charge fraction at constant degree of polymerization in Figure 1.6b. Increasing the charge fraction results in higher harvesting efficiencies at lower flocculation/coagulation agent doses. A plateau is reached once the monomer charge percent reaches 75% since there is little difference in the experimental results between 75% and 100%. Any further analysis that attempts to explain experiment should be able to explain the results presented in Figure 1.6. This requires providing reasoning for the differences in the op-

timal dosage required for higher harvesting efficiencies close to 100% when the brush degree of polymerization and charge fraction is changed and the plateauing observed at certain values.

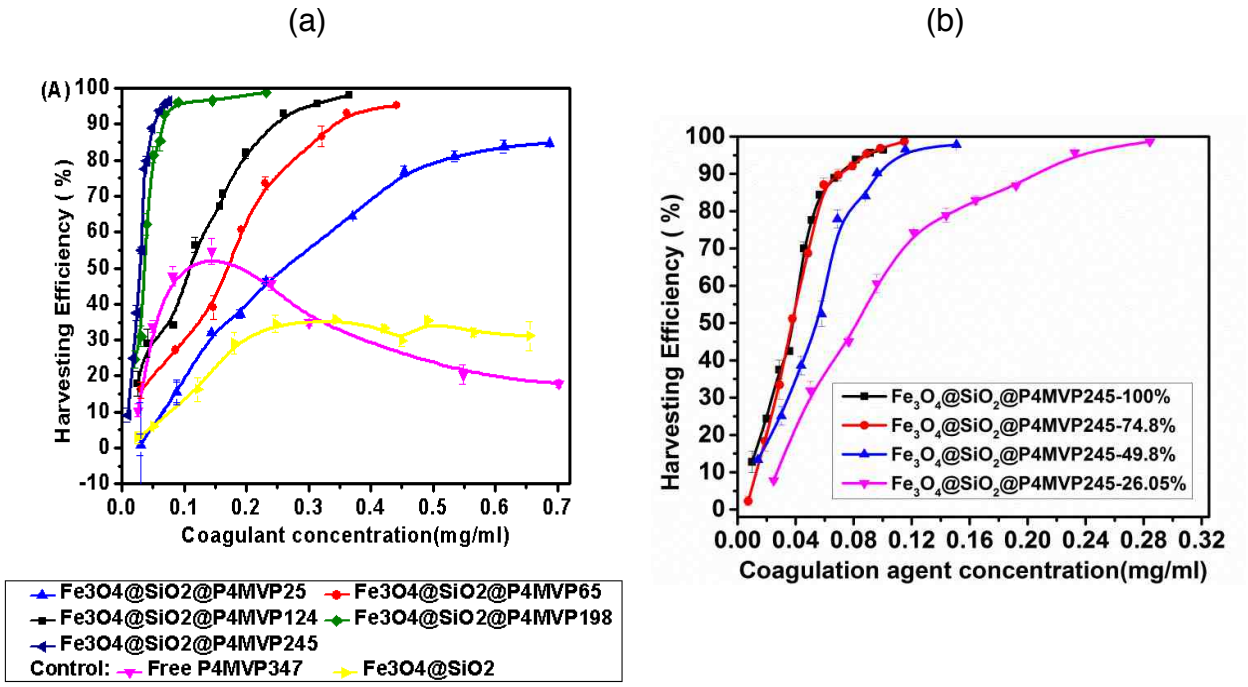


Figure 1.6. Experimental measurements of harvesting efficiency [23]. (a) Harvesting efficiency as a product of varying the degree of polymerization. (b) Monomer charge fraction effect on harvesting efficiency. Percent values represent the percent of monomers charged per chain.

## 1.2. Goals and Approach

In conjunction with experiment, theoretical models were developed and implemented to understand microalgae dewatering directed by a nanoparticle polyelectrolyte polymer brush (NPPB). More specifically, the main goal of this theoretical work was to elucidate possible relationships between structural parameters of the NPPB (degree of polymerization, fraction of monomers charged, size of NP core, etc.) and the harvesting efficiency of algae cells by NPPBs. These theoretical models will allow us to conduct a more informed discussion of experimental observations. In addition, they will give us the tools to not only discuss but also understand these observations through the scope of the fundamental physics of the system. Finally, and most significantly, this parallel theo-

retical treatment will provide information and prediction useful to the optimization of the experimental process. These benefits all advance the ultimate project goal of achieving highly efficient dewatering of microalgae at a low cost. In a more general scope, our findings can provide a framework for the extension of this brush into other research areas that currently exploit the polymer brushes' adaptability to suit a wide variety of functions and environments such as the development of bioelectronics [25] or health sciences [26,27,28].

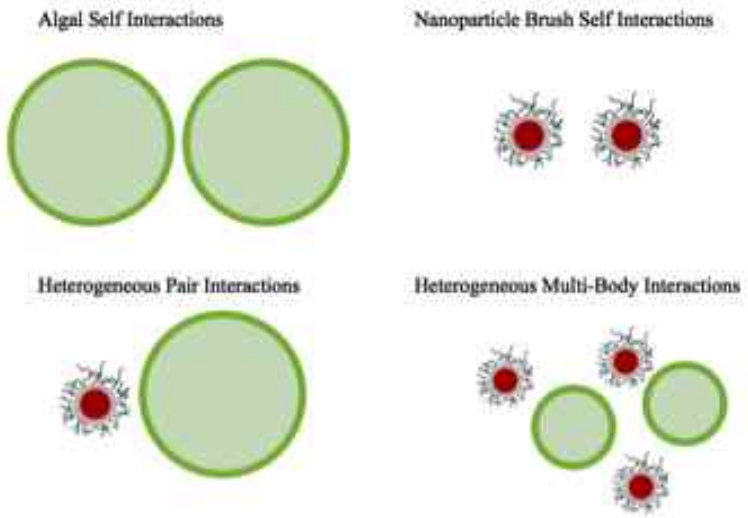


Figure 1.7. The relevant molecular bodies in our system and their possible interactions with each other. Note that the schematics are not shown to scale.

To complete these goals, we devised a strategy that breaks the task down into two subtasks. The first subtask was to analyze the interaction potentials between the relevant bodies (Figure 1.7). The second subtask was to find a relationship between these potentials and the harvesting efficiency. Consequentially, our model must allow us to complete these tasks in the scope of our main goals outlined above and explain the results in Figure 1.6. The method and calculation of interaction potentials for the algal self interactions are explained in Chapter 2, while methods and calculations for interactions involving polymer brushes are elucidated in Chapter 3. Chapter 4 uses these pair interaction results to determine multi-body interaction potentials and give quantitative predictions of harvesting efficiencies. A direct comparison between theoretical and ex-

perimental observations is conducted in this chapter as well. Finally, a summary of the general conclusions, recommendations to experiment, and future work is outlined in Chapter 5. Before we continue on these investigations, a brief review on polymer brushes is provided to give background to future discussions in Chapters 3 and 4.

## 1.3. Introduction to Polymer Brushes

The design and synthesis of polymer brushes has become more accessible to a wide range of scientific fields. Consequentially, the tailorability of polymer brushes has garnered interest as an intuitive approach to bottom up design in the development of nanoscale materials. The development of polyelectrolyte brushes, polymer brushes with charged chains, is especially attractive since it gives scientists an extra parameter to tune and an interface for electrical systems. As is such, theoretical methods surrounding these brush architectures have been used to understand experimental observations and to inform future design of brushes with novel functionalities. In this review, the diversity of polymer brush applications will be introduced and the concepts and utility of the Flory argument for understanding polymer brushes, particularly polyelectrolyte brushes, will be covered.

### 1.3.1. The Polymer Brush, an Introduction

As novel polymer synthesis techniques have been developed that allow more widely accessible approaches to designing polymers, the field of pure polymer chemistry has started to give way to a multidisciplinary interest in polymer science. Such fields as material science and engineering have adopted the special chemistry and physics of polymers into their tool belts. The ability to control each piece of a polymer substance via the monomer unit has made polymer science an intuitive and attractive approach to bottom up designing of materials with desired properties.

The development and production of nanomaterials is an area where polymer science has been central in problem solving. In particular, polymer brushes have incurred great interest in their ability to bridge different types of chemistry, such as in the coupling of inorganic and organic materials.

Polymer brushes are characterized by the incorporation of polymers onto a substrate at a high enough density such that the chains extend outwards from the surface. In general, the flexible polymer chain takes on a random walk conformation that minimizes its free energy [29]. The distinction then with the polymer brush is that the grafting density, i.e. the distance between two adjacent polymer chains, is constrained such that this dimension is much smaller than the linear dimension of the random walk. These polymer chains are constrained to the solid surface either through covalent linkage or adsorption [30].

As mentioned above, an intrinsic value of polymer brushes in nanoscale design is their ability to integrate different chemistries. The tethering of polymer brushes to gold and silicon are well studied and served as the pioneering solid substrates for brush synthesis. Since these initial studies, a wide diversity of organic, inorganic and even polymer substrates have been linked to polymer chains to create brush architecture. The list includes but is not limited to cellulose [31], poly(vinyl chloride) [32], carbon nanostructures, and steel [33].

Not only are a wide variety of substrates usable, probably the most notable merits of polymer brushes are the tailorable properties of the polymer layers themselves. Scientists are able to control the chemical composition of the monomer units along the chain, molecular weight, grafting density, polymer length, branching, and bridging. All these parameters can be tuned to give the brush distinct and well-controlled functionalities.

### 1.3.2. Applications

Original applications of polymer brushes focused on either steric or electrostatic stabilization of colloid solutions by polymers [29]. While this field is still relevant today, the uses of polymer brushes have diverged greatly.

One example is the current subject of this thesis investigation. In the effort to make the production process of the conversion of microalgae lipids to biofuel more scalable and inexpensive, a nanoparticle polyelectrolyte polymer brush (NPPB) that is pH insensitive and magnetic has been designed to induce the flocculation of dilute algae

solutions [23]. Upon addition of the NPPB, the stable solution of microalgae begins to flocculate around the brushes and the aggregate is irreversible around processing temperature. This concentrated mixture can then be transported via magnet and the NPPB can sequentially be desorbed and retrieved from the microalgae by altering the pH, creating a closed looped harvesting system.

In the development of bioelectronics, the technology requires the creation of an electrical signal from biochemical stimuli. Polymer brushes can serve as a go between for biological material (such as enzymes) and inorganic electronic material. In one instance, poly(4-vinyl pyridine) (P4VP) brushes were functionalized with an inorganic redox group that was active only in the presence of a specific combination of enzymes [25]. The active P4VP brush was able to oxidize NADH. Hence, the oxidation of NADH was controlled by biochemical stimuli, utilizing an inorganic oxidizing agent coupled to a polymer brush.

In another case, a polymer brush inside the human body was extensively studied to understand how defects of the mucus clearance pathway inside the human body lead to certain lung diseases [26]. The role of the pericilliary layer (PCL), comprised of long polysaccharides, was viewed in the context of a polymer brush in presenting a model of the airway surface.

The health sciences have found a particular niche for polymer brushes in drug delivery, biosignaling, and bioimaging. In the instance of bioimaging, polymer brushes were used for *in vivo* imaging and tracking of tumor cells in mice [24]. The researchers grafted poly(ethylene glycol) to conjugated polyelectrolytes and then complexed the molecule with the anticancer agent, cisplatin. These nanoparticles could then locate and attach themselves to cancerous cell and be imaged *in vivo* using a fluorescent imaging probe, in addition to being used as drug delivery systems. Another bioimaging example can be found in the production of “smart” microgels. Microgels with gold nanocrystal cores were synthesized using poly(N-isopropylacrylamide) grafted to the surface of the gold with a high degree of inter-chain bridging [28]. This thick brush (or microgel) was temperature sensitive in that it would stretch or shrink given a change in the thermal environment. This allowed for a tunable spacing between gold nanocrystals, creating a

"smart" microgel that exhibited tailorable surface plasmon resonance between the gold nanocrystals.

### 1.3.3. Flory Argument

Of particular interest to us are polyelectrolyte brushes where the anchored polymer chains are charged. Polyelectrolyte brushes, as seen in examples from Section 1.3.2 are useful in biology where cells surfaces are typically equipped with densely packed macromolecules containing ionizable groups. In addition, ionizable groups on the polyelectrolyte chains allow the brush to have functionalities that are pH sensitive. Finally, the electrostatic interactions inside the brush layer allow scientists to have another intermolecular force to exploit.

In order to understand the properties of these polyelectrolyte brushes, the Flory argument will first be examined. Results for charged structures will be compared with those for neutral brushes. These particular models are useful in explaining properties relying only on the brush height. However, scaling concepts do not inform us about the system inside the brush. Self-consistent field theory (SCFT) for polymers serves as a theoretical device for filling this gap. Chapter 3 introduces SCFT in more depth and rigorously outlines the theoretical derivation. For now, we will simply investigate the behavior of polyelectrolyte polymer brushes using the Flory argument.

The physics of a polymer chain can be well understood in the context of a balancing act of its free energy. Here, the consolidation of the celebrated scaling theories of Alexander and de Gennes given by Milner [29] and Pincus [34] for a neutral brush will be presented. First consider a flexible polymer chain of degree of polymerization $N$, monomer units measured by the statistical length $b$, and surface coverage density $\sigma$ with a brush height $L_p$ from the surface. If one were to walk along the chain backbone, he/she would see the chain attempt to configure itself in a random walk conformation in order to maximize its configurational entropy. The typical linear dimension for such a walk is given by the radius of gyration, $R_g$, and results in chains that are densely packed around the surface. The elastic nature of the polymer chain can be quantified by the

spring constant $k = k_BT/R_g^2$ (i.e. doubling the thermal energy increases the linear dimension four fold).

Counter to the configurational entropy are the maximization of favorable interactions with the solvent and the minimization of unfavorable contacts between chains. These two free energy arguments are contained within an excluded volume term *v*. For solvents that form favorable contacts with the chain, *v* is negative and stretching of the chain backbone results. For poor solvents, *v* is positive and the chain begins to favor monomer-monomer interactions over solvent contacts, resulting in contraction. The term theta solvents arise when *v* is zero.

The Flory free-energy cost per chain follows (tilde represents missing constants of order unity):

$$\Delta F \sim k_B T \left[ \frac{3L_p^2}{2Nb^2} + vN\left(\frac{N\sigma}{L_p}\right) \right] \qquad (1.1)$$

Eq. ( 1.1 ) above can be thought of as the energy cost required to add another chain to the system. The first term considers the random walk configuration, while the second term accounts for the maximization of favorable contacts along the backbone. Minimization of Eq. ( 1.1 ) with respect to $L_p$ gives the following scaling relation:

$$L_p \sim N(v\sigma b^2)^{1/3} \qquad (1.2)$$

We can compare this linear dimension of the brush with the linear dimension for a free polymer chain $R_g$, which scales as $N^{1/2}$. The brush length scales $N^2$ times greater than its random walk confirmation. As pointed out by Milner, this signifies that the properties of the polymer brush are expected to have different properties from its untethered counterpart.

Now consider a polyelectrolyte brush with *f* fraction of monomer units charged along the backbone [35]. Pincus [34] shows that the increased stretching of the chain mainly arises from the entropic cost to confine the counter ions inside the brush layer rather than the self-avoiding nature of the electrostatic interactions along the backbone. In order to stabilize the strong electrical charges along the chain, the counter ions will

remain inside the brush layer and hence create an osmotic pressure counter to the substrate surface. The electrostatic contribution to the free energy cost in Eq. ( 1.1 ) then is:

$$\Delta F_{el} \sim k_B T (f \emptyset \ln \emptyset) \quad (1.3)$$

where $\emptyset \equiv Nb^3/L_p\sigma$. In the case where the electrostatic contribution outweighs the excluded volume effects, the brush height arises from a balance between the elastic and electrostatic properties. In this regime $L_p$ retains its linear relation to $N$, but with an additional constant:

$$L_{pb} \sim f^{1/2} Nb \quad (1.4)$$

For small $f$ and large $v$, the scaling of $L_{pb}$ reverts to Eq. ( 1.2 ). Dividing Eq. ( 1.4 ) by Eq. ( 1.2 ) gives the relationship of a polyelectrolyte brush length with its neutral counterpart:

$$\frac{L_{pb}}{L_p} \sim \frac{f^{1/2} b^{1/3}}{(v\sigma)^{1/3}} \quad (1.5)$$

When the monomer dimension and the surface coverage density are on the same order (which is typically the case), it is evident that the electric charges along the chain result in the stretching of the brush. However $0 < f < 1$, such that in the case where excluded volume interactions dominate the height of the polyelectrolyte brush is much more likely to scale according to Eq. ( 1.2 ).

It is important to note that the properties of the polyelectrolyte brush were considered in salt-free conditions. Upon the addition of salt, the electrostatic interactions inside the layer are screened and the brush loses its polyelectrolyte character. This allows scientists to have a switchable parameter in controlling the behavior of polyelectrolyte brushes, but must be considered in environments with high ionic strength when using theory to describe experimental results.

# CHAPTER 2
# DETERMINING THE INTERACTION POTENTIAL FOR ALGAE CELLS

Determination of the algal pair interactions will lead to greater understanding of why cultures form stable suspensions in solution. From this insight we can hypothesize why the designed flocculation agent induces aggregation of the cells. The mechanism to perform this analysis will be presented in this chapter.

## 2.1. Setting up the Problem

The determination of biological interactions is a complicated procedure due to the dynamic behavior of organisms [36]. As an example, consider the system we wish to model in Figure 2.1a. Microalgae in this diagram are anisotropic and not all of the same exact size. Some of the cells actually consist of two cells surrounded by an outer cell wall. A balance must be made between exact description of each of the discrepancies and performing feasible calculations of the system. In an effort to model most algae – algae interactions in our system we will consider an interaction between two average algae cells. Thus, certain approximations are required in providing meaningful calculations to quantify these interactions. To develop a useful model we must first strive to understand this “average interaction” between algae.

The most prevalent forces describing interactions between biological cells can be divided into six categories: van der Waal, electrostatic, steric, depletion, hydrogen bonding, and hydrophobic. For algae cells, there is no hydrogen bonding. Furthermore if the algae surfaces were hydrophobic they would precipitate out of solution in order to minimize water contact. There has been no evidence of this phenomenon occurring and thus we can eliminate any hydrophobic influence in modeling an algae – algae interaction. Attractive depletion forces are entropic in origin and hence depend on temperature and local mixture concentrations. The depletion force in microalgae suspensions arises when smaller, nonadsorbing particles (such as a polymer) are introduced into the sys-

tem causing the large cells to sterically avoid them [37]. However, there is no significant source of depletants in a solution of algae that would cause aggregation on a macroscopic scale. With steric repulsion, the typical range of force is governed by the thickness of the adlayer on the microorganism surface. Generally, this extracellular mesh of proteins and polysaccharides generally extends between 1-10 nm from the surface [38]. Relative to the size of the algae (8 – 10 μm in diameter), this length scale is quite insignificant. We choose to ignore this force since the typical cell concentrations (see Figure 1.3 in Section 1.1) required for cell harvesting still do not approach this small of length scales. The van der Waal force measures the interaction between fluctuating microscopic dipoles and scales as the inverse of the separation between the two dipoles to some power depending on the relative distance. For our macroscopic cells, we will consider the van der Waal forces from all the microscopic dipoles.

(a) (b)

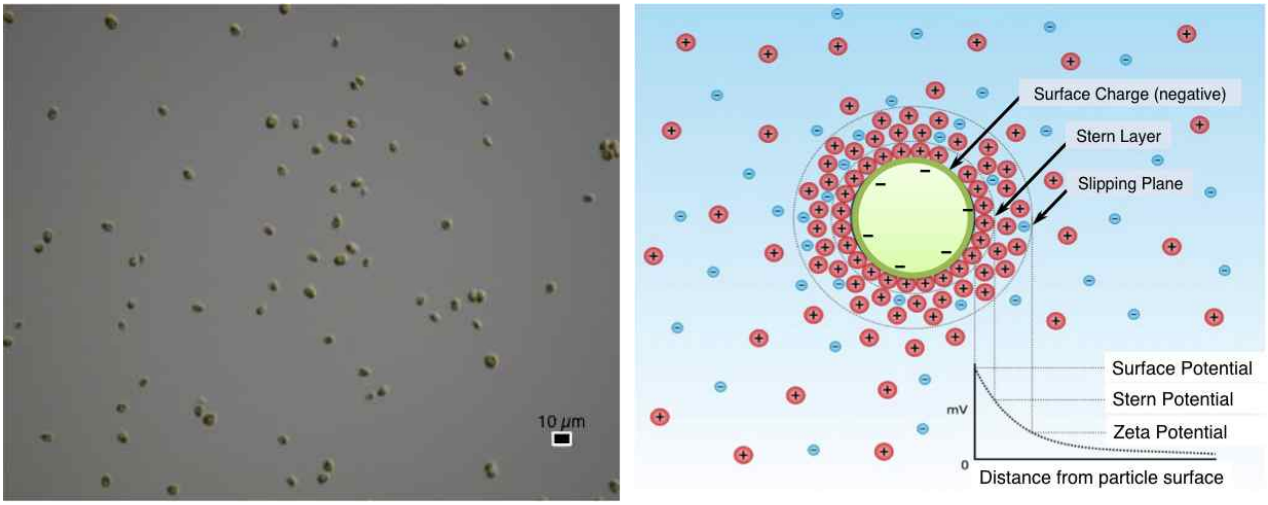


Figure 2.1. (a) Microscope image of *Chlamydomonas reinhardtii* [23]. (b) Electric Double Layer formation (modified from [39]).

Finally, we set out to understand the electrostatic interactions. Most microalgae are negatively charged in solution due to dissociation of carboxylic acid groups at the surface at pH's above 4-5 [40]. In order to stabilize this charge in solution, an adsorbing plane of oppositely charged counter ions form along the surface (see Figure 2.1b). This is known as the Stern Layer. Outside of this Stern layer a mobile layer of ions form that

are electro-osmotically active due to the electric field from the surface. As a result, an electrostatic double layer forms around the macroscopic particle. The effective electrostatic potential emanating from the surface is screened exponentially. The zeta potential at the slipping plane can be experimentally measured. For two similarly charged bodies, this electrostatic double layer force is repulsive.

We are left with two types of forces that govern the physical nature of the interactions between two microalgae: van der Waals and electrostatic. If we approximate our microalgae as uniform spheres with radius *R* of 4μm, the DLVO theory on the stability of charged colloids serves as an appropriate theoretical framework to describe our system.

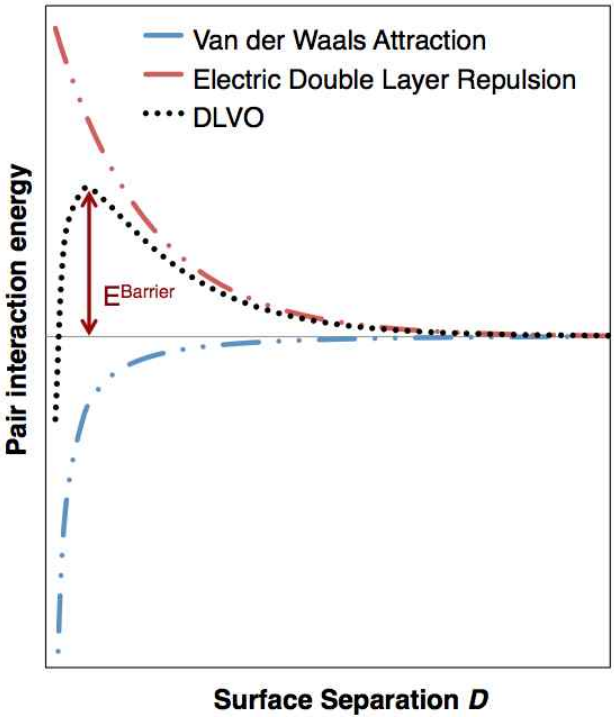


Figure 2.2. DLVO Interaction Potential Curve for two similarly charged species. The DLVO potential is an additive combination of van der Waals attraction and electrostatic repulsion.

## 2.2. DLVO Theory on the Stability of Colloids

Developed by Derjaguin and Landau [41], and Verwey and Overbeek [42], DLVO theory accounts for the combined effect of the attractive van der Waals and repulsive electrostatic double layer forces and treats them as additive (Figure 2.2). At longer ranges the electrostatic repulsions between similarly charged surfaces dominate over

attractive van der Waals forces. At shorter surface separations, a primary minimum begins to form when van der Waals forces substantially increase and colloids form irreversible aggregates. An overall energy barrier forms as a result. The scale of this barrier relative to the thermal energy available to a system $k_BT$ dictates the stability of colloids in solution. For $E^{Barrier} >> k_BT$ a stable suspension forms. Since algae do not spontaneously aggregate, we expect this energy barrier to be much larger than $k_BT$. This prevents statistically significant groupings of algae cells that are able to exist in the primary minimum region of the DLVO interaction curve. We will test this hypothesis.

The DLVO framework gives us the ability to calculate a pair interaction potential, predicts how tuning of this potential via experimental parameters influences the interaction, and provides quantitative results to strengthen our understanding of why algae form a stable mixture in water (i.e. do not flocculate). Deviations between the DLVO results and experimental observations do not fault DLVO, but rather underline the importance of non-DLVO forces [43]. The influence of these other forces has already been discussed and their contribution to the interaction has been ignored. The two proposed forms of the van der Waals and electrostatic energy are outlined below.

### 2.2.1. van der Waals (VDW) Potential

Starting from the attractive energy of interaction between two similar particles each containing $q$ atoms per $cm^3$:

$$F_{VDW} = -\int_{V_1} dv_1 \int_{V_2} dv_2 \frac{q^2\lambda}{r^6} \qquad (2.1)$$

Hamaker [44] derived the general equation for the nonretarded VDW potential between two spheres of equal radius $R$ at a separation $D$:

$$F_{VDW} = \frac{-A_H R}{6D}\left[\frac{2R}{4R+D} + \frac{2RD}{(2R+D)^2} + \frac{D}{R}\ln\frac{(4R+D)D}{(2R+D)^2}\right] \qquad (2.2)$$

In Eq. ( 2.1 ) $V_1$ and $V_2$ are the total volumes of the macroscopic bodies, $r$ is the distance between the two volume elements $dv$, and $\lambda$ is the London – van der Waals constant specific for the interaction. $A_H \equiv \pi^2\lambda q^2$ is the Hamaker constant that accounts

for the polarizabilities of all media involved. For metals and hydrocarbons in water typical values of $A_H$ are of order $10^{-21}$ and $10^{-19}$, respectively [45]. Figure 2.3 demonstrates that Eq. ( 2.2 ) shares the same asymptotic behavior of a more familiar form of the VDW energy for two similar spheres, $-A_H R/12D$, as $D/R \rightarrow 0$. These are the precise conditions that the latter expression holds true [43]. For values of $D \approx R$ the deviation between the two expressions increases and Eq. ( 2.2 ) predicts the correct relationship with surface separation.

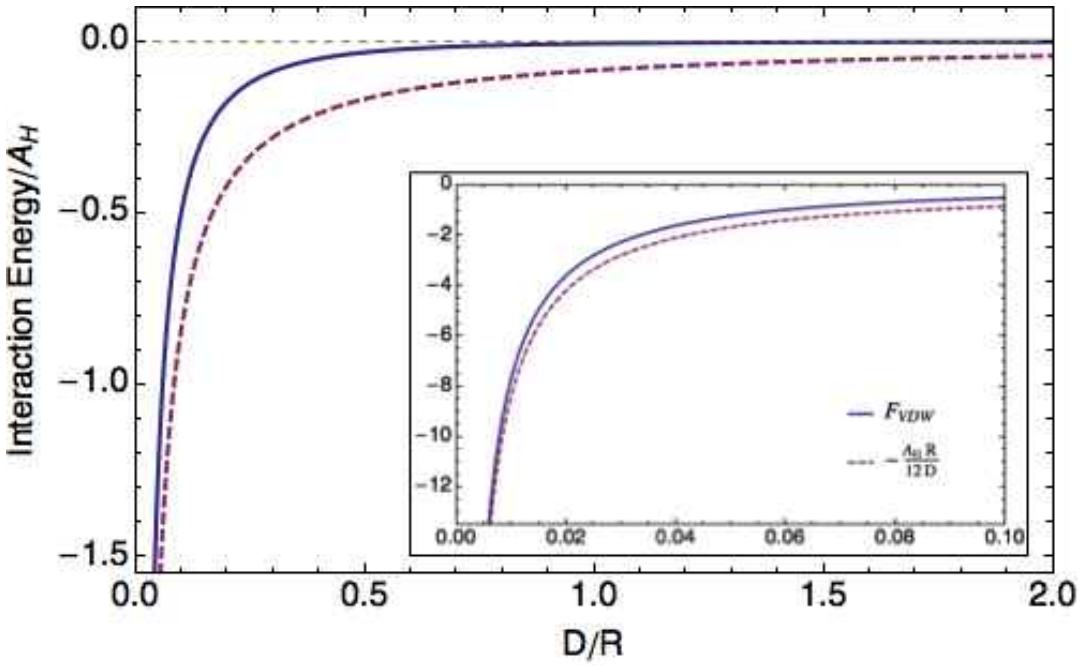


Figure 2.3. VDW Interaction Energy versus $D/R$. Inset: Enlarged area for $D/R \in [0, 0.1]$

It is important to note that in the determination of Eq. ( 2.2 ) from Eq. ( 2.1 ) the assumption of pairwise additivity between any two volume elements is made. The effect of neighboring atoms on the polarizability between these two volume elements is ignored. This is partially corrected through the use of the Lifshitz continuum theory in the determination of $A_H$. For macroscopic bodies composed of an anisotropic collection of atoms, Lifshitz and coworkers [46,47] proposed a solution to the many body interaction potential of the bodies in a medium based on macroscopic properties. Since VDW interactions are electrostatic in nature, the derivation of the potential starts from the fundamental principles provided by Maxwell's equations. The complexity of the deriva-

tion and the use of quantum field theory to arrive at the final result are beyond the scope of this discussion, but Isrealachvili [43] provides an estimate for the Hamaker constant using a modified form of the Lifshitz theory:

$$A_H = \frac{3}{2} k_B T \left(\frac{\varepsilon_1 - \varepsilon_2}{\varepsilon_1 + \varepsilon_2}\right)^2 + \frac{3h\nu_e}{16\sqrt{2}} \frac{(n_1^2 - n_2^2)^2}{(n_1^2 + n_2^2)^{3/2}} \quad (2.3)$$

where two identical phases 1 are interacting in a continuous medium 2, $\varepsilon$ is the dielectric permittivity, $h$ is Planck's constant, $n$ is the refractive index, $\nu_e$ is the main electronic absorption frequency in the UV. For water at room temperature, Israelachvili gives $\varepsilon_2$ = 80, $n_2$ = 1.333, and $\nu_e = 3.0 \times 10^{15}$ s$^{-1}$.

For microalgae cells, electric properties are harder to determine and are widely varied. We can estimate its dielectric permittivity $\varepsilon_r$ through its relation with the capacitance. Since the cell membrane acts as a barrier of charge, the outside surface can be thought of as a capacitor. The capacitance *C* of a membrane is a measurable quantity and is related to its dielectric permittivity constant:

$$C = \frac{\varepsilon_r \varepsilon_0}{d} \quad (2.4)$$

where $d$ is the thickness of the insulator between the two conducting plates (the cell membrane). *Chlamydomonas reinhardtii*'s cell wall is typically 40nm thick [48]. The capacitance of a eukaryotic cell membrane is approximately 1.0 $\mu$F/cm$^2$ [49,50]. The specific dielectric constant for microalgae is estimated below:

$$\varepsilon_r = \frac{Cd}{\varepsilon_0} = \frac{(1.0 \times 10^{-2}\ F/m^2)(4 \times 10^{-8}\ m)}{8.8542 \times 10^{-12}\ F\ m^{-1}} = 50 \quad (2.5)$$

The refractive index of biofuel producing *Chlamydomonas reinhardtii* was measured over the range of visible light with a range of values of 1.35-1.37 [51]. For measurements, we will use 1.36 for future calculations.

Using Eq. ( 2.3 ) $A_H$ was found to be $5 \times 10^{-22}$ *J* at 298 K. From Eq. ( 2.3 ) it is evident that lower value of $A_H$ result from similarities between the electric properties between the cell surface and water. Water is polarized by a phase of algae much in the

same way another phase of algae would be polarized. Thus water serves to dampen the dispersion forces of the van der Waal interactions between two algae.

### 2.2.2. Electrostatic Double Layer Potential

We are now interested in determining the electrostatic double layer (EDL) interaction potential between two algae cells. Recall Figure 2.1b, which illustrates the formation of the EDL around the negatively charged algae surfaces. The dissociation of functional groups along the surface results in a net negative charge. The electric field of this net negative charge pulls counter ions towards the surface in either a tightly bound Stern layer or a loose double layer. This EDL does not completely screen the charge repulsion as two similarly charged surfaces approach each other. The form of this interaction is exponential with respect to the surface separation: $F_{EDL}(D) \propto e^{-\kappa D}$ where $1/\kappa$, the Debye length, measures the range of the electrostatic effect of some charged body. Its form is only dependent on solution properties, i.e. the ionic strength and the permittivity of the solvent, $\varepsilon_s\varepsilon_0$:

$$\kappa^2 = \frac{1}{\varepsilon_s\varepsilon_0 k_B T}\sum_i \rho_{\infty i}(ev_i)^2 \text{ , in } m^{-2} \qquad (2.6)$$

where $\rho_{\infty i}$ is the concentration of ions *i* with valency $v_i$ in bulk where the reference electrostatic potential is defined as zero and $e$ is the elementary charge. It is suggested by Denton [52] that a correction to Eq. ( 2.6 ) be made to take into account the fact that the volume of the macroscopic polyions (algae) is unavailable to the ions in solution. However colloidal suspensions of algae are generally dilute and we can ignore this correction. Figure 2.4 shows the Debye length varying the bulk 1:1 monovalent salt concentration present in water. For concentrations more than $10^{-4}$ *M* the Debye length begins to drop off to zero. For a charged body in the presence of weak salt, the effective range of the electrostatic interaction rises exponentially. As a reference $1/\kappa$ for neutral water is marked.

When considering the interaction between two macroscopic polyions, it is typical to treat the medium as a continuous phase and ignore the size of the counter ions. Medina-Noyola and McQuarrie [53] continue this approximation while using a truncated

form of the linearized Poisson-Boltzmann equation for the first three terms of the series to solve for the interaction energy:

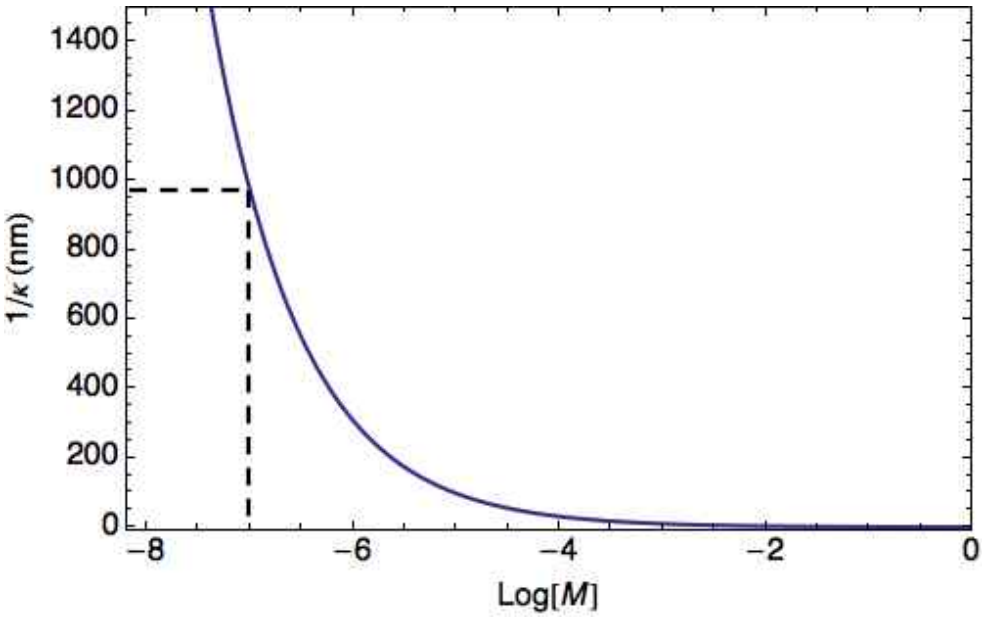


Figure 2.4. The Debye length for varying ionic strengths (*M* = moles/L) in water. Parameters: 298 K, 1:1 monovalent salt. Marked region represents Debye length = 971 nm for water at pH 7.

$$F_{EDL}(D) = \frac{Q^2}{4\pi\varepsilon_0\varepsilon_s(D+2R)}\frac{e^{-\kappa D}}{(1+\kappa R)^2}\,, \quad D \geq 0 \qquad (2.7)$$

where $Q$ is the uniform surface charge. To calculate $Q$ we require the value of the surface charge density $\sigma_C$. However, as briefly mentioned above, it is more convenient to measure electrostatic potential. The Grahame equation serves as an intermediary between the two quantities:

$$\sigma_C = \varepsilon_s\varepsilon_0\kappa\psi(0) \qquad (2.8)$$

where $\psi(0)$ is the electrostatic potential at the surface. Experimentally we can measure the zeta potential at the slipping plane of the EDL (see Figure 2.1b) using dynamic light scattering to calculate the electrophoretic mobility of a colloid in the presence of an applied field. $\psi(0)$ can be discovered from the zeta potential using *Gouy-Chapman* theory where (for small potentials, approx. ≤ 25 mV):

$$\psi_{zeta} = \psi(0)e^{-\kappa x} \quad (2.9)$$

where *x* is the thickness of the EDL.

Experimental measurements of the zeta potential for *Chlamydomonas reinhardtii* were made for algae in growth medium varying growth times and different pH (Figure 2.5). After approximately three days of growth time the average zeta potential begins to level out around -18 mV as the algae sizes and surface properties reach a steady state.

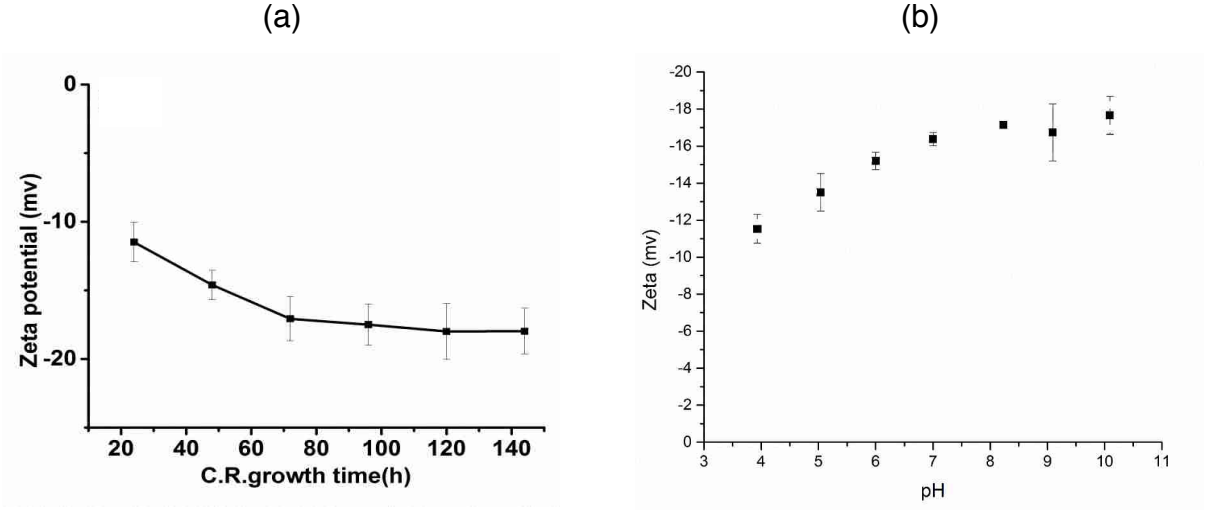


Figure 2.5. Zeta potential for experimental strain of algae in growth medium [23]. (a) Determination of the zeta potential varying the growth time (pH 8.3). (b) Zeta potential varying the pH of the solution after algae growth has reached a steady state.

When we increase the pH, acidic functional groups begin to completely dissociate along the surface and once again the zeta potential levels out around -18 mV.

To derive the surface potential from the zeta potential we now must calculate $\kappa$ in Eq. ( 2.9 ). We can make an assumption that avoids considering the complex behavior of the buffer solution and thickness of the EDL at first for different pH if we consider the ELD thickness $\approx 1/\kappa$. Recall that $1/\kappa$ represents the characteristic range of decay for some charge in an electrolyte solution. This range also determines the farthest distance from the surface where ions in solution feel the effects of the electric field. These ions make up the outer, electro-osmotically active diffuse layer. As an example, using Eq. ( 2.9 ) and Figure 2.5 we see that for pH 7 the surface potential $\psi(0) \approx$ -45 mV.

To determine the surface charge we can no longer use this assumption. From Eqs. ( 2.8 ) and ( 2.6 ) it is evident that we require an understanding of the composition

of the growth medium, which is typically a complicated mixture of buffer and other salts. Furthermore, the concentration can change as a result of nutrients (including ions) being absorbed by the algae cells. The most common growth medium for *Chlamydomonas* uses a tris-acetate buffer of 0.02 *M* (pH 7.2) in addition to 0.001 *M* (pH 7.0) potassium phosphate buffer, as well as a host of other trace salts [54,38]. The predominant contribution to the ionic strength comes from the dissociation of $NH_4Cl$, $K_2HPO_4$, and $KH_2PO_4$ with final medium concentrations (before nutrient uptake) of $7.0 \times 10^{-3}$ *M*, $1.6 \times 10^{-3}$ *M*, and $1.1 \times 10^{-3}$ *M*, respectively. Therefore, for neutral pH, the ionic strength is on the order of $10^{-2}$ *M*. We understand that after considering the contribution of all the salts and acid/base species using a numerical approach such as [55] that this ionic strength may be underestimated for the final solution. However we choose to round down since the final solution concentrations do not include nutrient uptake by the cells that would lower the overall salt concentration. Nonetheless, at room temperature this ionic strength translates to a Debye length on the order of $10^{-8}$ m. From Eq. ( 2.8 ) we find that our algae should have a surface charge density $\sigma_c$ on the order of $-10^{-3}$ C/m$^2$ under these conditions. When placed in a solution of mostly water with the same pH and temperature, the algae surface should maintain this charge.

## 2.3. Testing the Model by Varying the Ionic Strength

To test the validity of our model for calculating algae pair interaction potentials we hope to compare theoretical calculations with experimental observations of algae flocculation varying some experimental parameter. One approach would be to change the ionic strength of the algae medium. The experimental setup would begin by placing the algae cells in neutral water (ionic strength, *I*, of $10^{-7}$ *M*). The ionic strength of the solution can be increased by adding salt, mixing, and allowing the algae to settle. When the EDL repulsion is screened by the salt at some critical ionic strength such that the energy barrier $\sim k_BT$, the algae pairs can exist in the primary minimum DLVO range (see Figure 2.2) and form irreversible aggregates.

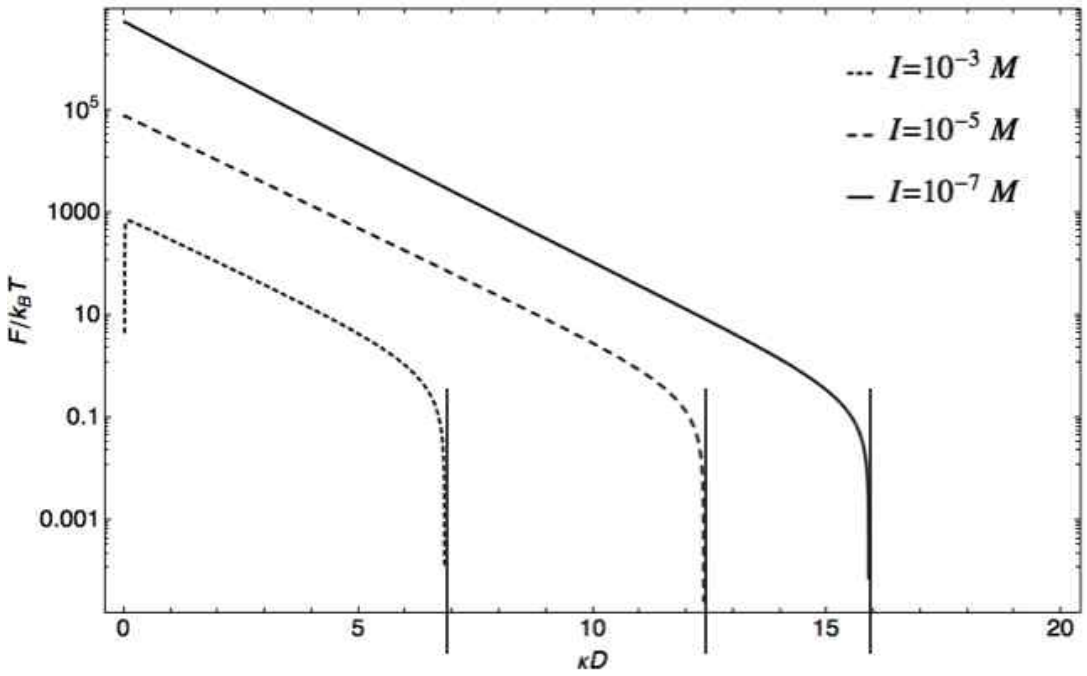


Figure 2.6. Logarithmically scaled DLVO free energy of interaction ($F$) for ionic strength $I$ = $10^{-3}$ moles/L ($M$), $10^{-5}$ $M$, $10^{-7}$ $M$ with $1/\kappa$ = 9.711 nm, 97.11 nm, and 971.1 nm, respectively. Vertical lines represent asymptotes log[x] →0. Parameters: $R$ = 4 $\mu$m, $A_H$ = $5\times10^{-22}$ J, $T$ = 298 K, water medium, $\sigma_c$ = $-10^{-3}$ C/m$^2$.

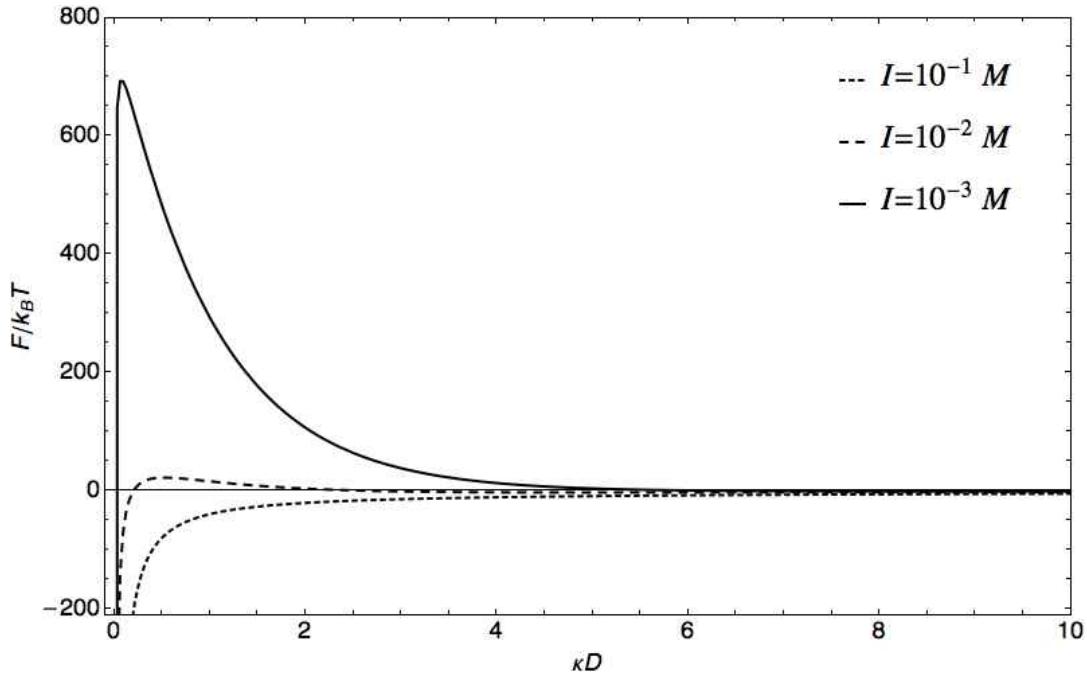


Figure 2.7. DLVO free energy of interaction ($F$) for ionic strength $I$ = $10^{-1}$ moles/L ($M$), $10^{-2}$ $M$, $10^{-3}$ $M$ with $1/\kappa$ = 0.971 nm, 3.07 nm, and 9.71 nm, respectively. Parameters same as in Figure 2.6.

This critical ionic strength can be visually observed and compared with theoretical calculations of the DLVO potential as in Figure 2.6 and Figure 2.7. In Figure 2.6 the normalized free energies are plotted logarithmically for comparison purposes. Vertical lines represent where the DLVO curves asymptotically approaches zero as $F/k_BT$ approaches one. Their intersection with the $x$-axis signifies where the free energy becomes negative. For clarity we decided not to plot absolute values. It is evident from Figure 2.6 that as we increase the ionic strength the EDL repulsion is screened by added salt. As $I \rightarrow 10^{-3}$ $M$ the ionic strength approaches a critical value where free energy of interaction is on the order of $k_BT$ at surface separations less than 100 nm. For neutral water, an algae cell feels the electrostatic repulsion from a neighboring algae cell up to 15 $\mu$m. Figure 2.7 shows the transition for the critical ionic strength. The energy barrier for $I = 10^{-2}$ $M$ is approximately 50 $k_BT$. This corresponds to physical observations of *Chlamydomonas* algae, where even in growth medium ($I = 10^{-2}$ $M$) the microalgae do not flocculate at room temperature. For $I = 10^{-1}$ $M$ the DLVO potential indicates that the pair interaction is completely attractive. In our proposed experimental setup this suggests that at this ionic strength we should begin to see aggregation between algae colloids.

## 2.4. Algae DLVO Interaction Energies in Neutral Water and Growth Medium

In order to harvest algae, cells must be separated from their growth medium and then dewatered and dried. Therefore, the two most important conditions for our investigation center on algae in their high salt growth medium and in neutral water where most of the growth medium salt has been removed or diluted. Furthermore, these two systems characterize the behavior of our algae at both extremes of the salt concentration spectrum for the experimental setup.

### 2.4.1. Neutral Water

For water with pH = 7 the medium is of low ionic strength and the characteristic range of decay $1/\kappa$ for the electrostatic repulsions between two algae cells is almost 1000 nm. As a result, neighboring algae cells electrostatically repel one another at far-

ther surface separations, *D*. To lower this expected DLVO energy barrier the VDW energy must be on the order of EDL repulsion. In contrast, Figure 2.8 shows that the EDL energy dominates at all relevant surface separations so that its value is coincident with the overall DLVO potential. In order to "overcome" this energy barrier and remain in a flocculated state, a pair of algae cells would need to be coupled to an energy source of approximately $5 \times 10^6$ $k_BT$, or $2 \times 10^{-14}$ J.

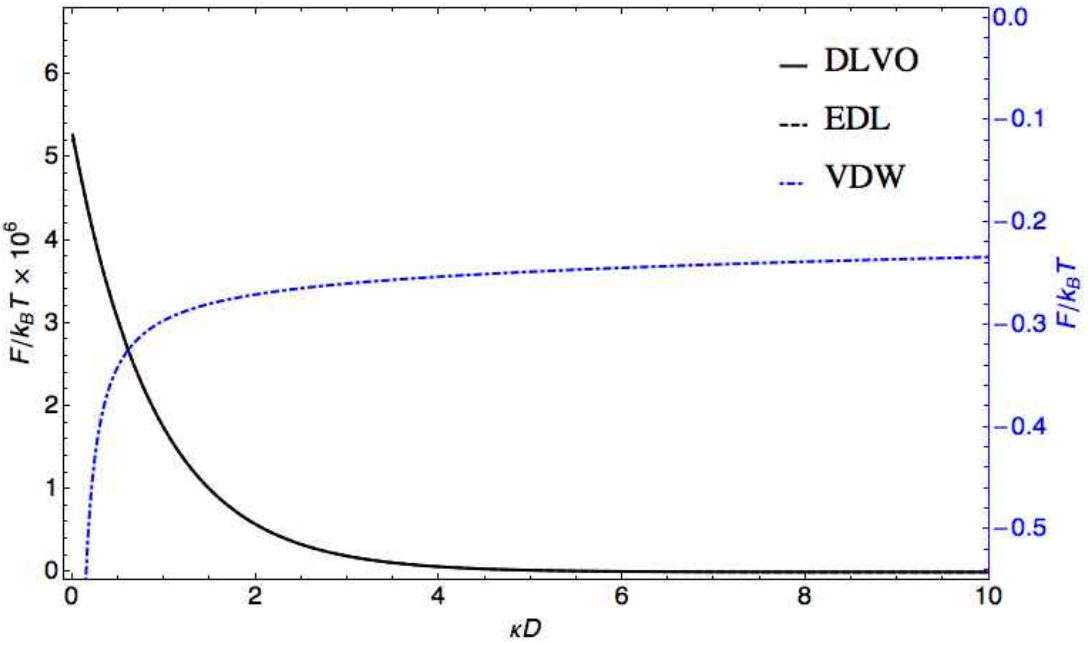


Figure 2.8. Free energy of interaction (*F*) for VDW, EDL, and DLVO potential in neutral water. All other parameters same as in Figure 2.6.

This repulsion is purely electrostatic. To understand the scale of this interaction, consider two negative point charges in water at room temperature interacting at some distance *d* on the order of hundreds of nanometers whose potential energy is given by $e^2/4\pi\varepsilon d \approx 0.007\, k_BT$. In comparison, the number of charges on the algae surface with $\sigma_c$ = -$10^{-3}$ C/m$^2$ is $|4\pi R^2\sigma_c/e| \approx 1.3 \times 10^6$ charges. If we replace the second negative point with half of an algae surface and consider the charge located all at one position some distance *d* on the order of hundreds of nanometers away, the new potential energy would increase by a factor of $0.6 \times 10^6$, or be approximately 5000 $k_BT$. In a similar way, for the interaction of two algae cells a single point charge on one surface is interacting with every point charge on the other surface. Though the approximation of each

of those charges being the same distance away does not hold up, one can now imagine how an interaction energy between two surfaces each carrying a scale of one million charges can have an interaction energy on the order of $10^6$ $k_BT$ in a medium of low ionic strength.

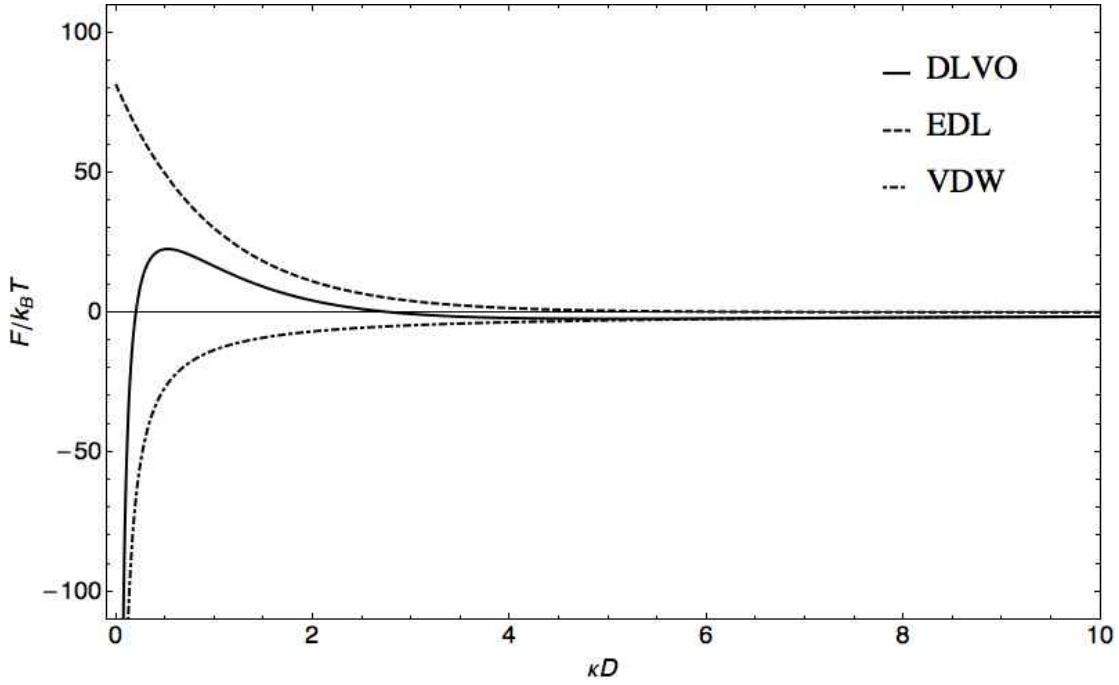


Figure 2.9. Free energy of interaction (*F*) for VDW, EDL, and DLVO potential in water with $I = 10^{-2}$ *M*. All other parameters same as in Figure 2.6.

2.4.2. Growth Medium

We estimated that the ionic strength of the experimental growth medium is on the order of $10^{-2}$ *M* ionic strength (see 2.2.2.). The Debye length is now on the order of several nanometers and the characteristic decay of the EDL repulsion is greatly reduced as compared to water with pH = 7. Figure 2.9 demonstrates this hypothesis. The VDW energy is now on the order of the EDL repulsion and a primary minimum occurs in the DLVO curve for $\kappa D < 1$ (corresponding to a surface separation ≈ 3 nm). This is a result of the high ionic strength of the medium being able to screen the effective charge on an algae surface, lowering the coulombic repulsion between like charged bodies. Also, a secondary minimum on the order of $k_BT$ is observed for $\kappa D \approx 5$ where the algae can form reversible aggregates. However, the energy barrier is still multiple times $k_BT$ and

the algae do not permanently flocculate in the growth medium solution, which is experimentally observed. Therefore, a method is needed that can allow algae to form stable aggregates so that they can be efficiently and cheaply dewatered and harvested for downstream processing.

## 2.5. Examining the Effective Charge Between Cells

Before we begin to investigate the experimental solution to the problem of harvesting by using charged polymer brushes, we can employ DLVO theory to gain some insight on how the charged polymer brushes may lead to spontaneous aggregation of the microorganisms. Much like in the case of adding salt, we hypothesize that the addition of the polymer brush screens the EDL repulsion. Introduction of the brush means adding cationic (charged monomers) and anionic (monomer counter ions) species to the system. The cationic units along the polymer backbone serve to screen the EDL repulsion between two algae by reducing the effective electric field between them.

### 2.5.1. Neutral Water

The anionic surface may attract the brush, possibly even causing the polymer to adsorb to its surface. This adsorption has been shown to cause the release of counter ions from the brush layers, which is entropically favorable [34]. If we hypothesize that the introduction of the brush screens the EDL repulsion by reducing the electric field each algae feels from another due to the effective charge, $\sigma_c$, we can use DLVO to qualitatively describe this phenomena. In Figure 2.10 we plot the logarithmic value of the unitless free energy of interaction between two algae cells in neutral water once again for comparison purposes. As before, for clarity purposes we chose not to represent the absolute value of the free energies that would have included negative values of the DLVO curve. Rather, we represent these areas of transition from positive to negative with vertical lines at the asymptotes as the value of the logarithm approaches zero. Figure 2.11 depicts the algae pair free energy of interaction for two cells in water with an ionic strength ($I$) of $10^{-2}$ $M$. We chose these two regions again to mimic the most common environments of the algae system (water and growth medium).

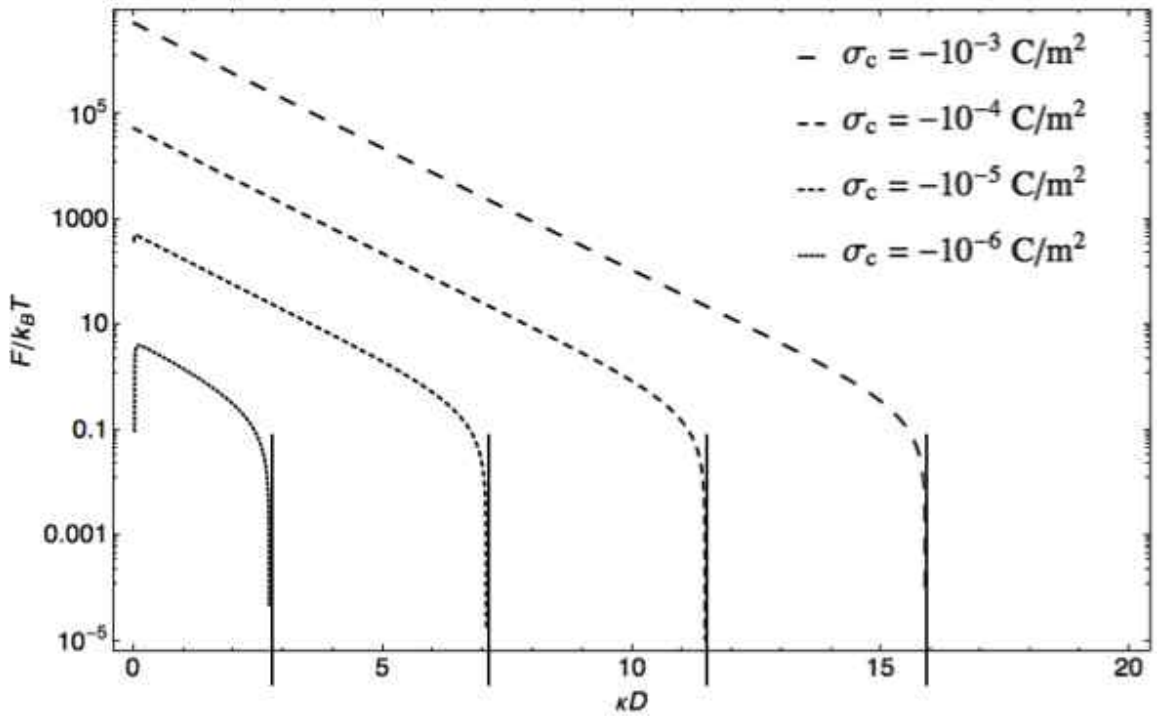


Figure 2.10. Logarithmically scaled DLVO free energy of interaction ($F$) for varying effective charge $\sigma_c$ in neutral water. Vertical lines represent asymptotes log[x] →0. All other parameters same as in Figure 2.6.

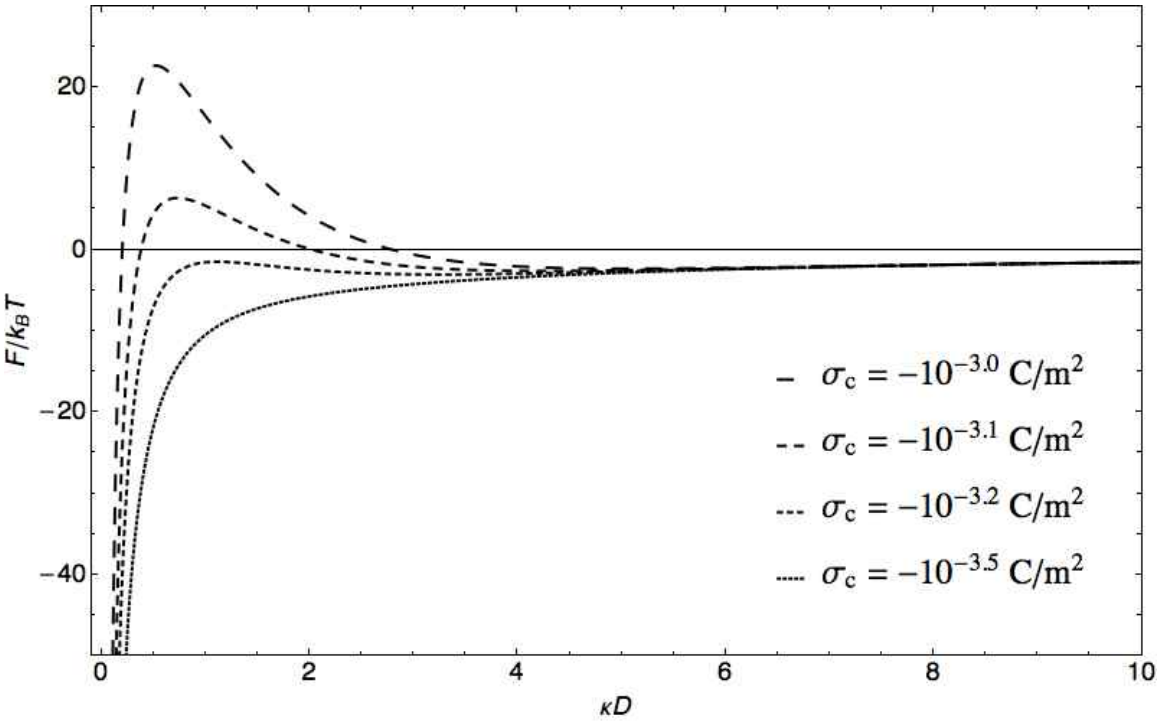


Figure 2.11. DLVO free energy of interaction ($F$) for varying effective charge $\sigma_c$ in water with $I = 10^{-2}$ $M$. All other parameters same as in Figure 2.6.

For the case of neutral water, we see that the DLVO energy barrier is much greater than $k_BT$ for most effective charge values. It is not until we reach $\sigma_c$ = -$10^{-6}$ C/m$^2$ when the energy barrier begins to become on the order of the thermal energy. Recall that for water pH = 7 the Debye length is approximately 1000 nm. Therefore the distance at this effective charge where the DLVO curve would signify an attractive force (when the EDL repulsion will begin to compare to the VDW energy) is around 3000 nm, equivalent to the radius of an algae sphere. If we once again picture the algae surface as a grouping of point charges we can see the equivalent number of charges that must be screened for $\sigma_c$ = -$10^{-6}$ C/m$^2$ by taking the difference with the initial state where $\sigma_c$ = $10^{-3}$ C/m$^2$. The percent of charges on the surface we must quench is given by ($10^{-3}$ – $10^{-6}$)/$10^{-3}$ = 99.9%. Therefore, even after we have screened almost all of the charges, we still observe an energetic barrier for the pair interaction between two cells. We must screen most of the remaining 0.1% of charges (≈ 1000) before algae pairs can begin to form in the primary minimum.

### 2.5.2. Growth Medium

In contrast we see that only small decreases in the effective charge lead to a state where the EDL repulsion is screened sufficiently enough so that the DLVO interaction is attractive at all surface separations (when $\sigma_c = -10^{-3.5}$). As a comparison with neutral water, this requires that only ($10^{-3.1}$ - $10^{-3.5}$)/$10^{-3.1}$ = 60% of the charges be screened by the cationic brush. The difference in values between neutral water and growth medium signify the ability of the high ionic strength salt to already screen most of the effective charge between two algae cells.

## 2.6. Conclusions

The DLVO theoretical framework predicts that the pair interaction between two algae species is repulsive for the two most common environments of our system: growth medium and neutral water. In both cases, the EDL energy dominates the VDW energy at almost all surface separations greater than 10 nm. Physically this means that algae

do not spontaneously flocculate due to the similar charge coulombic repulsion between the surfaces.

In the case of low ionic strength solutions, such as neutral water, this energy barrier that prevents flocculation is more pronounced and much higher than the thermal energy available to the cells. Even when over 99% of the charges are quenched, the energy barrier is still several orders of magnitude higher than $k_B T$.

For high ionic strength solutions the EDL repulsion is screened by the added salts and the energy barrier begins to be on the order of magnitude of the thermal energy and the VDW energy for distances below 100 nm. In some cases, this results in the formation of a secondary minimum where an energy barrier still exists but a minimum in the DLVO curve at surface separations before the primary minimum physically allows for reversible flocculation. At higher ionic strength, about half the charges need to be quenched before the effective charge is low enough so that the pair interaction is attractive at all separations.

For the experimental solution to the low-cost efficient method for algae dewatering and harvesting, we hypothesize that the cationic polymer brushes serve to screen the EDL repulsive force between algae cells. When the brushes do not adsorb, they serve to increase the ionic strength much like in the case of adding salt. If adsorption occurs, the brush quenches negative charges on the surface of the algae, reducing the effective charge and lowering the energy barrier. More brushes are needed for low ionic strength solutions than higher ones. This transition between high and low ionic strength solutions occurs when the energy barrier is on the order of the thermal energy at a critical value around $10^{-2}$ and $10^{-3}$ *M*.

# CHAPTER 3
# CHARGED POLYMER BRUSH AND ALGAE INTERACTIONS

The flocculation agent involves a polymer brush grafted to a nanoparticle core. If we are to understand the interactions in our system we require a method for modeling the polymer brush behavior in different environments. In this chapter, we explain the theoretical framework used to perform this piece of the project and provide explicit calculations.

## 3.1. Introduction to Modeling Polymer Brush Systems

We now must calculate the energy between the remaining pair interactions in our system: algae – polymer brush and brush – brush. Since both require consideration of the dynamic behavior of the polymer in response to changing stimuli, we use Self-Consistent Field Theory (SCFT) for polymers to model the system. Unlike DLVO, SCFT provides much greater structural information about brush density distributions and allows models to consider multi-component effects inside the brush in much greater detail. Initially formulated by Edwards and Dolan [56], SCFT attempts to find a simplified description of interacting chains through a mean field approach. Rather than taking into account all interactions between bodies in the system, it only considers the conformational fluctuations of any given polymer chain in the averaged environment (mean field) due to the presence of all other species (see Figure 3.1). A self-consistent calculation is then established between the local monomer concentration profile and the position dependent mean field potential around the concentration profile. Upon convergence, thermodynamic properties of the system can be computed. Here we will outline the extension of the Scheutjens and Fleer lattice SCFT for a multicomponent mixture [57,59] and extend it for a charged system.

3.2. A Lattice Model for Polymer Systems

Consider discretizing a space into a three dimensional lattice. We can fill this lattice with a multicomponent mixture of molecules. Let $r_{Ai}$ be the number of segments of type *A* belonging to a particular molecule of type *i*. If $r_i$ is the total number of segments belonging to a molecule of type *i*, $\sum_A r_{Ai} = r_i$. We can arbitrarily pick a space coordinate to label our three dimensional lattice. Consider the cross sectional slices defined by the direction *x* and *y* with number of sites *L*. Starting from one of the boundaries of our system, we can label these slices along the *z* axis as 1, 2, … *M*. If we adopt a mean-field approximation in the steps of Scheutjens and Fleer [57] we can consider the segments of a given molecule to be randomly distributed over the *L* lattice sites in layer *z*. Therefore we most only consider the density fluctuations along *z*. The number of segments of type *A* belonging to molecule *i* in a given slice (or layer) is given as $r_{Ai}(z)$.

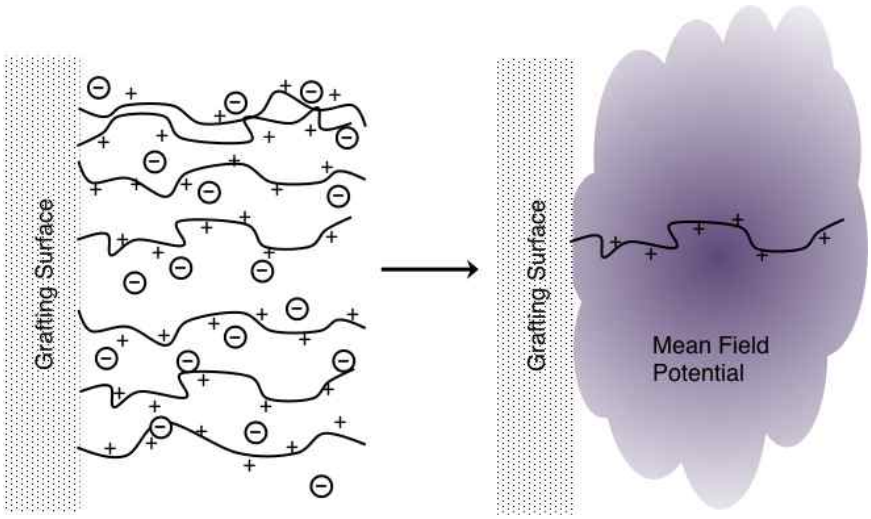


Figure 3.1. SCFT simplifies a many body problem using a position dependent mean field potential. System involves a polymer brush with cationic monomers along the backbone and anionic counter ions.

It now makes sense to define a particular conformation of a molecule by the layer labels of each of its segments. For instance the chain molecule in Figure 3.2 has a conformation given by (*a*,2), (*b*,2), (*c*,3), (*d*,4). The conformation of every molecule in the multicomponent mixture is completely defined by the *z* coordinates of its segments. We can now introduce another identifier to our notation for our molecules in the system con-

sidering a specific conformation of the molecules. Let $r_{Ai}^{c}$ be the number of segments of type *A* belonging to a molecule of type *i* in a specific conformation *c*. The total number of segments for a given conformation is the same as before: $\sum_A r_{Ai}^{c} = r_i^{c} = r_i$. The number of molecules of type *i* with the same conformation is denoted by $n_i^{c}$. The total number of molecules of type *i* in the system is given as a sum over all the different conformations: $n_i = \sum_c n_i^{c}$. If we constrain our lattice to be incompressible (completely filled), the total number of segments $\sum_i n_i r_i$ must equal the total number of lattice sites *ML*.

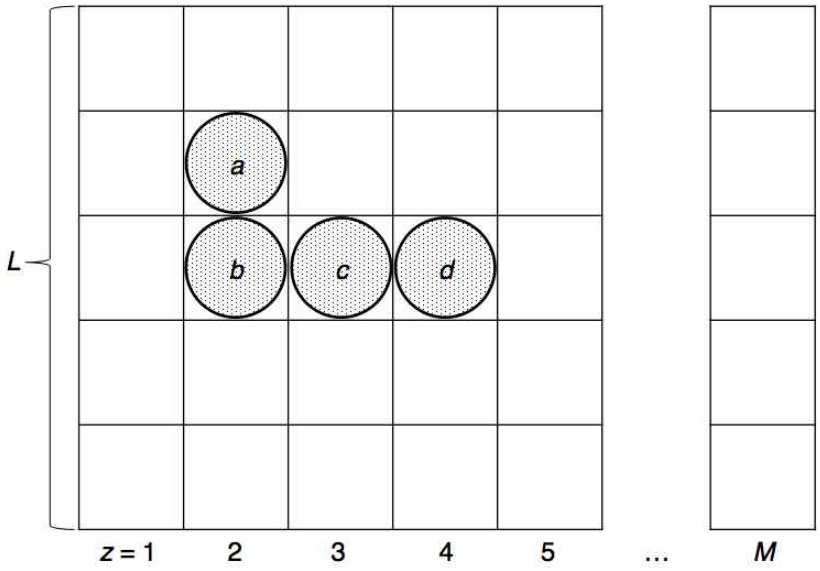


Figure 3.2. A particular conformation of a molecule on a lattice. Here space is shown only in two dimensions with fluctuations along the layers *z* characterizing the system. For this two dimensional system, *L* = 5.

3.3. Determining the Partition Function

Imagine our multicomponent mixture is in thermal equilibrium with both a particle and temperature reservoir. The grand canonical partition function for such a system is given by:

$$\Xi = \sum_{j}^{all\ states} e^{-\beta(E_j - \mu N_j)} \qquad (3.1)$$

The possible states of the system are simply all the possible concentration profile variations along *z* for all the molecules. The definition of a state follows from the idea that a given concentration gradient is defined by the set of conformations for all the molecules

in the system, $\{n_i^c\}$. Any given $\{n_i^c\}$ completely fills all the lattice sites. It is customary to decompose the grand partition function using the canonical partition function:

$$\Xi(\{\mu_i\}, M, L, T) = \sum_{\{n_i^c\}} e^{-\beta E_{\{n_i^c\}}} e^{\sum_i \beta \mu_i n_i} = \sum_{\{n_i^c\}} Q(\{n_i^c\}, M, L, T)\, e^{\sum_i \beta \mu_i n_i} \quad (3.2)$$

where it is important to remember we are summing over all possible fluctuations of the molecular densities in the layers. Note that the variables are the set of chemical potentials of the molecules, the volume, and the temperature. If the system is internally constrained such that one of these variables is varied while the others are held constant, the value of this parameter at equilibrium maximizes the entropy and minimizes the grand free energy.

Each individual *Q* in Eq. ( 3.2 ) is defined by the same number and type of molecules in each layer. Under the mean field approximation each possible realization of $\{n_i^c\}$ has the same total energy *U* since the same number and type of interactions remains constant. *Q* becomes $\Omega e^{-\beta U}$ where $\Omega$ is the degeneracy (multiplicity) of $\{n_i^c\}$. Since it is differences in energies that are important, it is useful to express *Q* in terms of a reference state. Let $Q_i^* = \Omega_i^* e^{-\beta U_i^*}$ be the partition function for $n_i$ molecules in homogenous bulk phase. The total energy $U^* = \sum_i U_i^*$ and the partition function decomposes into a product: $Q^* = \prod_i Q_i$. The canonical partition function becomes

$$Q = Q^* \frac{\Omega}{\Omega^*} e^{-\beta(U - U^*)} \quad (3.3)$$

where $\Omega^*$ is the product of individual multiplicities $\Omega_i^*$ and counts all the possible ways of distributing $n_i$ molecules in the bulk phase with a given conformation *c*.

To determine $\Omega_i^*$, let us consider a lattice construction of bulk phase. Unlike for our system, each of the layers is identical and defining a conformation by a layer number is meaningless. The total number of sites occupied by a species of type *i* is given by the product of the total number of molecules of type *i* $(n_i)$ and the number of segments belonging to the molecule $(r_i)$. It is clear then that for the placement of the first segment

on a molecule of type *i* there are $n_i r_i$ possibilities. If each lattice site has *Z* neighbors, the placement of the second segment is limited to *Z* options since it is attached to the first. However, we must take into account the probability that any of the neighboring sites are already filled. Under the mean-field approximation of random mixing in each layer all sites in a given layer have the same likelihood of being vacant, given by 1 – *p*(filled) where *p*(filled) for indistinguishable layers in bulk is the probability that any of the possible sites available to a segment belonging to a molecule of type *i* is already filled. For the second segment, the number of possible configurations is now limited to *Z*(1 – *p*(filled)) $= Z(1 - 1 \,/\, (n_i\, r_i)) = Z(n_i\, r_i - 1) \,/\, (n_i\, r_i\,)$. For the *jth* segment this expression can be generalized to $Z(n_i\, r_i - j) \,/\, (n_i\, r_i)$. Therefore the overall configuration multiplicity for the first molecule of species *i* is given as:

$$\Omega_1^* = \left(\frac{Z}{n_i r_i}\right)^{r_i - 1} (n_i r_i)(n_i r_i - 1)(n_i r_i - 2) \ldots (n_i r_i - r_i) \qquad (3.4)$$

The configurational multiplicity of the *kth* molecule of species *i* can be determined using the same logical methology. The placement of the first segment has $n_i r_i - (k-1) r_i$ possibilities. The number of ways of placing each successive segment is still *Z*(1 – *p*(filled)). The form of the overall configuration multiplicity is identical to Eq. ( 3.4 ) with the exeception of the shift taking into account the previous placement of *k* – 1 molecules:

$$\Omega_k^* = \left(\frac{Z}{n_i r_i}\right)^{r_i - 1} (n_i r_i - (k-1) r_i)(n_i r_i - (k-1) r_i - 1) \ldots (n_i r_i - (k-1) r_i - r_i) \qquad (3.5)$$

The overall multiplicity is simply a product of each of the individual molecule expressions, e.g. Eqs. ( 3.4 ) and ( 3.5 ). After positioning all $n_i$ molecules, an expression for $\Omega_i^*$ identical to the combinatory factor derived by Flory [58] follows:

$$\Omega_i^* = \frac{(n_i r_i)!}{n_i!} \left(\frac{Z}{n_i r_i}\right)^{(r_i - 1) n_i} \qquad (3.6)$$

where $1/n_i!$ accounts for the indistinguishability of molecules *i*.

Determining $\Omega$ is a little more complicated due to the distinguishability of layers in the system. Recall that *L* is the number of lattice sites per layer, *Z* is the number of neighbors per lattice site and the set $\{n_i^c\}$ is completely defined by the specific layer

number sequence belonging to all types of molecules *i* present in the system. Consider the conformation of a given molecule *i* where $n_i^c$ is the number of molecules *i* with the same configuration. The first segment of the molecule can be distributed at any of the *L* sites in its layer if each site is empty. As before, we can take into account the possibility that part of the layer is already filled by considering the fraction of empty sites within the layer equal to $1 - v_z/L = (L - v_z)/L$ where $v_z$ is the occupation number of the layer *z* (for the first segment $v_z = 0$).

Before we discuss the possible configurations for the additional segment we must briefly introduce some notation. Consider the conformation of the molecule in Figure 3.2 (*a*,2), (*b*,2), (*c*,3), (*d*,4) [figure on lattice polymer]. If *k* is the label attributed to layer "2", the second segment is in layer *k*, the third in layer $k + 1$, and the fourth in $k + 2$. The first segment *a* has *Z* neighbors, $2\lambda_1 Z$ in the two adjacent layers and $\lambda_0 Z$ in the same layer. Segment *b* is in the same layer as segment *a*. Therefore there are $\lambda_0 Z$ possible sites for segment *b*. Segment *c* is in an adjacent layer to segment *b* and has $\lambda_1 Z$ possible configurations. The same can be said for segment *d*. For the entire molecule in its current conformation there are $(L - v_2)(Z/L)^3[\lambda_0(L - v_2 - 1)][\lambda_1(L - v_3)][\lambda_1(L - v_4)]$ ways of placing it on the lattice. Following the work of Evers et al. [59] it proves convenient to define the following variable:

$$\lambda^c = \prod_{s=2}^{r_i} \lambda^c(s|s-1) \qquad (3.7)$$

where $\lambda^c(s|s-1)$ is equal to $\lambda_0$ if the *sth* segment is in the same layer as the *s*-1*th* or $\lambda_1$ if they are in adjacent layers. The superscript denotes the particular conformation.

The number of different ways of placing a molecule *i* in a unique conformation *c* can now be expressed as:

$$\Omega_1^c = \left(\frac{Z}{L}\right)^{r_i - 1} \lambda^c \prod_{s=1}^{r_i} \left(L - v_{z(s,c)}\right) \qquad (3.8)$$

The product in Eq. ( 3.8 ) can be simplified by replacing it with a product over the lattice layers. Consider that the molecule *i* in configuration *c* contributes $r_i^c(z)$ molecules to the lattice layer *z*. For the first segment being placed in an empty lattice in layer *z*, $r_i^c(z) = 1$

and $v_z = 0$. For the second segment $r_i^c(z) = 2$ and $v_z = 1$, … ending with $v_z = r_i^c(z) - 1$. The product can now be expressed as $\prod_{z=1}^{M} \prod_{v_z=0}^{r_i^c(z)-1} (L - v_z)$. Instead of keeping track of the placement of every previous segment when evaluating the product in Eq. ( 3.8 ), we only have to know $r_i^c(z)$. For $n_i^c$ molecules, the first two terms in $\Omega_1^c$ are multiplied $n_i^c$ times while the product over $v_z$ now extends to $n_i^c r_i^c(z) - 1$ (if $n_i^c = 3$, on the third chain with the same configuration we have already placed $2r_i^c$ segments in that layer). For $n_i = \sum_c n_i^c$ molecules, we can express $\Omega_i$:

$$\Omega_i = \left(\frac{Z}{L}\right)^{(r_i-1)n_i} \prod_c \lambda^{c\,n_c} \prod_{z=1}^{M} \prod_{v_z=0}^{n_i r_i(z)-1} (L - v_z) \Big/ n_i^c! \qquad (3.9)$$

where $r_i(z) = \sum_c r_i^c(z)$ and the factorial accounts for indistinguishability of the molecules in the same confirmation. The first term in $\Omega_1^c$ is independent of configuration and is now repeated $n_i$ times in Eq. ( 3.9 ). However, $\lambda^c$ is unique for each configuration and requires us to take the product.

If we completely fill all *ML* lattice sites with the remaining species of molecules, the incompressibility requirement requires that the product $\prod_{v_z=0}^{n_i r_i(z)-1} (L - v_z) = L!$ since every site in the layer *z* is completely filled. The rest of the terms in $\Omega_i$ are identical for every *i* and simply become a product overall all species. We arrive at an expression for $\Omega$ similar to $\Omega^*$:

$$\Omega = (L!)^M \prod_i \left(\frac{Z}{L}\right)^{(r_i-1)n_i} \prod_c \lambda^{c\,n_c} \Big/ n_i^c! \qquad (3.10)$$

The only difference in our derivation of Eq. ( 3.10 ) and $\Omega^* = \prod_i \Omega_i^*$ for $\Omega_i^*$ in Eq. ( 3.6 ) is the distinguishability of the layers. The logartithm of both terms is closely related to the entropy through Boltzmann's famous equation for the entropy in the microcanonical ensemble $S \propto \ln \Omega$. Taking the logarithm of both terms also allow us to qualitatively determine the difference in entropy that occurs when we take the molecules from bulk and position them in our system. When determining the difference between the two logarithms many terms cancel:

$$\ln \frac{\Omega}{\Omega^*} = \sum_{i,c} n_i^c \ln \frac{L\lambda^c}{r_i n_i^c} \qquad (3.11)$$

where we have made use of Stirling's Appromixation for $\ln n! = n \ln n - n$ and the incompressibility of our system where $\sum_i r_i n_i = ML$. Recall $\lambda^c$ in Eq. ( 3.7 ) is a consequence of labeling the layers in the system as opposed to the indistinguishability of layers in bulk. With *L* being the cross sectional area of the lattice and $r_i n_i^c$ representing the space available to a particular conformation of molecule *i,* we can consider $L/r_i n_i^c$ a constant (if we double our system size, the lateral density fluctuations with respect to *z* should remain constant and $n_i^c$ is also doubled). Therefore $\ln \Omega/\Omega^* \propto \sum_{i,c} n_i^c \ln \lambda^c$. It is clear now that the difference in the entropy between bulk phase and the system is directly a consequence of numbering the layers in the system. As an example let us consider two extremes. First, if we have only one molecule in our system and its segments are all in the same layer then $\lambda^a = r_i \lambda_0$ and $\ln \Omega/\Omega^* \propto -\ln 1/r_i\lambda_0 = -\ln 1.5/r_i$ for a cubic lattice. Now if we change the conformation of the molecule so that each segment is placed in a different layer from its previous segment instead then $\lambda^b = r_i \lambda_1$ and $\ln \Omega/\Omega^* \propto -\ln 1/r_i\lambda_1 = -\ln 6/r_i$. It is clear that in the latter case increasing the randomness of the molecule's configuration increases the entropy difference between the bulk phase and the system. If each layer was given the same label (indistinguishable), the latter case would be identical to the former where all the segments were in the same layer and the difference between the two would vanish (signifying no difference between $\Omega$ and $\Omega^*$).

Eq. ( 3.11 ) naturally leads to the expression of the canonical partition function in its logarithmic form:

$$\ln Q = \sum_{i,c} n_i^c \ln \frac{L\lambda^c}{r_i n_i^c} - \frac{U - U^*}{k_B T} + \ln Q^* \qquad (3.12)$$

### 3.4. Equilibrium Statistics

Now that we have some construct for the canonical partition function in Eq. ( 3.2 ) we must determine the equilibrium form of the grand canonical partition function in order

to calculate important thermodynamic properties of the system. At equilibrium $\Xi$ minimizes the grand free energy $\Phi$ through the statistical thermodynamics relationship $\Phi = -k_B T \ln \Xi$. Therefore there is an equilibrium set of $\{n_i^c\}$ that maximizes $\ln \Xi$ subject to the constraint that each layer is completely filled. The Langrange method of undetermined multipliers is a useful tool to determine $\{n_i^c\}$ subject to any constraint. First we define the following function:

$$\mathcal{L} = \ln Q + \sum_i \frac{\mu_i n_i}{k_B T} - \sum_z^M \epsilon(z) \left[ L - \sum_{i,c} n_i^c r_i^c(z) \right] \qquad (3.13)$$

When the lattice is completely filled, $\mathcal{L}$ and $\ln \Xi$ are maximized by the same equilibrium set of $\{n_i^c\}$.

Taking the partial derivative of $\mathcal{L}$ with respect to $\{n_i^c\}$ in order to find the extremum involves solving the set of equations below:

$$\left( \frac{\partial \mathcal{L}}{\partial n_j^d} \right)_{M,L,T,n_i^c \neq n_j^d} = 0$$

$$= \frac{\partial \ln Q}{\partial n_j^d} + \frac{\mu_j}{k_B T} + \sum_z^M \epsilon(z) r_j^d(z) \quad \text{for all } n_j^d \in \{n_i^c\} \qquad (3.14)$$

and

$$\frac{\partial \mathcal{L}}{\partial \epsilon(z)} = 0, \qquad z = 1, 2, \ldots M$$

The first term can be solved for using Eq. ( 3.10 ):

$$\frac{\partial \ln Q}{\partial n_j^d} = \ln \frac{L \lambda^d}{r_i n_i^d} - 1 - \frac{\partial \left( U - U^* \right)/k_B T}{\partial n_j^d} - \frac{\mu_j^*}{k_B T} \qquad (3.15)$$

where we have made use of the total differential of the free energy $dF = d(-k_B T \ln Q)$ for constant temperature and volume to derive $\mu_j^*$, the chemical potential of species *j* in bulk phase. It proves convenient to introduce a factor of $r_j^d$ in the third term of Eq. ( 3.15 ). We can use the definition of the volume fraction of a particular segment of species *i*, $\phi_A(z) = n_i^c r_{Ai}^c(z)/L$, to do so:

$$\frac{\partial \left( U - U^* \right)/k_B T}{\partial n_j^d} = \frac{\partial \left( U - U^* \right)/k_B T}{\partial n_j^d} \frac{\partial \sum_{A,z} L \phi_A(z)}{\partial \sum_{A,z} L \phi_A(z)}$$

$$= \sum_{A,z} \frac{\partial\,(U - U^*)/Lk_BT}{\partial \phi_A(z)} \frac{\partial L\phi_A(z)}{\partial n_j^d} \qquad (3.16)$$

This particular notation also proves useful since it allows us to decompose $U$ into contributions of segments in order to evaluate the derivative with respect to the volume fraction, as we will show later.

By substituting Eqs. ( 3.15 ) and ( 3.16 ) into ( 3.14 ) and rearranging we obtain:

$$\ln \frac{L\lambda^d}{r_i n_i^d} - 1 + \frac{\mu_j - \mu_j^*}{k_BT} - \sum_{z,A}^{M} r_{Aj}^d(z) \left[ \frac{\partial\,(U - U^*)/Lk_BT}{\partial \phi_A(z)} - \epsilon(z) \right] = 0$$

$$\text{for all } n_j^d \in \{n_i^c\} \qquad (3.17)$$

$$L - \sum_{i,c} n_i^c r_i^c(z) = 0, \quad z = 1, 2, \ldots M$$

Eq. ( 3.17 ) gives an expression for every $n_j^d \in \{n_i^c\}$ through the first term. If the bulk reference state is large enough to fix the chemical potential inside the system, the third term vanishes. Knowing the equilibrium distribution of the system allows us to derive all thermodynamic properties of interest.

## 3.5. Determining Volume Fractions

An explicit picture of the system is a useful piece of information that Eq. ( 3.17 ) allows us to uncover. We can precisely diagram the system by determining the volume fractions of each species present in each layer. However we must find a link between the segment volume fractions and the overall equilibrium configuration. This is provided by determining the probabilistic weight some segment has at being at a lattice site in layer z. These weights are usually related to the energetic potential of the segment being present at that location. We begin by finding a form of the potential.

The derivative in square brackets in Eq. ( 3.17 ) quantifies the change in the total energy per layer that occurs when we change the volume fraction of a given segment with respect to a reference state in bulk. We can interpret this as the energy difference when we take some volume fraction of *A* and place it at some lattice point within the layer *z,* divided by the thermal energy. We can define this segment potential:

$$u_A(z) = \frac{\partial\,(U - U^*)/L}{\partial \phi_A(z)} - k_B T \epsilon(z) \qquad (3.18)$$

The last term is the potential required to prevent layer *z* from being under or overfilled.

To determine a connection between the segment potential and the segment volume fraction, recall the definition $\phi_A(z) = n_i^c r_{Ai}^c(z)/L$. In Eq. ( 3.17 ) we can isolate $n_i^c/L$. After substituting in Eq. ( 3.18 ) we obtain:

$$\frac{n_i^c}{L} = C_i \lambda^c \prod_{z,A} G_A(z)^{r_{Ai}^c(z)} \qquad (3.19)$$

where the constant in front does not depend on segment type or configuration:

$$\ln C_i = \frac{\mu_i - \mu_i^*}{k_B T} - 1 - \ln r_i \qquad (3.20)$$

and $G_A(z) = e^{-u_A/k_B T}$ is a Boltzmann weighting factor for segment *A* to be in layer *z* as opposed to bulk. Multiplying both sides of Eq. ( 3.19 ) by $r_{Ai}^c(z)$ recovers the volume fraction of segment *A* in layer *z* belonging to a particular configuration of molecule *i*. If we sum over all possible conformations we obtain the volume fraction of all segment *A*'s belonging to molecules *i*. After summing over *A* we obtain the volume fraction for all species *i*:

$$\phi_i(z) = \sum_c \frac{n_i^c r_i^c(z)}{L} = C_i \sum_c \lambda^c G_i^c r_i^c(z) \qquad (3.21)$$

where $G_i^c$ is the abbreviation for the product in Eq. ( 3.19 ). The significance of $\lambda^c G_i^c$ and $C_i$ are perhaps more clear now from Eq. ( 3.21 ). If a molecule has $r_i^c(z)$ segments in a particular layer, $\lambda^c G_i^c$ represents the statistical weight associated to these segments in that layer based on the freely jointed walk of that molecule on the lattice and the local segment potential those segments feel at that site. Collectively these resemble a "walk" weighting factor. $C_i$ serves to normalize the distribution to volume fractions.

However we have no knowledge of $n_i^c$ or $r_i^c$ beforehand so we still require a method for determining the volume fractions. Both the continuum theory [56] and the discrete formulation [57] draw a parallel between the conformation of the chained molecules in

the system and the semi-random walk of the molecules under the influence of some potential. In the latter case, determining the equilibrium configuration of the system is similar to filling the lattice with individual molecules by placing the first segment at any position and allowing the rest of the segments to walk across the lattice sites subject to bond restrictions and the local mean field potential. Of important note, Iakovlev [60] has shown that the resulting diffusion equation used to solve for the weighting functions in the continuum case decomposes into a propagator equation/recurrence relations on a lattice, which we derive here.

In the footsteps of Evers and coworkers [59] we define a "chain end distribution function" $G_i(z,s|1)$ which gives the combined weight of all possible walks starting with segment *s=1* and ending at *s* in layer *z*. Consequentially $G_i(z,r_i|1)$ is the statistical weight of all complete walks of a molecule ending at layer *z*. Summation over all layers gives the complete distribution function of the molecule over the entire system. This term is equivalent to $\sum_c \lambda^c G_i^c$, as Evers and co. note:

$$G_i(r_i|1) \equiv \sum_z G_i(z,r_i|1) = \sum_c \lambda^c G_i^c = \frac{n_i}{C_i L} \qquad (3.22)$$

Therefore, $G_i(z,r_i|1)$ is simply equal to $\lambda^c G_i^c$ when the conformation *c* results in the last segment $r_i$ being placed in layer *z*.

From this equality it is possible to derive a recurrence relation for each of the chain end distribution functions. Let us define $G_i(z,s)$ as the segment weighting factor equivalent to $G_A(z)$ when *s* belonging to molecule *i* is of type *A*. When we express $G_i(z,r_i|1)$ in terms of $G_i(z,r_i-1|1)$, we realize that a factor of $G_i(z,r_i)$ is pulled out in front and $r_{Ai}^c(z)$ diminishes by one when $z' = z$. A single bond weighting factor also arises (ref. Eq. ( 3.7 )).

$$G_i(z,r_i|1) = \sum_{c(r_i \text{ at } z)} \lambda^c \prod_{z',A} G_A(z')^{r_{Ai}^c(z')}$$

$$= G_i(z,r_i) \sum_{c(r_i \text{ at } z)} \lambda^c(r_i|r_i-1)\lambda_{1,r_i-1}^c \prod_{z',A} G_A(z')^{r_{Ai}^c(z')} \qquad (3.23)$$

$$= G_i(z, r_i) \sum_{c(r_i \text{ at } z)} \lambda^c(r_i | r_i - 1) G_i(z, r_i - 1 | 1)$$

Considering in Eq. ( 3.23 ) the sum is only over the conformations where $s = r_i$ is in *z*, segment $s = r_i - 1$ can only be in one of three layers: *z*-1, *z*, or *z*+1. Defining the notation:

$$\langle f(x,y) \rangle = \lambda_0 f(x-1,y) + \lambda_1 f(x,y) + \lambda_0 f(x+1,y) \qquad (3.24)$$

we can express a consolidated form for the end distribution function:

$$G_i(z, r_i | 1) = G_i(z, r_i) \langle G_i(z, r_i - 1 | 1) \rangle \qquad (3.25)$$

Note that there is nothing special about $s = r_i$. We very well could have had *s* equal any one of the segments and consider that the end of our chain. We also could have started our walk along the chain at $s = r_i$ as well. Therefore we arrive at a general recurrence relation for each of the endpoint distribution functions:

$$\begin{aligned} G_i(z, s | 1) &= G_i(z, s) \langle G_i(z, s - 1 | 1) \rangle \\ G_i(z, s | r_i) &= G_i(z, s) \langle G_i(z, s + 1 | r_i) \rangle \end{aligned} \qquad (3.26)$$

The placement of the first segment is not dependent on any prior positioning of the chain and its distribution function is simply the weighting factor $G_i(z, s)$. Thus, our boundary conditions for a free molecule are: $G_i(z, 1|1) = G_i(z, 1)$ and $G_i(z, r_i | r_i) = G_i(z, r_i)$. For an end tethered to a surface the segment, e.g. $s = 1$, is localized to a single layer adjacent to the surface, e.g. $z = 1$, such that $G_i(z, 1|1) = \delta_{1,z}$ where $\delta_{1,z}$ is one if *z* equal one and zero otherwise.

Eq. ( 3.26 ) gives the weight of segment *s* being in layer *z* taking into account all the possible walks beginning at either the $s = 1 \text{ or } r_i$. When considering this weight for a chain molecule we must remember that segment *s* being placed in layer *z* is the result of a walk starting on both sides of the chain. Therefore the actual weight for segment *s* is the product of both recurrence relations in Eq. ( 3.26 ): $G_i(z, s|1) G_i(z, s|r_i) / G_i(z, s)$. Dividing by $G_i(z, s)$ avoids double counting. To derive the volume fractions, recall that the layer volume fraction of molecule *i* is proportional to the overall weighting factor of its possible

conformations in Eq. ( 3.21 ). The weight for segment *s* above also is a complete weighting factor, considering all the possible conformations resulting in segment *s* being in layer *c*. Therefore we can express the volume fraction of segment *s* belonging to molecule *i* as:

$$\phi_i(z,s) = C_i \frac{G_i(z,s|1)G_i(z,s|r_i)}{G_i(z,s)} \qquad (3.27)$$

Calculating $\phi_i(z)$ simply requires summing over *s*, while $\phi_{Ai}(z)$ changes the sum to only over segments of type *A*. For the relationship between Eqs. ( 3.21 ) and ( 3.27 ), it is perhaps more clear to see that $\phi_i(z)\ r_i^c(z)$ is replaced by a sum over *s*. Therefore for segments in the same layer and of the same type, the sum will have $r_i^c(z)$ identical terms.

The normalization constant $C_i$ can be determined from Eq. ( 3.20 ) if the chemical potential of the species in the system and in bulk are known. Alternatively, if the number of molecules in the system are known Eq. ( 3.22 ) gives:

$$C_i = \frac{n_i}{LG_i(r_i|1)} = \frac{\theta_i}{r_i G_i(r_i|1)} \qquad (3.28)$$

where $\theta_i \equiv \sum_z \phi_i(z) = n_i r_i / L$. Finally, we can choose a reference potential such that all $G_i(z,s)$'s are unity when species *i* is in bulk solution. From Eq. ( 3.27 ) we find $\phi_i^b = r_i C_i$ after summing over all *s*.

It is typical to characterize the brush structure using the first moment of Eq. ( 3.27 ) to describe the chain length. For a lattice where *L* is constant for each layer, the characteristic chain length is given as:

$$h_i = \frac{\sum_z |z - z^*| \phi_i(z, r_i)}{\sum_z \phi_i(z, r_i)} \qquad (3.29)$$

where $z^*$ is the position of the first segment of the chain.

### 3.6. Segment Potentials

Eq. ( 3.27 ) can be completely solved once the form of the segment potential in Eq. ( 3.18 ) is known. This requires an expression for $U - U^*$ in terms of the segment volume

fractions $\phi_A(z)$. For most systems of interest quantifying the energy from mixing and electrostatics is sufficient to characterizing the total energy.

### 3.6.1. Energy of Mixing

To calculate the contribution of mixing the multiple species to the total energy we can use the well-known Flory Huggins parameter $\chi_{AB}$. $\chi_{AB}$ is a dimensionless quantity that quantifies the interaction energy that results from species *A* interacting with species *B* compared to a pure solution of both. In mean field theory we ignore long range correlations from the energy of mixing and only consider nearest neighbor contacts. More explicitly, for a binary interaction, $k_B T\chi_{AB} = 0.5(2E_{AB} - E_{AA} - E_{BB})$ where $E_{AA}$ and $E_{BB}$ are the interaction energies of the species in pure solution and 0.5 corrects for double counting of interactions. As an example, consider a case where the energy of species *A* and *B* in their respective pure states are equal. If mixing the two species together results in a more favorable state, $\chi_{AB}$ is negative.

Now consider a certain volume fraction of segment *A* in some layer z. Recall *Z* is the number neighboring sites for a lattice point. The average number of contacts that a segment *A* will have with segment *B* in layer *z* is given by $Z\langle\phi_B(z)\rangle$, where we have used the condensed bracket notation from Eq. ( 3.24 ). The total contribution of the mixing energy to the total energy with respect to bulk follows:

$$U_{mix} - U^*_{mix} = 0.5k_B TL \sum_{z,A,B} \phi_A(z)\chi_{AB}\left(\langle\phi_B(z)\rangle - \phi_B^b\right) \qquad (3.30)$$

where the term $0.5\phi_A(z)\chi_{AB}\phi_B^b$ is the energy of mixing when one places $L\phi_A(z)$ segments *A* in the homogenous bulk phase. It also requires that $U_{mix} - U^*_{mix} = 0$ when $\phi_A(z)$ is in bulk.

### 3.6.2. Electrostatic Energy

For a charged system, we must also consider the electrostatic contribution to the total energy. The impact of a segment of type *A* to the total electrostatic energy in a layer with respect to bulk is given as:

$$U_{A,el}(z) - U^{*}_{A,el} = 0.5L\phi_A(z)\, ev_A[\psi(z) - \psi^b] \qquad (3.31)$$

where $e$ is the elementary charge, $v_A$ is the valency of segment *A*, $\psi(z)$ is the electrostatic potential in layer *z* and $\psi^b$ is the electrostatic potential in bulk and ensures Eq. ( 3.31 ) is zero if the segments are in bulk phase. Determining the overall electrostatic energy of the system with respect to bulk involves summing over all the species in the layer and over all layers:

$$U_{el} - U^{*}_{el} = 0.5L\sum_{z,A}\phi_A(z)\, ev_A[\psi(z) - \psi^b] \qquad (3.32)$$

If we require that the bulk solution remains electroneutral, the final term vanishes.

There are two methods for determining the electrostatic potential in a given layer. The first involves solving the well-known Poisson Equation: $\nabla^2\psi = -\rho/\varepsilon$, where $\rho$ is the excess charge density and $\varepsilon$ is the dielectric permittivity. In one dimension $\rho(z)$ is the excess charge density in layer *z* and is derived from the volume percent of the species in that layer: $\rho(z) = e\sum_A v_A\phi_A(z)/b^3$, where $b^3$ is the volume of a lattice cell. The dielectric permittivity in a layer can be calculated by taking a linear combination of the permittivities of each of the individual molecules. It is also possible to assume that the permittivity is dominated by the contribution of the medium and is the same throughout, e.g. in water $\varepsilon = \varepsilon_0\varepsilon_{H2O}$. This is true for systems consisting mainly of medium.

We can use the geometry of the lattice to our advantage in solving the Poisson Equation for $\psi$. Its discrete form is expressed here:

$$\frac{\psi(z+1) - 2\psi(z) + \psi(z-1)}{b^2} = -\frac{\rho(z)}{\varepsilon} \qquad (3.33)$$

Thus we can solve for the electrostatic potential in one layer knowing the potential in the two adjacent layers and the volume fraction profile of the species. The boundary conditions of the system can be derived from the electroneutrality constraint, $\sum_{z,A} v_A\,\phi_A(z) = 0$. Gauss's law dictates that the field strength at the boundaries should be zeros such that $\psi(0) = \psi(1), \psi(M) = \psi(M+1)$.

An alternative method to determining the electrostatic potential involves the integration of the coulombic force to determine the work required to bring a charge from some reference point to a particular position in the system. The scalar quantity that results is defined as the electrostatic potential. From this treatment, the electrostatic potential felt by a discrete charge in layer *z* is given as:

$$\psi(z) = \sum_{z' \neq z}^{\text{all layers}} \frac{1}{4\pi\varepsilon} \frac{q_{z'}}{r_{z,z'}} \qquad (3.34)$$

where $q_{z'} = e \sum_A \upsilon_A \phi_A(z')$ and $r_{z,z'}$ is the absolute distance between the two layers. The boundary conditions are dictated by specific knowledge of the system's surroundings. As an example, consider Figure 3.3. An excess of negative charge is present at one side of

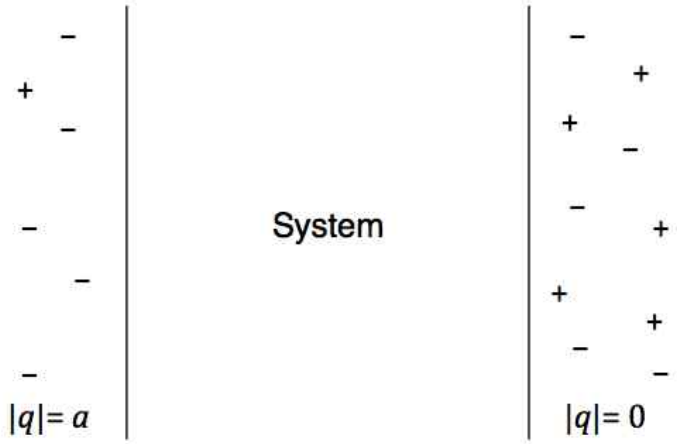


Figure 3.3. A system with left biased negative charge. *q* is the excess charge.

the system while the charges on the other side cancel each other out such that it applies no electrostatic bias. Implementing a boundary condition requires adding a constant to Eq. ( 3.34 ) that inversely decays with the distance from the negative excess charge and is proportional to the negative magnitude of the excess charge, i.e. $-a/r_{z,M<}$. Utilization of Eq. ( 3.34 ) does not require the constraint of electroneutrality but does entail prerequisite knowledge of the system to apply boundary conditions. Eq. ( 3.33 ) should be used for systems were the electroneutrality condition exists.

3.6.3. Determining the Explicit Form of the Segment Potentials

Eqs. ( 3.30 ) and ( 3.32 ) generally cover most type of systems and the sum of these two terms constitutes $U - U^*$ in Eq. ( 3.18 ), summarized here:

$$U - U^* = 0.5k_BTL \sum_{z,A,B} \phi_A(z)\chi_{AB}\left(\langle\phi_B(z)\rangle - \phi_B^b\right) + 0.5L \sum_{z,A} \phi_A(z)\, ev_A\left(\psi(z) - \psi^b\right) \qquad (3.35)$$

Dividing by *L* and applying the derivative causes all terms except those containing $\phi_A(z)$ to vanish. The result for the segment potentials is

$$\frac{u_A(z)}{k_BT} = u'(z) + \sum_B \chi_{AB}\left(\langle\phi_B(z)\rangle - \phi_B^b\right) + \frac{ev_A(\psi(z) - \psi^b)}{k_BT} \qquad (3.36)$$

where $u'(z) \equiv -\epsilon(z)$ is the unitless potential that requires the layer be filled. If the segment is uncharged $v_A = 0$ and there is no electrostatic contribution.

Eqs. ( 3.27 ) and ( 3.36 ) form a self-consistent loop. Knowledge of the segment potentials requires understanding of the segment volume fractions and vice versa.

3.7. Numerical Scheme

This set of implicit equations formed by the self-consistent field must be solved numerically. First we define our iteration variables as the set of segment potentials $\{u_A(z)\}$. As an initial guess all values are set to zero except for at $z = 0, M$ where a negative potential is supplied, as suggested by [59]. We choose values of approximately $-k_BT/5$. Then the segment profiles are found and the electrostatic potentials are calculated either from Eq. ( 3.33 ) or ( 3.34 ).

We then solve for $u'(z)$ via Eq. ( 3.36 ) using the current iteration variables used to calculate the current $\{\phi_i\}$. During the iterations $u'(z)$ may vary with the segment type. To ensure that the Lagrange Multipliers are only dependent of the layer number we define the following variable:

$$u'_A(z) = \frac{u_A(z)}{k_BT} - \sum_B \chi_{AB}\left(\langle\phi_B(z)\rangle - \phi_B^b\right) - \frac{ev_A(\psi(z) - \psi^b)}{k_BT} \qquad (3.37)$$

where $u'(z)$ is redefined as the average value of the set of $\{u'_A(z)\}$ in layer *z*. With this in mind, we can define the set of functions:

$$f_A(z) = 1 - \frac{1}{\sum_A \phi_A(z)} + u'(z) - u'_A(z) \qquad (3.38)$$

which equal zero only when the incompressibility constraint is reached and the potential is consistent with the segment profiles, guaranteed through Eq. ( 3.37 ) when $u'(z) = u'_A(z)$ for every *A*. The iteration algorithm is stopped when the maximum norm of $\{f_A\}$ is less than the tolerance $\eta = 10^{-7}$. When this steady state is reached, the equilibrium segment profiles are found.

Newton type iterative methods come in handy when dealing this type of problem. As we noted above, the iteration variables are the set of segment potentials. The goal is to solve the set of equations $\{f_A\}$ where the vector $\boldsymbol{f}$ is a function of the vector $\boldsymbol{u}$ for any *A*:

$$\begin{aligned} \boldsymbol{u} &= [u(1), u(2), \dots u(M)] \\ \boldsymbol{f}[\boldsymbol{u}] &= [f(1, \boldsymbol{u}), f(2, \boldsymbol{u}), \dots f(M, \boldsymbol{u})] \end{aligned} \qquad (3.39)$$

The variable $\boldsymbol{u}$ is updated via Newton's Method where the *n*+1th iteration is related to the *n*th iteration by the following expression:

$$\boldsymbol{u_{n+1}} = \boldsymbol{u_n} - \frac{\boldsymbol{f}[\boldsymbol{u_n}]}{\boldsymbol{f}'[\boldsymbol{u_n}]} \qquad (3.40)$$

For matrix first order derivatives $\boldsymbol{f}'[\boldsymbol{u_n}]$ is replaced by the Jacobian, $J$. Computing the Jacobian directly for large systems is computationally intensive, and a number of methods have been developed to provide and estimate to $J^{-1}$. One example is the Jacobian-free Newton-Krylov method, which enjoys the nonlinear convergence of other Newton methods but avoids explicit calculation of the Jacobian [61].

While the nonlinear convergence of Newton methods allow for fast calculations, their stability is dependent on the accuracy of the initial guess [62]. As an alternative, mixing schemes provide a more stable convergence path that is less dependent on the initial guess of the iteration variables. As a result the convergence zone is larger, but the overall process requires more iterative steps to reach the steady state due to smaller steps and is usually slower. The general scheme involves defining a residual vector between the input iteration variables $\{u_A(z)\}$ and the output vectors $\{f_A(z)\}$ of the same dimensions. For any *A* this looks like:

$$\boldsymbol{F_n} = \boldsymbol{f_n} - \boldsymbol{u_n} \quad (3.41)$$

The new variables are linearly mixed with the previous set via the following relation:

$$\boldsymbol{u}_{n+1} = \boldsymbol{u}_n + \alpha_n \boldsymbol{F}_n \quad (3.42)$$

where $\alpha_n$ is the mixing ratio and is usually constant for each iteration *n*. The convergence of the self-consistent calculation is now dependent on the mixing ratio. Generally lower values of $\alpha_n$ result in more stable iterations. Values closer to one result in updating the new input variables almost entirely with the previous output vectors. Anderson mixing is a particularly powerful mixing scheme that is a bit more complicated than the general mixing idea outlined above. Rather, it considers previous iteration vectors into each iterative calculation in an efficient way that leads to faster convergence [63].

We employ both methods in our numerical solution to the self-consistent field. To guarantee convergence for most situations we use Anderson mixing to a tolerance $\eta = 10^{-2}$. The output set of $\{u_A(z)\}$ then form the initial guess for the Newton-Krylov scheme until a tolerance $\eta = 10^{-7}$ is reached. Therefore our scheme has a wide zone of convergence with relatively quick calculation times.

### 3.8. Computational Aspects

When dealing with high-density molecular systems, i.e. grafted polymer chains with high grafting density and strongly charged polyelectrolytes, the individual $u_A$ for these segments can become quite large. As a result, the polymer chains are strongly stretched and the weighting factor $G_i(z,s)$ when segment *s* is of type *A* can become quite large. As Eq. ( 3.26 ) is recursively applied in the determination of the segment profiles, values can exceed the numerical range available to a computer. There are two common approaches to solve this problem.

The first is scaling the potential prior to application of Eq. ( 3.26 ) such that a new zero reference potential is appointed. The maximum $u_A$ is chosen as the reference potential so that all values are negative. While this solves the problem of exceeding the

numerical range overflow in one direction, there is the possibility that this method will scale the potential too much in the other direction such that $G_i$'s become much greater than unity. Now as Eq. ( 3.26 ) is applied, the numerical range is overshot on the high end.

The second method leaves the reference of the potentials alone but scales Eq. ( 3.26 ) for each column *s*. Wijmans and coworkers [64] have suggested a method that performs this scaling. They define the scaled version of Eq. ( 3.26 ) (denoted by tildes) as:

$$\begin{aligned} \tilde{G}_i(z,s|1) &= G_i(z,s)\langle \tilde{G}_i(z,s-1|1)\rangle c(s|1) \\ \widetilde{G}_i(z,s|r_i) &= G_i(z,s)\langle \tilde{G}_i(z,s+1|r_i)\rangle c(s|r_i) \end{aligned} \qquad ( 3.43 )$$

where $c(s|1)$ and $c(s|r_i)$ are constants chosen to keep the values of the end chain distribution functions close to unity. Unlike [64], we choose $c(s|j)$ to be unity for $s = 1, r_i$ and the maximum value of the current column $\tilde{G}(z,s|j)$ for all other *s*. This guarantees that each column is closer to unity since the scaling factor is based on the current column rather than the previous.

The reduced segment volume fraction $\tilde{\phi}$ is then found using the set of reduced propagator from Eq. ( 3.43 ) in Eq. ( 3.27 ). To obtain the actual segment volume fractions we normalize the result using the equation below:

$$\phi(z,s) = \sigma \frac{\tilde{\phi}(z,s)}{\sum_z \tilde{\phi}(z,s)} \qquad ( 3.44 )$$

where $\sigma$ is the grafting density for tethered chains.

### 3.9. Free Energy of Interaction

For our purpose, we are interested in determining the free energy for interacting systems involving grafted polymer chains. Recall both the temperature and chemical potential of our system is fixed by a surrounding reservoir. In this case the characteristic free energy is given by statistical thermodynamics as:

$$\Phi = F - \sum_i \mu_i n_i \qquad ( 3.45 )$$

The free energy *F* follows from the logarithm of the partition function in Eq. ( 3.12 ) as $-k_BT\ln Q/Q^*$. Using Eq. ( 3.19 ) to replace the first term in Eq. ( 3.12 ) so that the energy is in terms of the calculated variables for the segment potentials and profiles gives:

$$\sum_{i,c} n_i^c \ln\frac{L\lambda^c}{r_i n_i^c} = -L\sum_i \frac{\theta_i}{r_i}\ln r_i C_i + L\sum_{Z,A}\phi_A(z)\frac{u_A(z)}{k_BT} \qquad (3.46)$$

where we have used the definition of the segment volume fractions in Eq. ( 3.21 ). Substituting the result from Eq. ( 3.35 ) into *F* gives:

$$\frac{F}{Lk_BT} = \sum_i \frac{\theta_i}{r_i}\ln\frac{\theta_i}{G_i(r_i|1)} - \sum_{Z,A}\phi_A(z)\frac{u_A(z)}{k_BT} + 0.5\sum_{z,A,B}\phi_A(z)\chi_{AB}\left(\langle\phi_B(z)\rangle - \phi_B^b\right) + 0.5\sum_{z,A}\phi_A(z)\,\frac{ev_A(\psi(z)-\psi^b)}{k_BT} \qquad (3.47)$$

For interacting systems at some characteristic separation *M,* the energy of interaction is given as the difference between *F* at that distance and the systems in isolation:

$$\Phi^{\mathrm{int}} = F^{int} = F(M) - F(\infty) \qquad (3.48)$$

where the separation ∞ indicates a distance apart where the systems can be considered independent from each other. Notice that we avoid the calculation of chemical potentials in Eq. ( 3.45 ). Furthermore, the choice of the reference state is arbitrary since it also cancels out in Eq. ( 2.1 ). For those interested in the determination of the chemical potentials, see [60] for the equations of $\mu_i$ for mobile and grafted molecules. Eq. ( 2.1 ) suffices as a prerequisite for the calculation of other thermodynamic properties. However, it will be our main characterization for systems we investigate.

## 3.10. Determining the Free Energy of Interaction for Polymer Brush – Algae Pair

Eq. ( 2.1 ) grants us the ability to calculate the free energy of interaction between the anionic algae surface and the cationic polymer brush grafted to the paramagnetic iron oxide core. Before we calculate the energies at varying surface separations to obtain an overall interaction profile like the DLVO interaction curve for algae – algae interactions, we can make several approximations. First, we make the assumption that

our interaction is mainly electrostatic. Experimentally it was shown that the nanoparticle without the polymer were unable to induce flocculation among algae (see Section 1.1). Figure 6 from Section 1.1 also shows that the harvesting efficiency is a function of the charge of the system. Therefore we will only consider electrostatic contributions to the mean field potential in Eq. ( 3.36 ). All $\chi_{AB}$ are set to zero. Physically this signifies that all segment *A*'s energetically have no preference to be in a pure phase *A* or in a mixture with *B*. As a consequence, our brush is in the polyelectrolyte regime given by Pincus [34]. Pincus gives the characteristic length $L_p$ of the brush in this regime as $L_p \sim f^{1/2} N b$ where $fN$ is the number of monomers charged along the polymer backbone and $b$ is the Kuhn length of a monomer. If $R_a$ = 4 $\mu$m is the radius of curvature for the algae and $R_{pb}$ = 150 nm is the radius of curvature for the paramagnetic core, for all $N$ we consider $L_p < R_{pb} \ll R_a$ (see Figure 3.4). We can then simplify the model by considering the two surfaces locally flat. Since we are mainly interested with surface separations much smaller than $R_a$, this simplification does not cause significant error. Finally, we can exploit the symmetry of our system to only consider fluctuations perpendicular to the surface.

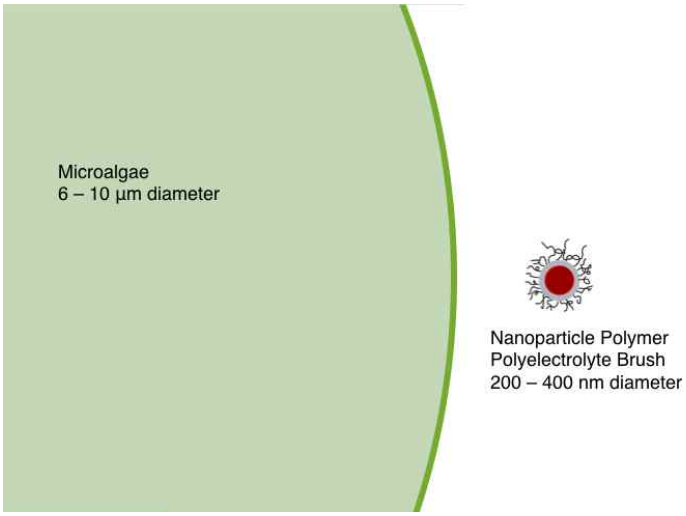


Figure 3.4. Pair interaction between the polymer brush and the algae surface shown roughly to scale.

With these simplifications in mind, for the SCFT calculation we place the two surfaces on either side of the boundaries of the lattice (see Figure 3.5). The space between

the two surfaces is divided into *M* layers where the layer number $z$ is related to the distance from the surface through the Kuhn length $b$, e.g. $D = Mb$. A negative charge is applied to both surfaces as determined by the zeta potentials (see Section 2.2.2.). For the silica-coated iron oxide grafting surface, the zeta potential was experimentally measured in deionized water to be -38.24 mV. We use a cubic lattice, where $\lambda_0 = 2/3$ and $\lambda_1 = 1/6$. The area of the interaction, given as the number of lattice sites in each layer *L*, is limited by the cross sectional area of the polymer brush, which in turn is determined by the radius of the core and given as $4\pi R_{pb}^2/b^2$.

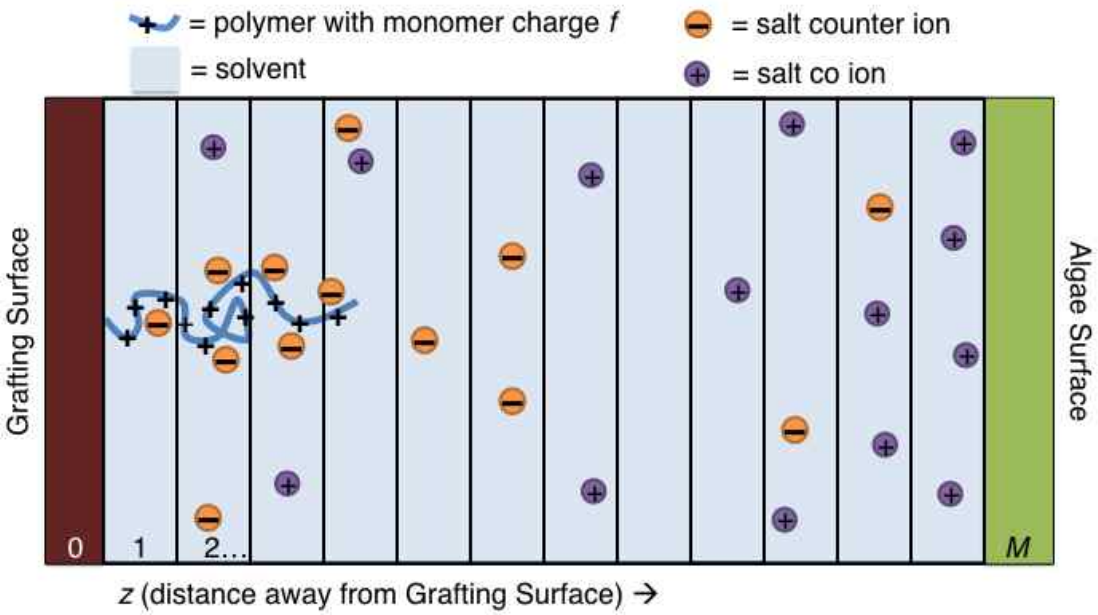


Figure 3.5. Diagram of the system divided into *M* layers between the two surfaces.

3.10.1. Free Energy for Constant Degree of Polymerization, *N*, Varying the Charge

First we investigate the effect varying the monomer charge fraction *f* has on the free energy of interaction between the nanoparticle polymer polyelectrolyte brush (NPPB) and the algae. Recall that we are not arbitrarily choosing which monomers along a polymer backbone are charged. Rather, each is given the exact same fractional charge. For instance, for a monomer charge fraction of 0.75, each monomer unit has a charge of +0.75*e* C. Experimentally harvesting efficiency was measured for *N* = 245 where *f* = 0.25, 0.5, 0.75, and 1 (see Section 1.1). We choose theoretical parameters of degree of polymerization (*N* = 250) and the charge fraction, *f* to mimic experiment.

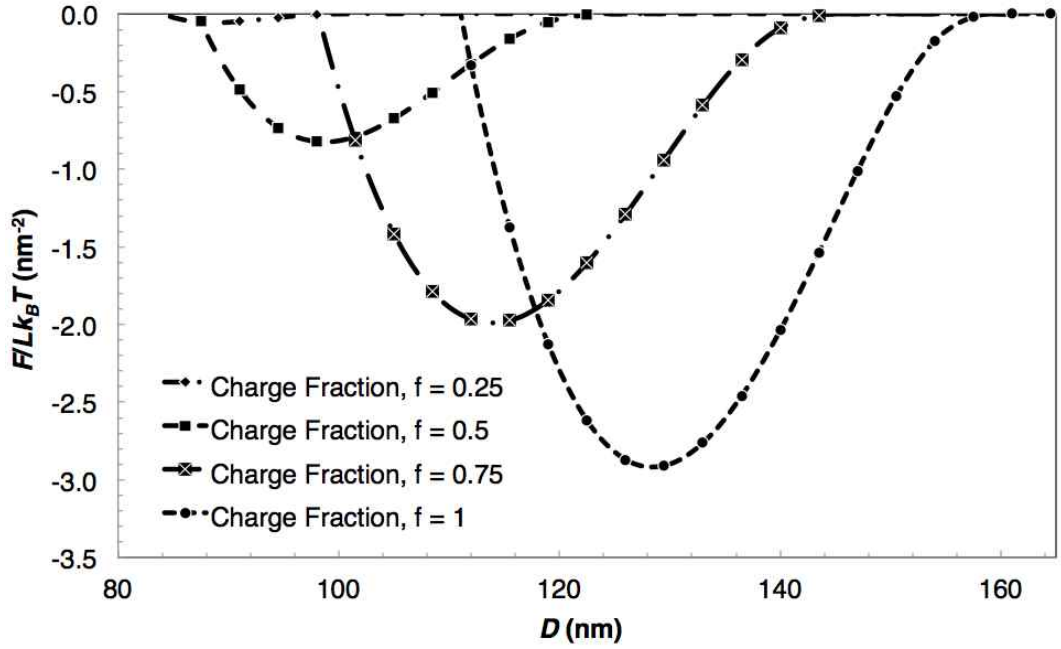


Figure 3.6. Free energy of interaction $F$ per unit area $L$ versus surface separation $D$. Points mark sampled $D$, while the line is interpolated using a smooth curve fit. $N = 250$.

Figure 3.6 provides a graphical representation of the SCFT results for the free energy of interaction for varying monomer charge fractions. As the algae surface approaches the free end of the polymer brush an energy well begins to form. Figure 3.7 gives $D$ at contact as well as the brush height determined by the first moment in Eq. ( 3.30 ). From Figure 3.7 it is evident that the adsorption of the brush onto the surface coincides with the formation of the well. This is a result of minimizing the electrostatic contribution to the free energy in Eq. ( 3.47 ) as oppositely charged bodies come in contact, lowering the excess charge in a layer. This adsorption process becomes repulsive when the height is constrained significantly such that entropic spring nature of the brush starts to resist further compression from its equilibrium position (i.e. no algae wall). Also, as the monomers are forced together like-charge repulsion between the repeating units increases. The energy well depth for charge fraction equal to 0.25 is much smaller than the higher charge fractions due to the fact that characteristic brush height is much smaller. Therefore when the algae wall comes in contact with the free end of the polymer brush, the brush does not have as much volume to compress before the interaction becomes repulsive. For higher charge fractions, this interaction becomes repulsive

when the brush is approximately 90% of its reference height ($D \rightarrow \infty$) whereas for charge fraction equals 0.25 this occurs at approximately 96%.

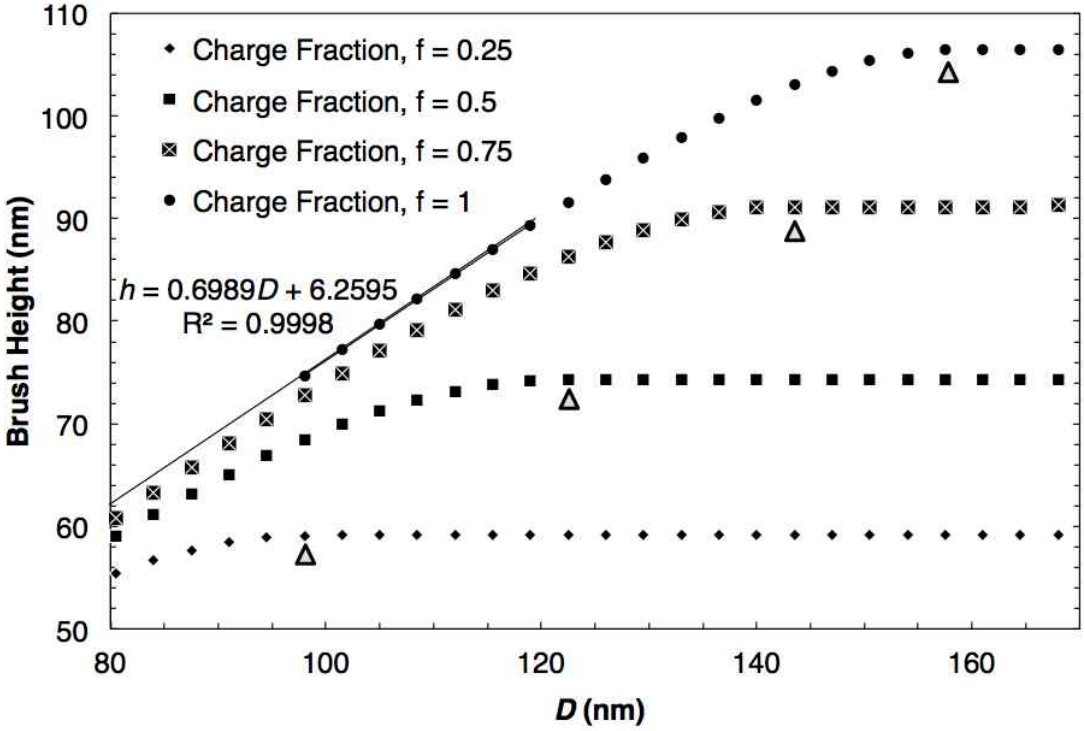


Figure 3.7. Brush height versus surface separation *D*. Triangles denote when the brush first comes in contact with the algae surface. For $f = 1$, a linear extrapolation of the data is given for comparison purposes as *D* goes to 80 nm. The equation of the fit is given in terms of the brush height (*h*) and *D*.

Unlike the brush height, the length of the brush is not weighted by the segment volume fractions and determines the point of brush – algae contact depicted in Figure 3.7. Figure 3.8 gives the polymer brush profile from the grafting surface when the molecule is isolated (i.e. $D \rightarrow \infty$). The remaining volume fraction consists of mostly solvent, with relatively small traces of salt ions. This gives a more explicit picture of the polymer profiles given by the brush heights. When the monomers have a valency of +1, the similar charge repulsion along the backbone stretches the polymer farther away from the surface compared to lower charge fractions. This leads to lower volume fractions in the interior of the brush. More cationic charges are able to adsorb onto the surface as *D* is decreased before the energy minimum is reached. Figure 3.9 depicts the brush profile for each charge fraction that corresponds to the minimum of the free energy curves in

Figure 3.6. The peak at the free end indicates the preferential adsorption of the cationic polymer units to the negatively charged algae surface. Stronger charged monomers demonstrate a stronger peak due to the increased electrostatic attraction. As a result, monomers with valency of +0.25 weakly interact with the surface leading to profile behavior similar to that in Figure 3.8.

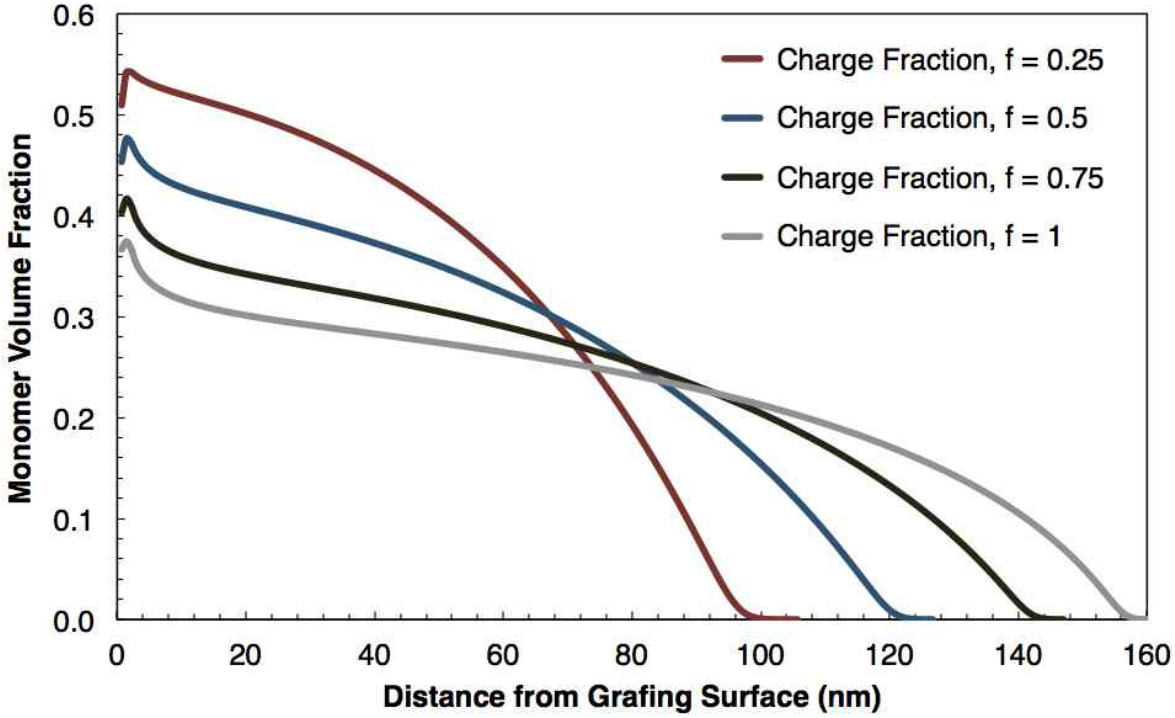


Figure 3.8. Polymer brush profile at $D \rightarrow \infty$ for varying monomer charge fractions.

On a per unit area basis, we can conclude that as the charge fraction is increased, the pair interaction potential is more energetically favorable. This is not an obvious result. Recall that the surface charge density of the algae surface is $10^{-3}$ C/m$^2$. This translates to 160 nm$^2$ per negative charge. For a chain with $N$ = 250 and the charge fractiony at one, the chain would have to adsorb onto an area of 40,000 nm$^2$ for all of it's charges to be spatially matched with a counter ion on the algae surface. While this amount to only 0.06% of the algae surface area, this is an immense space to cover for a single tethered chain. In comparison, the radius of gyration $R_g$ for a free polymer in a theta solvent is given as $R_g^2 = Nb^2/6$, or roughly 1% of 40,000 nm$^2$. Therefore the minimums in the free energy curve are a result of a slight minimization of the electrostatic energy compared to reference when the two surfaces are infinitely apart.

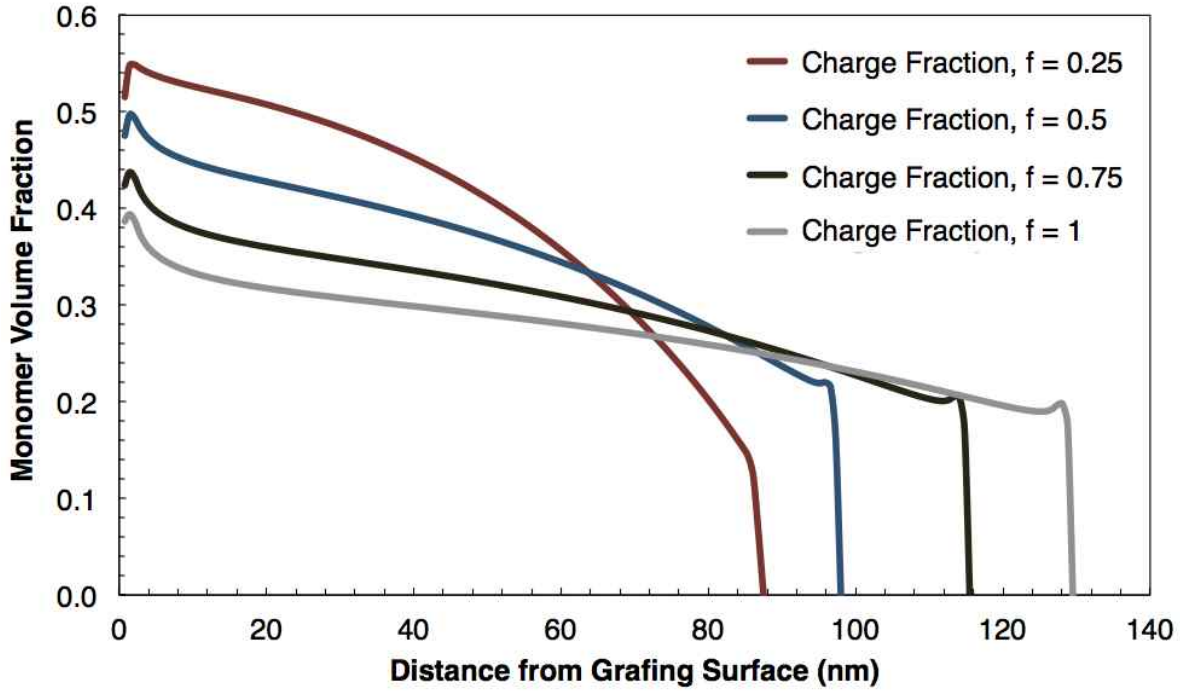


Figure 3.9. Polymer brush profile at free energy minimum in Figure 3.6. The polymer chain is compressed by the adsorbing boundary conditions caused by the presence of an algae wall at a distance $D$ when the monomer volume fraction drops to zero.

While on a per unit area basis there may be significant differences between the pair interactions, as a whole entity there is no significant variance. For the former case, these free energy of interaction adsorption wells are on the order of the thermal energy. For the complete adsorption between our two spheres, the area of the polymer brush limits the area of interaction. If approximately half the polymer brush surface interaction with the algae cell wall, $L \approx 2\pi R_{pb}^2$ = 141,372 nm$^2$. This does not include the range of the electrostatic forces, given by the Debye length in the medium. Thus the adsorption well depth is at least $10^6 k_B T$ for any of the charge fractions. The energy depth is so much greater than the thermal energy that the adsorption is irreversible once any of the NPPB's come in close proximity to an algae cell. There is no specificity in the pair interactions between different charge fractions and algae that would explain the experimental harvesting efficiencies varying the charge in Section 1.1. Thus, a missing piece of information and analysis is required to explain experimental results. However, we now have calculated the free energy of interactions varying the charge along the polymer backbone for constant degree of polymerization.

3.10.2. Free Energy for Constant Monomer Charge Fraction, varying *N*

In determination of the optimal brush structure for the system, the degree of polymerization is an experimentally controlled parameter that can be optimized in addition to the monomer charge fraction. Experimental results in Section 1.1 indicate that increasing *N* causes higher harvesting efficiencies to be reached at lower NPPB concentrations. This escalation trails off once $N > 200$ as little difference is improvement is seen between $N = 198$ and $N = 250$. To model the ranges of *N* in our experimental system and to compare to experimental observations we set a low value for *N* at 50, an intermediate value at 100, and two at the aforementioned transition where little change in the harvesting efficiency is observed at 200 and 250. The monomer charge fraction is constant at 0.75 for all results in this section.

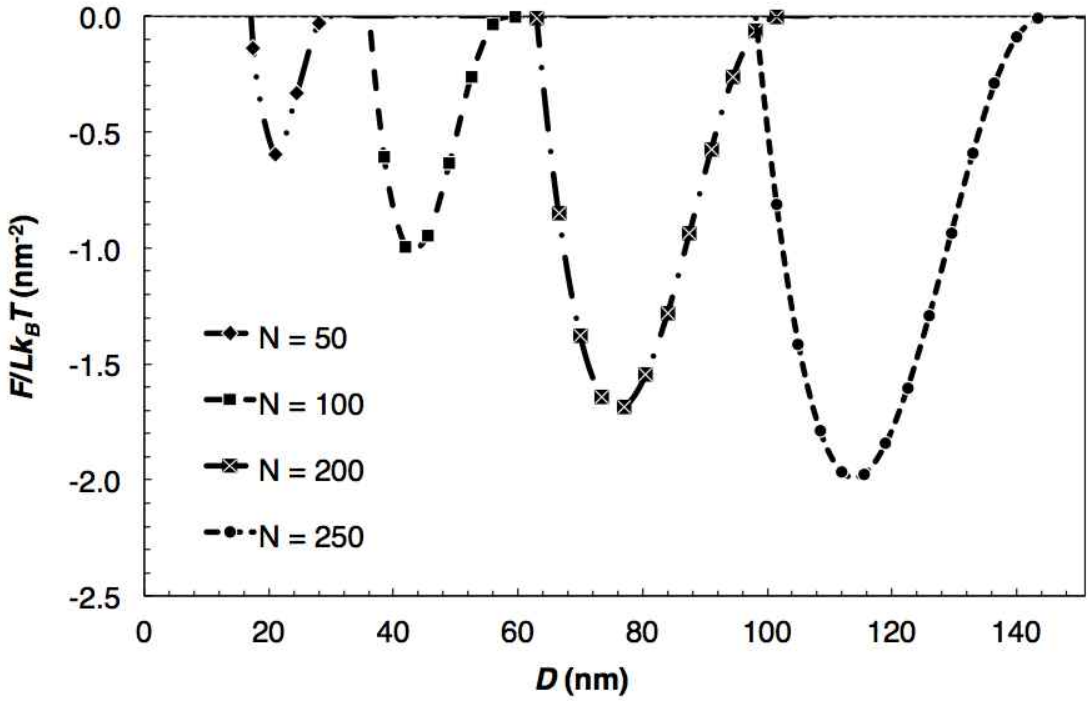


Figure 3.10. Free energy of interaction *F* per unit area *L* versus surface separation *D*. Points mark sampled *D*, while the line is interpolated using a smooth curve fit. Monomer charge fraction, $f = 0.75$.

The free energies of interaction for the range of studied *N* is given in Figure 3.10. As was the case in Section 3.10.1, the per unit area pair interactions between the charged polymer chain and the algae surface form energy wells on the order of the thermal energy of the system. The formation of this energetically favorable bond once

again coincides with the adsorption of the NPPB on the algae surface. The point of contact between the two is marked in Figure 3.11, where we have divided *D* by *N* due to the disparity in sizes between the different *N*. Since the polyelectrolyte brush length scales linearly with *N*, it is expected that the point of contact is at the same *D*/*N* for each *N*. Doubling the number of monomers doubles the length, with doubles *D* as well.

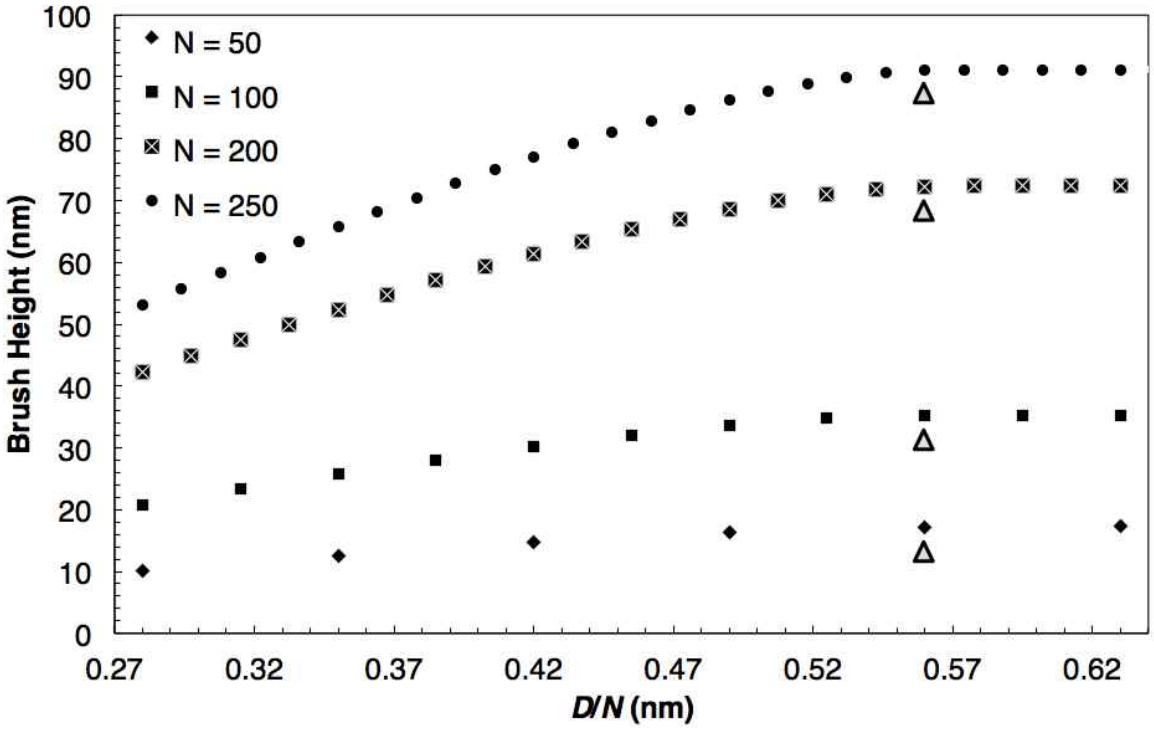


Figure 3.11. Brush height versus the ration of surface separation *D* and *N*. Triangles denote when the brush first comes in contact with the algae surface.

Furthermore, Figure 3.10 demonstrates that the addition of more monomeric units along the chain backbone results in larger binding energies (deeper adsorption wells). Unlike the free energies for varying charge fractions in Figure 3.6, the binding energy scales linearly with the variable *N*. For instance, doubling the degree of polymerization from 50 to 100 increases the energy well depth by the same factor as when we double the degree of polymerization from 100 to 200. We suspect that the brush length, which for constant monomer charge scales linearly with *N* as well, leads to the differences in binding energy.

Figure 3.12 shows the polymer profile at infinite separation for varying *N* while Figure 3.13 gives the profile at their respective free energy minimums. The brush for

each *N* compresses by roughly the same factor of one quarter from its reference state (Figure 3.12) to its length at the free energy minimum (Figure 3.13). The difference is that one fourth of the brush with *N* = 250 is five times greater than one fourth of the brush with *N* = 50, for example. Therefore after original contact brushes with higher *N* can compress over a longer range, exposing more of the positive monomer units to the anionic algae surface before the elastic pressure of the brush causes the interaction to be repulsive. The peaks at the free end of the brush in Figure 3.13 are further proof of adsorption as the cationic monomers favorable stick to the algae surface. As we increase *N* this trend should continue.

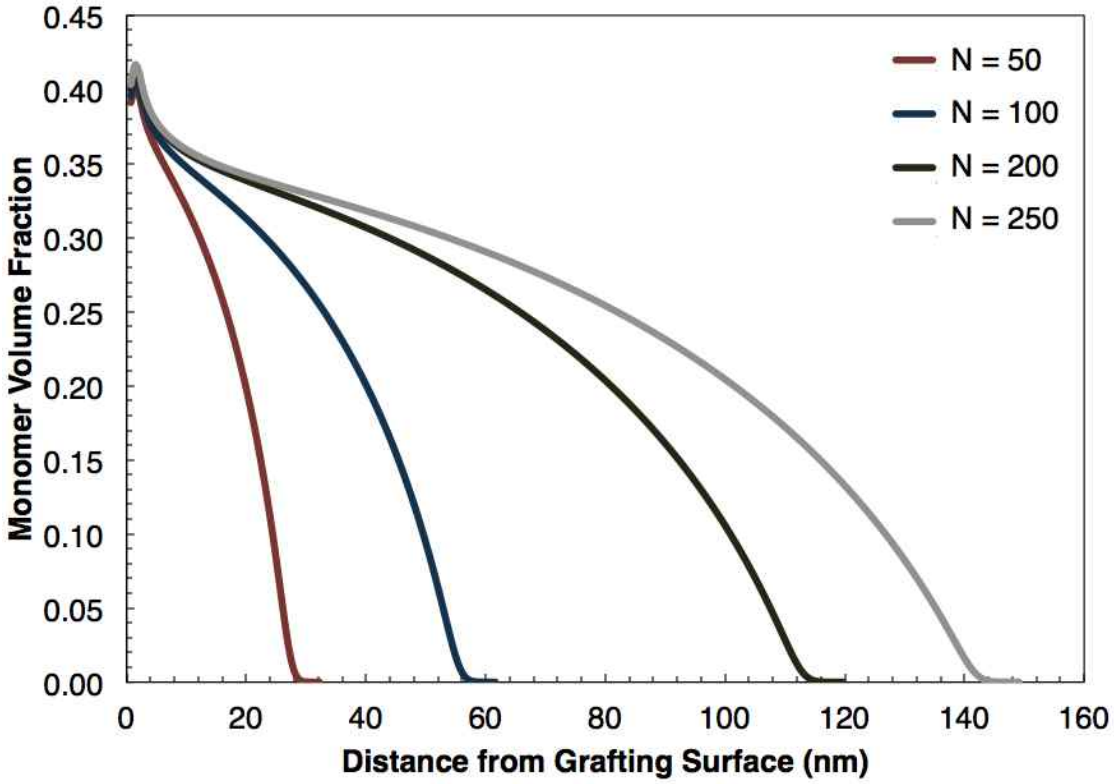


Figure 3.12. Polymer brush profile at $D \rightarrow \infty$ varying the degree of polymerization, *N*.

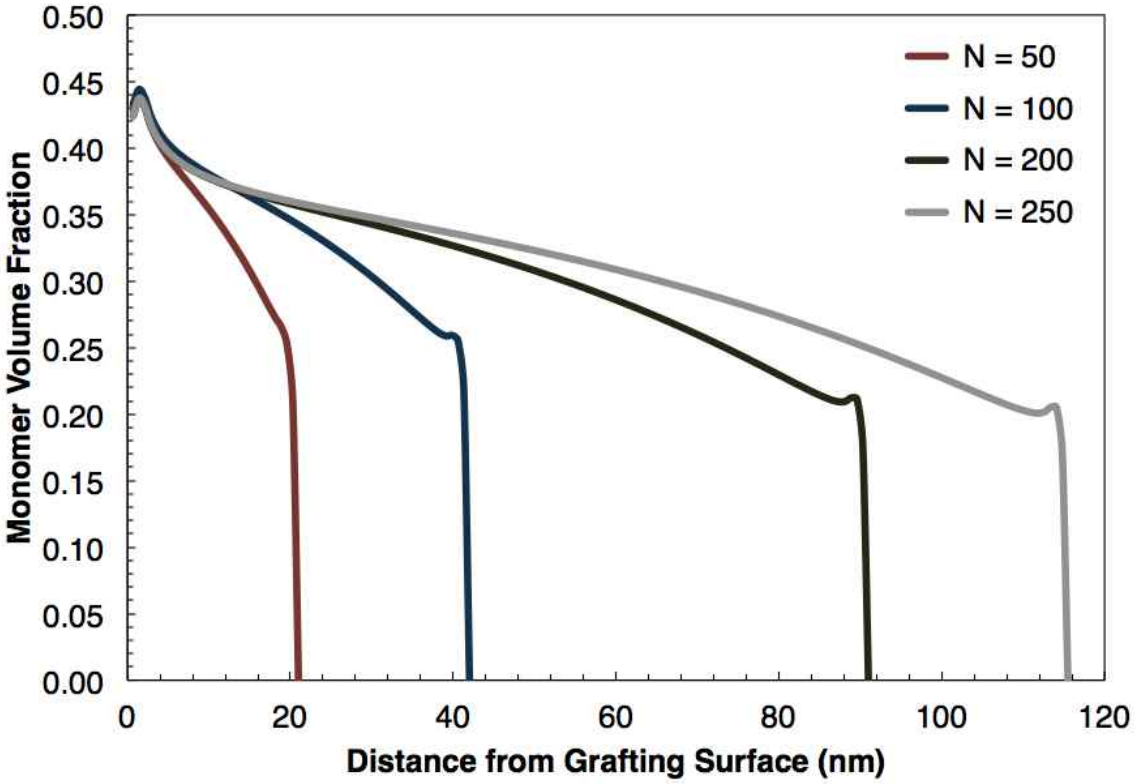


Figure 3.13. Polymer brush profile at free energy minimum in Figure 3.10. The polymer chain is compressed by the adsorbing boundary conditions caused by the presence of an algae wall at a distance *D* when the monomer volume fraction drops to zero.

However, once again we are faced with the shortcomings of the pair interaction to provide any specificity between the brush structure and the harvesting efficiency. As we mentioned above, the overall interaction between the algae and the brush is on the order of $10^6 k_B T$. The binding energies in Figure 3.10 are irreversible. Once any of the brushes come in contact with an algae surface, they will stick. There is no difference for any of the *N* when it comes to the ability to bind to algae. Further analysis is required to determine how *N* influences the harvesting efficiency.

### 3.11. Polymer Brush – Brush Interactions

To understand a typical NPPB – NPPB interaction we must first analyze the typical surface separations where the pair interactions occur. To do this, we can use the experimental harvesting results depicted in Section 1.1 to estimate the number of NPPB per algae surface. Between similarly charged species, minimization of the free energy of

interaction would result in an equilibrium distribution where the NPPB distribute themselves evenly along the algae surface such that their surface separation is maximized. If we assume this distribution, knowing the number of NPPBs per algae will lead us to the average surface separation of a pair interaction.

To get a range of the typical surface separations, we analyze the number NPPB per algae for the lowest and highest NPPB concentration for our brush structures in Section 3.10 close to 100% harvesting efficiency when the number of NPPB is the highest. These two extremum correspond to when the degree of polymerization is 250 and 50, respectively. For the degree of polymerization at 50 we can approximate it with the experimental results for 65. For degree of polymerization 250 the concentration is approximately 0.1 mg/mL when the harvesting efficiency is almost 100%. For 65, the concentration is approximately 0.45 mg/mL. The majority of the weight arises from the paramagnetic $Fe_3O_4$ core. At RT, the density of magnetite is 5.1 g/mL [65]. With a radius of 150 nm, each NPPB weighs approximately $7.21 \times 10^{-11}$ mg. The number density for the two extremum follows directly from this value. Experimentally there are $25 \times 10^6$ algae per mL [23]. Therefore for a NPPB with degree of polymerization 250 or 65 the NPPB per algae is about 55 or 250, respectively.

Now that we know the approximate coverage of the NPPB on the algae surface we can determine the range of surface separations for a pair interaction. For our algae with a radius of 4 $\mu$m, the surface area is $201 \approx 200\ \mu m^2$. If we assume that the NPPBs distribute themselves evenly across the surface, there should be one for every 3.6 $\mu m^2$ for the larger NPPB and 0.8 $\mu m^2$ for the smaller NPPB. Consequentially, our surface separations for our pair interaction on an algae particle range from 600 nm for degree of polymerization at 65 and 1600 nm for 250. Given the brush lengths in Figure 3.12, it is evident that we do not have to worry about brush-brush physical contact when calculating pair potentials for typical interactions in our system when considering NPPB on the same algae. Furthermore, if two algae have the same surface coverage of NPPB we can assume that as the two approach each other they will rotate to minimize their free energy by maximizing separations between each other's NPPBs as well (Figure 3.14). The range of surface separations on a single algae surface leaves enough space be-

tween each NPPB such that the approaching algae's NPPBs are not forced to come into contact with another NPPB at any algae surface separation. If they are not forced to come in contact, the configuration at equilibrium will minimize the free energy such that none come in contact.

Therefore, for determining the pair interactions we can ignore any surface separations less than two times the brush length of the NPPB. This allows us to simplify our approach for explicitly calculating free energies of interaction for a wide range of surface separations possible between two NPPB. Using SCFT, which allowed us to model the elastic behavior of a brush as it comes in contact with a wall, for this wide range of separations is computationally expensive. We can instead treat the NPPB as colloids with a charge given by the number of charged monomers tethered to the surface. In order to avoid severe bias of the charge placement, we situate the simulated surface of the NPPB colloid (where all the charge is concentrated) at the brush height *h*, the first moment of the distribution of the monomers. The charge on the grafting surface is negligible compared to the polymer charge, and we will ignore it. We will also ignore the van der Waals interactions since they only come into effect at close surface separations. All interactions occur in water with pH = 7 at RT.

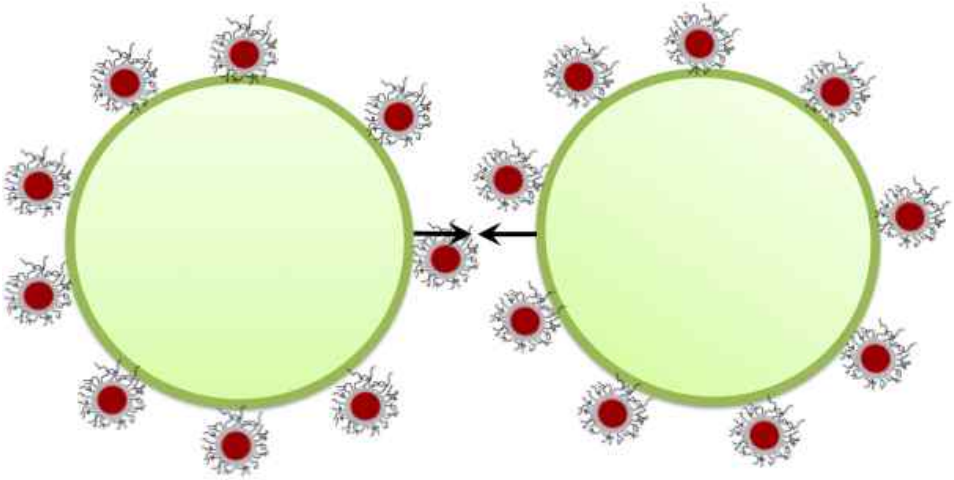

Figure 3.14. Two NPPB covered algae approaching each other with a configuration that avoids NPPB pair contact.

How the NPPB – NPPB interactions will be explicitly calculated depend on how we model the harvest efficiency. Therefore we will discuss how we go about exactly cal-

culating the value of the pair interactions in Chapter 4, when we model the harvesting efficiencies. The nature of the NPPB self-interactions discussed here will be useful then.

## 3.12. Conclusions

With the knowledge gained here on the interactions involving the polymer brush, we can now move forward in determining a method to model the experimental results of the harvesting efficiency for different brush structures. The magnitude of the NPPB – algae adsorption energies suggest that adding NPPB will immediately cause the algae cells to be coated with these particles. We now must find a way to determine how many NPPB must coat the algae cells before they can be harvested. From these observations we hope to be able to explain experimental data and suggest how the structure of the brush influences the harvesting efficiency of the experimental set up.

# CHAPTER 4
# DETERMINING THEORETICAL HARVESTING EFFICIENCY

So far we have only examined the pair interactions between the relevant bodies in our system. However, our main goal was to explain how the brush parameters influence the harvesting efficiency. In this chapter we will describe how we can make this connection.

## 4.1. Introduction

From what we have learned so far, we know that microalgae repel each other strongly due to the like-charges present on their surface. Also, when the nanoparticle polyelectrolyte polymer brush (NPPB) adsorbs onto the algae surface, the depth of the free energy well for attraction between microalgae and the brush is many times greater than $k_BT$. This suggests an irreversible binding event once a polymer brush comes in contact with an algae surface in solution. However, both of these results do not tell us how brush structural parameters determine harvesting efficiency.

In the lab setup, harvesting efficiency is determined by the number of cells that can be removed from solution relative to the original amount. A cell is removed from solution if: 1. It forms in a cluster with other algae and 2. If the number of magnetic NPPBs in that cluster is large enough such that the magnetophoretic force of the cluster outweighs the random Brownian forces dispersing it. For now, let us assume that the number of NPPBs required to form any cluster of algae is sufficiently large enough to be drawn in by the magnet.

Now harvesting efficiency is solely dependent on the ability of the cells to form clusters (flocculate). To look at the dependency of flocculation versus different brush parameters for a many body system, we take two approaches. The first involves considering when the effective charge of an algae surface is completely screened by the NPPBs. The second involves taking two bare algae as a reference system, then coating

the surfaces with a uniform density of NPPBs and determining when the net force between these two bodies becomes negative (attractive). We outline the two approaches and give results here.

## 4.2. Harvesting Efficiency as a Variable of the Effective Algae Charge

Each NPPB carries a given amount of cationic charge along the polymer backbone. Coating the anionic algae surface with NPPB reduces the effective charge. As the effective charge of the algae approaches zero, coulombic repulsion between algae vanishes and the algae can aggregate. We saw in Section 2.5.1 that for algae in water the effective charge must go close to zero before they can form pair aggregates in the primary minimum of the DLVO curve. We can then determine the amount of cationic charge needed to reduce the effective charge of the algae to zero and back out the minimum required degree of polymerization, grafting, and charge fraction of the polymer chains on the NPPB.

We realize the limitations of this model will cause the predicted NPPB required to screen the effective charge on algae to be severely underestimated due to the range of electrostatic interactions in a medium. Inherently assumed in this theoretical model is that the positive charges belonging to the NPPB are unrestricted mobile entities. Stated differently, when we add one NPPB brush to the system, we are “allowing” each charge on that brush to pair with a negative charge anywhere on the algae surface. However, the effective interaction range of the positively charged monomer attached to the NPPB is set by the characteristic decay of the electrostatic field of the charge given by the Debye length. Thus we consider that the NPPB has an effective charge radius. Beyond this effective charge radius the positive charges of the brush are not felt. The NPPB brush is only “screening” a fraction of the equivalent number of negative charges on the algae surface. “Screening” here refers to changing the interaction with another algae from repulsive to attractive on the length scale of a Debye length or shorter.

To get an idea of the order of magnitude the number of NPPB per algae required to screen the effective charge is underestimated by, we must determine this effective charge radius around the NPPB and the number of charges along the algae surface it

can screen. As we discussed in Section 3.11, let us assume that the charge is localized to the imaginary surface given by the first moment of the polymer brush profile at equilibrium, or the brush height. From the brush height results in Figure 3.7 and Figure 3.11 we obtain that this number is on the order of 100 nm. The end-to-end diameter of the polymer brush is then approximately 400 – 500 nm. For pH = 7 water, we have already shown that the Debye length is 973 nm. Therefore the effective charge radius, which is the sum of the radius of the polymer brush (200 – 300 nm) and the Debye length, is between 1200 – 1300 nm. If we estimate the algae surface as locally flat, then the effective charge surface screening area of the brush on the algae surface is equal to π(effective charge radius)$^2$ ≈ 5 $\mu$m$^2$. The actual number of algae charges that are screened by this effective charge disc can be gleaned from the number of charges in this area. With *e* being the elementary charge of an electron, there are about (-10$^3$ m$^2$/C)(10$^{18}$ nm$^2$/m$^2$)(*e*) = 160 nm$^2$ per charge on the algae surface. Therefore the NPPB effective charge area covers 3×10$^4$ negative charges on the algae surface. The number of charges on the NPPB with degree of polymerization *N* and monomer charge fraction *f* is given as:

$$\frac{0.41\ \text{chains}}{\text{nm}^2} * \frac{4\pi R_{NPPB}^2}{1\ \text{NPPB}} * \frac{N\,\text{monomers}}{\text{chain}} * \frac{f\ \text{charge}}{\text{monomer}} = 1.2\times10^5\ N\,f \qquad (4.1)$$

where for our NPPB the graft density is 0.41 chains/nm$^2$ on the surface and $R_{NPPB}$ = 150 nm. With *N* and *f* on the order of 100 and 1, respectively, the number of NPPB charges is about 1×10$^7$. The NPPB is sequestering only a fraction equal to 3×10$^4$/1×10$^7$ = 0.003 or 0.3% of the charges it could screen if its positively charged monomers were completely mobile. We will be under-counting the number of NPPB per algae required to screen the charge by an order of 10$^3$. With this in mind, we will continue on with the model but tread carefully when making conclusions on the NPPB per algae data.

We can also determine from this information the number of possible binding spots where the NPPB can adsorb to the algae surface and not feel the effect of any other NPPB. With a radius of 4 $\mu$m, the algae has a surface area of 200 $\mu$m$^2$. The number of these binding sites then is about 40. Since the number of NPPB charges in the effective charge area (determined by the effective charge radius) is much greater than the number of algae charges in that area, only one NPPB is required at each of these

binding sites before the effective charge is screened using our model. This is true for any NPPB structure studied here. Thus we go forward realizing the deficiencies of this model to accurately predict the actual number of NPPB per algae and mainly examine the scaling of the results with *N* and/or *f*.

4.2.1. Matching the Number of Positive and Negative charges

We found that each algae cell has a surface charge density on the order of $-10^{-3}$ C/m$^2$ (Section 2.2.2). Therefore the number of charges on each cell is given as:

$$-\frac{10^{-3}\mathrm{C}}{\mathrm{m}^2} * \frac{4\,\pi\,R_{alg}^2}{1\ \mathrm{algae}} * \frac{1\ \mathrm{charge}}{-1.6019\times10^{-19}\mathrm{C}} = 1.3\times10^{6} \qquad (4.2)$$

where $R_{alg}$ = 4 $\mu$m and we have carried the number of charges to an extra significant figure since this is a crude model.

The charges on the algae are completely screened when the following equality holds true:

$$\frac{n_{NPPB}}{n_{alg}} = \frac{10}{Nf} \qquad (4.3)$$

If the number of algae, $n_{alg}$, and N and f are all specified the number of NPPB required for Eq. ( 4.3 ) to be true, $n_{NPPB}$, can be determined. When Eq. ( 4.3 ) is not satisfied, the remaining effective charge of the algae can also be interpreted as a harvesting efficiency. As an example consider when 0.25 of the effective algae charge is screened. At two simplified extremes, this can be interpreted as either 25% of the charge on each algae is screened or 25% of the algae have their charge completely screened. Since we are treating flocculation as the sole criteria for algae to be harvested, this latter number suggests 25% of the algae can flocculate and thus be harvested.

Eq. ( 4.3 ) also demonstrates that the number of NPPB per algae should be on the order of 0.1. With the correction factor discussed earlier, we expect experimentally this number should actually be on the order of 100. To reinforce the point that the charges on the NPPB are limited by the range of the electrostatic force in medium, with a characteristic decay length given by the Debye length, let us imagine what the former

case would physically signify. If only 0.1 NPPB were needed per algae, then 1 NPPB could aggregate 10 algae. However, when a NPPB bridges the gap between two algae surfaces, the diameter of the effective charge volume is smaller than the diameter of the algae. Therefore, this effective charge volume does not extend past these two algae and the NPPB cannot screen any other algae.

Figure 4.1 and Figure 4.2 show the number of NPPB per algae varying the monomer charge fraction and degree of polymerization, respectively. For convenience, the experimental results originally depicted and discussed in Section 1.1 are reproduced alongside the relevant theoretical calculations. For varying degree of polymerization at constant charge fraction, experimental harvesting efficiencies were normalized to the number of NPPB per mL of solution using the average weight of a NPPB to avoid discrepancies in the different molecular weights of the chain. As we expect from Eq. (4.3), $n_{NPPB}$ when all of the algae charges are screened varies linearly with both *N* and *f* in the theoretical calculations. As an example, doubling either *N* or *f* decreases the NPPB per algae required by one half.

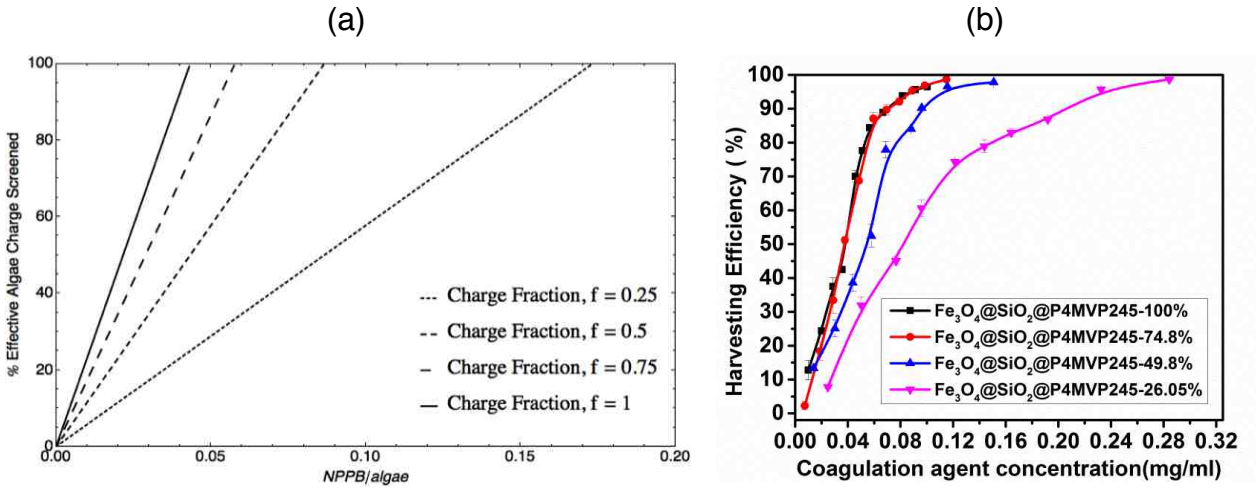


Figure 4.1. Theoretical and experimental results for constant *N* = 250 varying the monomer charge fraction (*f*). (a) Number of NPPB per algae versus percentage of algae charge screened varying *f*. (b) Experimental calculations of harvesting efficiency varying the monomer charge fraction (given by the percentages).

However, as we see from the experimental results the response is not linear with respect to either. For varying charge fraction, *f*, increased by a factor of 1.9 from 26.05% to 49.8%, the coagulation agent concentration when 100% of the algae is harvested (in

our theoretical case this corresponds to when the effective charge is completely screened) is decreased by a factor of 0.56 (NPPB concentration at $f$ = 49.8% divided by concentration at $f$ = 26.05% at equal harvesting efficiency at 100%). Theoretically this ratio is 0.5. When $f$ is increased by a factor of 1.5 from 49.8% to 74.8%, the coagulation agent concentration when 100% of the algae is harvested is decreased by a factor of 0.75. Theoretically this ratio is 0.67. Finally, while theoretically we predict that the coagulation concentration at complete harvesting efficiency changing from $f$ = 0.75 to $f$ = 1 should diminish by a factor of 0.75, the experimental results for $f$ = 0.75 and 1 are practically identical. We can see experimentally that as we increase the charge, the response in the harvesting efficiency versus NPPB concentration is not linear in $f$. Note that each of the NPPB should have the same weight so any change in the units along the concentration of coagulant should not change the experimental ratios. As a consequence, if the algae concentration is held constant, this applies to converting mg/mL of agent to NPPB/algae as well.

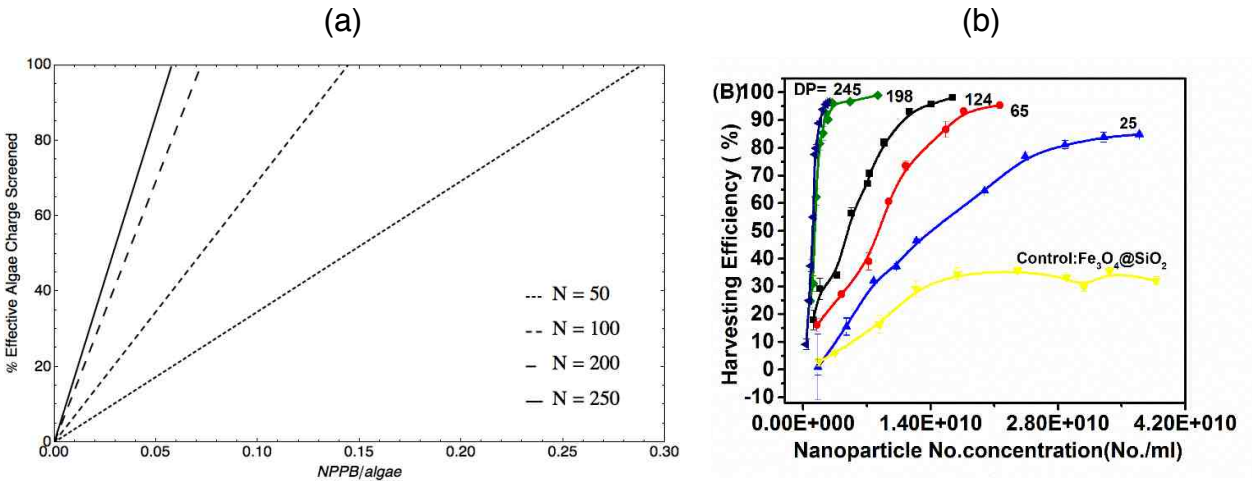


Figure 4.2. Theoretical and experimental results for constant $f$ = 0.75 varying the $N$. (a) Number of NPPB per algae versus percentage of algae charge screened varying $N$. (b) Experimental calculations of harvesting efficiency varying $N$.

For varying degree of polymerization, when $N$ is increased by a factor of 1.9 from 65 to 124, the coagulation agent concentration at equal harvesting efficiencies is approximately decreased by a factor of 0.67. Theoretically we predict that this value should be closer to one half. In comparison, doubling the degree of polymerization again from 124 to 245 in experiment results reduces the NPPB concentration at equal harvest-

ing efficiencies by 0.42. We can also compare directly the change in degree of polymerization from 198 to 245. Experimentally we see no discernible variation between the NPPB concentrations at equal harvesting efficiencies. Theoretically we predict that the NPPB concentrations should vary by a factor of 0.81 as the number of monomers is augmented from 198 to 245. Therefore, experimental results are nonlinear in *N* as well.

While the theoretical prediction of linear behavior does not match the experimental data, the predictions of the NPPB per algae and the scaling of the NPPB concentrations varying *N* or *f* are well within the error margin of the model. To get an idea about the order of magnitude for this error, we realize that we determined in Section 2.2.2 that the algae surface charge density is on the order of $-10^{-3}$ C/m$^2$. Our range for the possible values of the charge density is approximately $-5 \pm 4 \times 10^{-3}$ C/m$^2$. Therefore, the measure of uncertainty in the algae surface charge density is on the order of $\pm 10^{-3}$ C/m$^2$ and we can include the order of the uncertainty in Eq. (4.3):

$$\frac{n_{NPPB}}{n_{alg}} = \frac{10}{Nf} \pm O(0.1) \qquad (4.4)$$

Recall that we also discussed how the theoretical NPPB per algae will underestimate the experimental data by an order of $10^3$ since we inherently do not consider the charges localized to a single brush. Also remember that in Section 3.11 we calculated the experimental range of NPPB per algae at 100% harvesting efficiency to be between 65 and 250. Adding $10^3$ to Eq. ( 4.4 ) places the theoretically determined NPPB per algae in Figure 4.2a at 100% harvesting efficiency within this range.

We can also resolve the order of the margin of error in the NPPB per algae ratios versus *N* and *f*. Let $x_i$ be the NPPB per algae for brush structure *i*. The error in the ratio $x_i/x_j = y$ is then given as the differential of *y* with respect to the error. The order of the margin of error between two NPPB per algae ratios at equal harvesting efficiencies follows as:

$$\epsilon = \frac{1}{x_1} O(0.1) - \frac{x_2}{x_1^2} O(0.1) \qquad (4.5)$$

where we have used the total differential for the error between For constant *N* and varying *f* the uncertainties, $\epsilon$, are ± 0.3 varying *f* from 0.25 to 0.5 and ± 0.4 varying *f* from 0.5

to 0.75 and from 0.75 to 1. For constant $f$ and varying $N$, the uncertainties are ± 0.2 varying $N$ from 50 to 100 and ± 0.3 varying $N$ from 100 to 200 or 200 to 250. The ratios are also in the range of error.

While we realize that this model serves as a straw man argument, the similarities to experimental data are suggestive. Qualitative comparisons can be made to understand the relationship between the harvesting efficiency and brush structure. If flocculation is the sole criteria for harvesting efficiency, theoretical results show that adding more charge per brush to the system leads to fewer NPPBs required for equal harvesting efficiencies. This is a result of screening the effective charge on the algae at a faster rate per NPPB added. Therefore, the experimental observations of harvesting efficiency possess a close dependence on the amount of algae surface charge screened per addition of an NPPB. This is supported by the results in Chapter 2 where we saw that the flocculation behavior of the algae should be electrostatic in origin.

We also observe that experimental plots in Figure 4.1 and Figure 4.2 have a close resemblance to the theoretical plots of harvesting efficiency. While experimental scaling of the NPPB concentration versus $f$ and $N$ is nonlinear, its behavior is not distant from the linear behavior predicted theoretically. This suggests that a modification in the theoretical assumptions of this model could lead to better agreement with experimental observations. If we included the effective range of the field emanating from the positively charged NPPB into the calculations, it is possible that this may lead to nonlinear behavior due to the scaling of the brush height. Recall that we determined the effective charge radius of a brush from the first moment of the polymer profile, or brush height, where all the charge was located at this position. This brush height is related to the brush length that scales in the polyelectrolyte regime as $\sim f^{1/2} N$. So as $f$ is increased, the brush height and effective charge radius increases as well. This may explain the experimental observation that the harvesting efficiency for $f$ = 0.75 resembles the results for $f$ = 1 much more than for $f$ = 0.5 even though the difference in charge is equal. As evident in Figure 3.7 and Figure 3.8 the change in the brush height and length is greater when increasing the charge fraction from 0.5 to 0.75 than from 0.75 to 1. Therefore the change in the NPPB effective charge radius would be less pronounced for the latter as compared to

the former. While the change in the amount of charge may be the same, the screening range at which this charge can be effective scales nonlinearly and by a lesser factor.

Yet this explanation is incomplete in that even for the longest brush structure, when $N = 250$ and $f = 1$, the effective charge radius of the NPPB is still much smaller than the radius of the algae. When the algae are flocculated, which physically signifies the formation of algae clusters, one brush can at most be felt by two algae. This suggests that making a NPPB such that its effective charge radius is on the scale of or greater than the algae radius could lead to larger harvesting efficiencies at equal NPPB number densities. Maximizing the charge fraction and diameter of the NPPB can do this. The charge fraction can be optimized by setting $f = 1$ and/or increasing the grafting density. Increasing the size of the nanoparticle core and/or the length of the brush by adding more monomers and/or increasing the charge fraction can increase the diameter of the NPPB. However, until the sum of the NPPB radius and the Debye length is on the order of 4 $\mu$m, at most one NPPB can only flocculate two algae.

### 4.2.2. Incorporating a NPPB Distribution of Coverage When Matching Charges

From Figure 4.1b and Figure 4.2b we observe that rate of change for higher experimental harvesting efficiencies begins to trail off as the coagulation agent concentration increases. This effect is more noticeable as $f$ and $N$ approach their minimum value. We hypothesize that this is a result of our assumption earlier where the algae were either coated evenly or that only a few algae were coated at a time. We can incorporate into our model in Section 4.2.1 a distribution function that more accurately depicts the probabilistic nature of an NPPB coating an algae surface. The decay in the rate of the change in harvesting efficiency versus the change in NPPB at higher harvesting efficiencies would be a result of the probabilistic nature of the distribution of the NPPB coated algae. From Section 4.2.1 we calculated a cutoff for the NPPB per algae required to induce flocculation. Since this distribution is not uniform, increasing the number of NPPB added to the system shifts the distribution so that more cells have an NPPB per algae value greater than the calculated cutoff threshold. Once higher harvesting efficiencies are reached, most of the cells already have reached this threshold and

the rate at which the number of algae pass this critical concentration as more agents are added decreases. This would help explain experimental results.

To test this hypothesis, we must derive the form of the probability distribution. We imagine an array of $M$ algae cells. After adding an NPPB to the system, an algae cell has a probability of $p = 1/M$ to have the NPPB adsorb to its surface and a $1 - p$ probability of it adsorbing to another algae. We assume that each addition of NPPB is independent. After adding $A$ NPPB, the probability that $k \leq A$ are adsorbed onto a particular algae surface is given by the Bernoulli distribution:

$$P_K(k) = \binom{A}{k} p^k (1-p)^{A-k} \qquad (4.6)$$

If we take $M$ to the thermodynamic limit the required $A$ and $p$ are extensive variables and scale to this limit as well, such that $A$ becomes infinitely large and $p$ becomes infinitely small. Eq. ( 4.6 ) is reduced to the Poisson Distribution:

$$P_K(k) = \frac{(Ap)^k}{k!} e^{-Ap} \qquad (4.7)$$

Integrating Eq. ( 4.7 ) with respect to $k$ from the cut off $k^*$ to infinity and normalizing it by the total area gives the percent of algae that have enough NPPB to flocculate and be harvested.

Figure 4.3 illustrates the theoretical model. When $Ap$ is small, the majority of the algae have less NPPB adsorbed to their surface than the threshold required for flocculation, $k^*$. The shaded region under the curve relative to the total area represents the percent harvesting efficiency. As more NPPB are added to the system, the threshold remains constant but the distribution shifts such that a greater percentage of the algae can be harvested. When the relative number of NPPB becomes 50,000 times greater, the majority of algae pass over $k^*$ and the harvesting efficiency reaches 100%. Note that the slope at $k^*$ decays as $Ap$ increases. As this slope approaches zero, the change in the percentage of algae that are harvested trails off to unity as the number of NPPB relative to the number of algae swells.

We can apply this model for the brush structure varying $f$ or $N$ and plot the harvesting efficiency versus the NPPB concentrations. In Figure 4.4 we calculate these

harvesting efficiencies varying the monomer charge fraction at constant $N = 250$. Figure 4.4a depicts the unscaled calculations for $f = 0.25$. It is evident from the curve that as harvesting efficiencies approach 100%, the rate of change of the percent of algae that are over the threshold diminishes rapidly. Figure 4.4b shows a semilog plot of the number of NPPB per algae for all the different charge fractions. The relationship between the different charge fractions and their NPPB concentration at equal harvesting efficiencies is maintained.

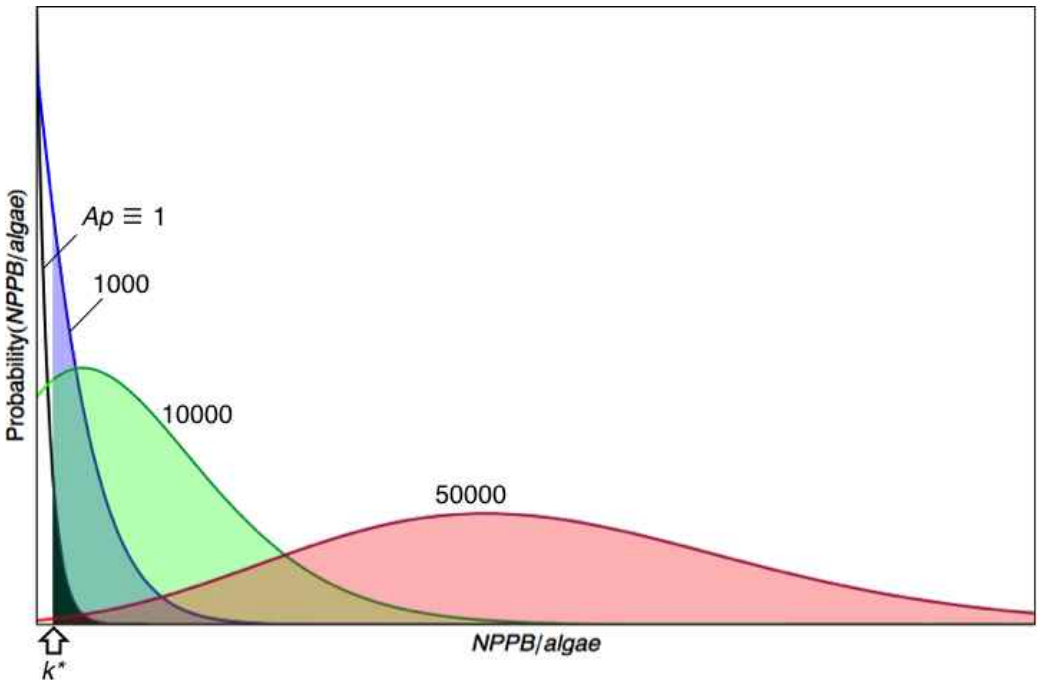


Figure 4.3. The Poisson distribution for the number of NPPB per algae varying the relative amount of NPPB added (*Ap*). The shaded area represents values for the given *Ap* that are above the flocculation threshold, *k**.

However, the rate at which this scaling behavior changes for a given monomer charge fraction varies. For each *f* the rate increases as the maximum value of the Poisson distribution for a given *Ap* approaches *k** for the different structures (0.043 for $f = 1$, 0.058 for $f = 0.75$, 0.086 for $f = 0.5$, and 0.172 for $f = 0.25$; see Figure 4.1). The rate then begins to tail off as the distribution becomes more spread out as the algae are saturated (see Figure 4.3). This results in a smaller percentage of algae that pass over the respective *k** for each increment in *Ap*. When this transition occurs, higher charge frac-

(a)

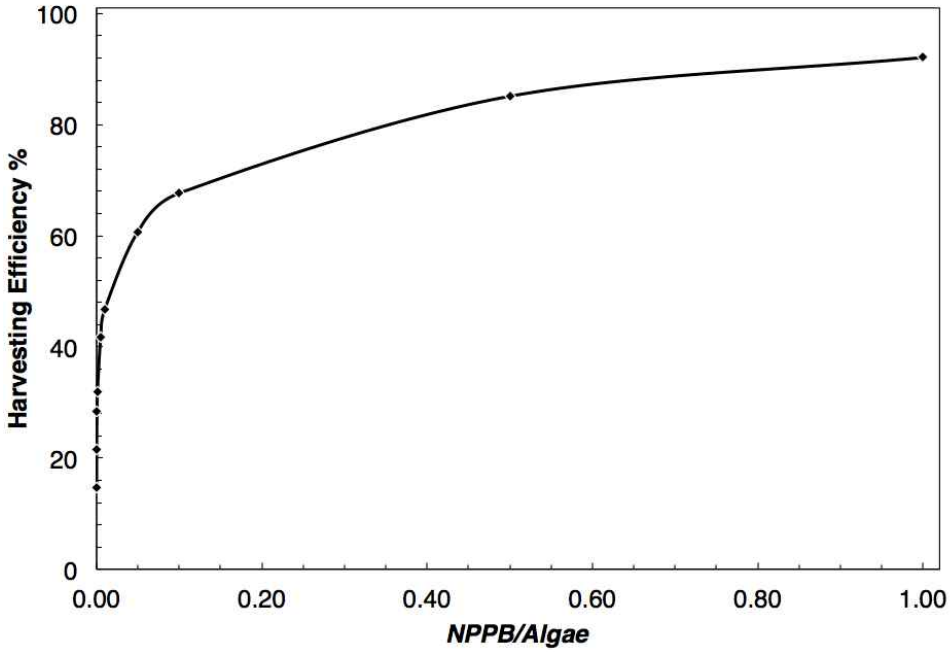


(b)

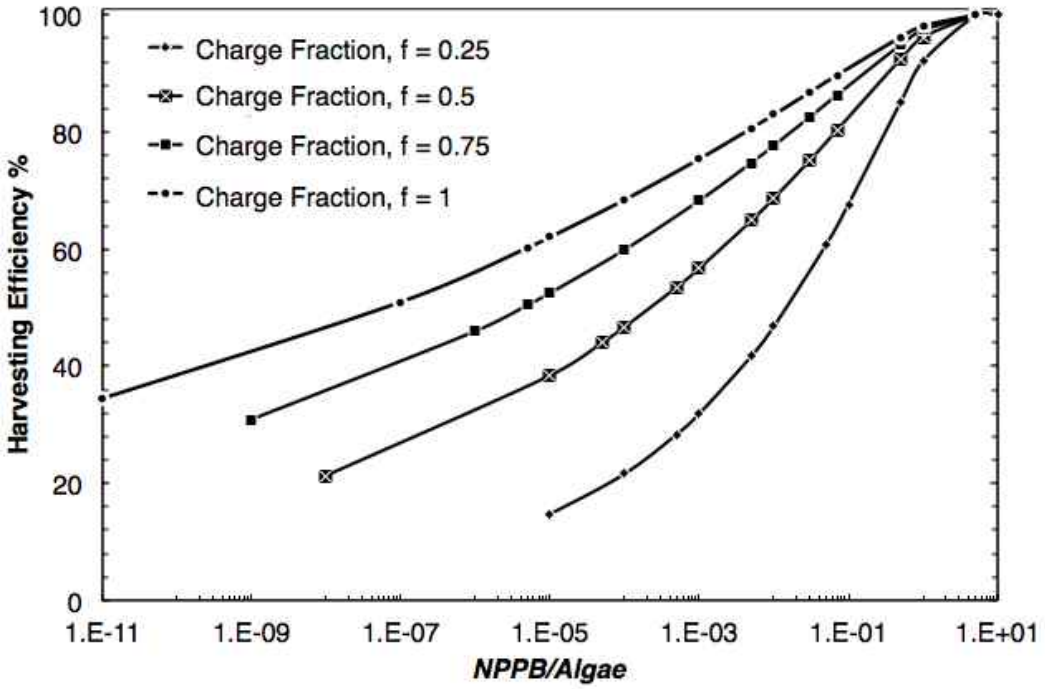


Figure 4.4. Harvesting efficiency as a percent versus the number NPPB added to the system divided by the total number of algae. Points represent results and line is a smooth curve fit to compare to experimental data representation. (a) Calculations for charge fraction = 0.25. (b) Calculations for all the charge fractions.

tions already have harvesting efficiencies close to 100%. At lower charge fractions, $k^*$ is smaller and higher NPPB concentrations are required to achieve equal harvesting efficiencies. Therefore while the rate for the change in harvesting efficiency with respect to the NPPC concentration for each $f$ diminishes, lower charge fractions have a greater percentage of algae still not flocculated at this transition. A similar observation is seen in experimental results in Figure 4.1a, where these rates fall off for the different $f$ at a similar NPPB concentration.

Since $N$ also scales linearly with the harvesting efficiency, similar behavior to Figure 4.4 should be observed. A simple inclusion of an NPPB probability distribution may serve to explain the experimentally observed tailing off of the harvesting efficiency phenomenon seen in both Figure 4.1b and Figure 4.2b. As the number of NPPB relative to the number of algae increases, the probability distribution approaches a more uniform spread and the rate of algae that pass over the threshold for the number of NPPB per algae required to induce flocculation and be harvested at the boundaries decays. For larger $N$ and $f$, the harvesting efficiencies are already close to 100% and the trail off phenomenon is not as persistent. However, it should be noted that the scaling behavior between the NPPB concentrations at equal harvesting efficiencies for the different $f$ is no longer linear as in Section 4.2.1. Increasing $f$ by a factor of 2 does not decrease the required NPPB for an equal harvesting efficiency by a factor of one half. This is a result of the non-uniform distribution of the NPPB on the algae surfaces.

While matching the number of charges led to some qualitative explanations of experimental behavior, we can improve on this model by considering the actual structure of the brush. Using the free energies of interaction determined by SCFT, the charges are physically localized along the polymer chain. Furthermore, we did not determine how the brush structure is able to form a floc of algae other than in terms of the effective charge on the algae surface. Yet we saw that the range of the electrostatic charges limit the interaction between the NPPB and other algae. In the next model, we include these physical behaviors.

4.3. Determining Harvesting Efficiency Using the Free Energies

A multi-body interaction potential follows directly once all the pair potentials are calculated. It is evident from our preliminary studies that once a NPPB comes in close proximity to the algal surface an irreversible, energetically favorable complex forms between the two species. Our main interest though is the NPPB mediated aggregation of microalgae. Our hypothesis stated that the flocculation of algae mediated by the NPPB resulted from a screening of the repulsive double layer between the two algae surfaces. Therefore, the energy barrier preventing two algae from aggregating is lowered.

If we take two bare algae as a reference system, we can then coat each algae surface with a uniform density of NPPBs (see Figure 4.5). The force between the two bodies is then given as the sum of the force between the two algae, the two NPPB layers, and the NPPB layers with each of the algae. The force of each of the interactions can be determined from the free energies, $F$, of each of the interaction. The relationship is given as $Force = -\partial F/\partial D$. When the force becomes attractive (negative), the algae are able to flocculate. As we have already mentioned, if we assume any aggregation of algae is large enough to be pulled by the magnet, then the ability of algae to flocculate determines the harvesting efficiency. In this case, we are assuming each algae is coated evenly and with the same amount of NPPB.

Since we are mainly concerned with $D \ll R$, where $R$ is the radius of either the inner algae or the outer NPPB body, we can use the Derjaguin approximation to convert the energy per unit area $W(D)$ to the force between two spheres of radius $R_1$ and $R_2$:

$$Force = 2\pi\left(\frac{R_1 R_2}{R_1 + R_2}\right)W(D) \qquad (4.8)$$

Eq. ( 4.8 ) allows us to readily convert the algae – NPPB free energies of interaction to forces. These free energies are given in Section 3.10.

For the algae – algae interactions, the force can be found from the derivatives of the free energy expressions in Section 2.2 with respect to $D$. For the interaction between the NPPB layers, we place all the charge of the polymer on the interacting surface. This surface is defined as having a radius equal to the distance between the center of an adsorbed NPPB brush and the middle of the algae cell. Therefore it is the

sum of the algae and NPPB radius, and the surface separation *D* where the free energy of the adsorption interaction between an NPPB and algae is at a minimum (determined in Section 3.10). We will mainly be interested in the case of flocculation, i.e. distances where the surface separation between the two NPPB layers, $D_{PB\text{-}PB}$, is much less than the radius of curvature, $R_{PB}$ of the layer surface. The force between the two surfaces is given as [66]:

$$Force = 0.5\kappa R_{PB} Z e^{-\kappa D} \qquad (4.9)$$

where $Z = 64\pi\varepsilon(k_B T/e)^2 \tanh^2(e\sigma_c/4k_B T\kappa\varepsilon)$ and $\sigma_c$ is the surface charge density of the NPPB.

We can now determine the overall force of the interaction. For forces involving the uniform NPPB density coat, we multiply *W*(*D*) in Eq. ( 4.8 ) by a scalar *n* that gives the relative coverage of the NPPB. For instance, a value of *n* = 0.1 suggests that it is as if 10% of the algae surface is covered with NPPB, or more accurately that the number of NPPB about an infinitesimal algae surface area *dA* is 0.1. Therefore we can readily convert *n* to the number of NPPB per algae by asking the question, how many NPPB fit into a surface area equal to *n* × 100% of the algae surface area?

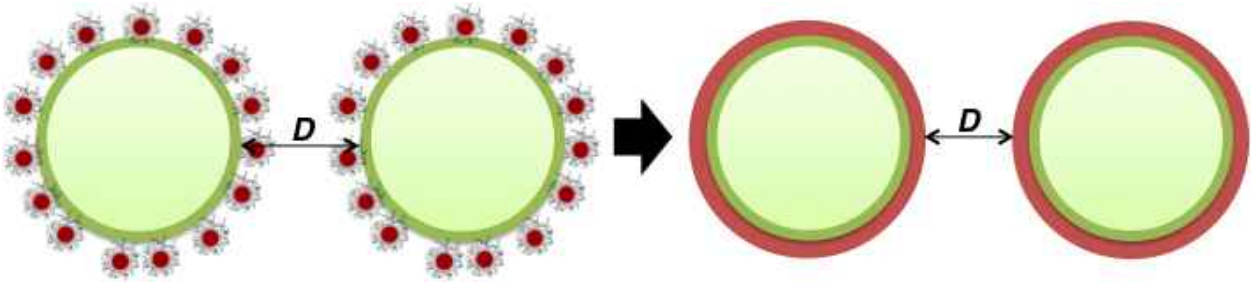


Figure 4.5. Coating two algae surfaces with NPPB.

Let us consider now when the two bodies depicted in Figure 4.5 are first able to flocculate, and therefore be harvested. We can imagine our bare algae cells as a reference. When the NPPB concentration is lower than the critical concentration required to induce flocculation, any amount of stirring would not cause two cells to “stick” to one another since the bridging between the NPPB layer on one algae with the surface of the other is not strong enough to outweigh the repulsion between the two algae cells and

NPPB layers. When the critical concentration is reached, there is enough NPPB such that the NPPB – algae force holding the two cells together offsets the repulsive forces pulling them apart. This occurs when the overall force of the NPPB – algae interaction first becomes attractive at some *D*. As we increase *n,* we can track the overall force for varying degree of polymerization *N* and monomer charge fraction *f* and determine when the interaction starts to become attractive.

### 4.3.1. Results for Varying Monomer Charge Density at Constant $N = 250$

First we will examine how the overall force changes for different brush structures as more charge is added for constant degree of polymerization, *N*. In Figure 4.6 we plot the lowest value of the total force between two coated algae cells (see Figure 4.5) to determine when the force becomes attractive for any of the possible *D* at a given *n*. This minimum happens to correspond to the lowest value of the free energy of interaction between an algae and an NPPB particle (see Section 3.10). At the edge of the plot when there is only one NPPB per algae cell, the repulsion between the similarly charged algae cells dominate the force. The slight variation of the value of the force for the different charge fractions arises from the different algae – algae separations determined by the *D* at which the force is at a minimum. As *n* approaches one, the NPPB begins to completely coat the surface and the minimum force starts to transition to the attractive regime.

The theoretically predicted NPPB per algae when this shift occurs is given in Figure 4.6, as well. They are on the order of the estimated experimental values. For instance, consider that in Section 3.11 we calculated that there should be approximately 55 NPPB per algae cell when the degree of polymerization experimentally was 250 when all the monomers were charged. This is in close agreement with the theoretically predicted value of 38. It is most likely that the latter underestimates the former considering that we are plotting when the interaction first becomes attractive at only one *D*. Several more NPPB must attach to the algae before the entire force becomes attractive. It should be mentioned, however, that the theoretically predicted value of NPPB per algae at the transition for monomer charge fraction equal to 0.25 overestimates the

experimental value. Recall that we estimated the mass of each NPPB to be around $7.21 \times 10^{-11}$ mg. When close to 100% of the algae are harvested, the experimental NPPB concentration is about 0.30 mg/mL (see Figure 4.1b). Thus, experiment concludes that there should be about 166 NPPB per algae for monomer charge fraction equal to 0.25 at degree of polymerization around 250. The large deviation between the experimental and theoretical value results from underestimating the NPPB – algae interaction for the given brush structure. As the monomer charge fraction decreases, theoretical results begin to overestimate experimental results by a greater factor. We propose this situation arises from an approximation in the theoretical framework where the charge is spread out evenly among the monomeric units. Rather than a fraction of the monomers along a single chain backbone having a full charge, each monomer was given a fraction of a full charge. Since only a small fraction of the monomers adsorb to the algae surface, the adsorption well may have been underestimated.

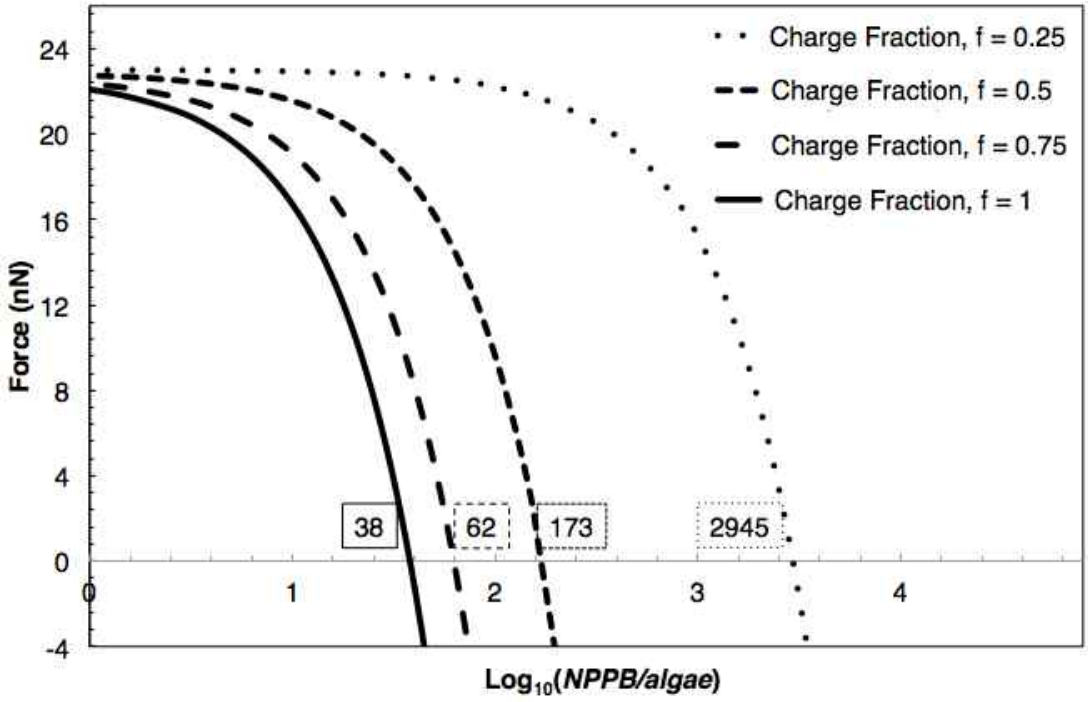


Figure 4.6. The minimum force in nano-Newtons versus the NPPB per algae varying the monomer charge fraction. The NPPB/algae are logarithmically plotted for comparison purposes. The numbers outlined by a box denote the un-scaled value for NPPB/algae when the force becomes attractive. The degree of polymerization is held constant at $N = 250$.

Nevertheless, taking into account the shape of the charge distribution along the polymer backbone as opposed to just considering the number of charges led to results more closely aligned with experimental data. Furthermore, the nonlinearity in the scaling of the NPPB per algae required with the charge fraction seen in experimental results (Figure 4.1b) is also evident in the theoretical findings. For instance, when the charge fraction is doubled from 0.25 to 0.5, the NPPB concentration required to reach an attractive minimum force is decreased by a factor of 0.059. When we double it again from 0.5 to 1, this factor is now 0.22. We see that as we approach a monomer charge fraction of one, the change in the NPPB required begins to diminish disproportionally to the charge fraction. Though not as pronounced as experimental data, a plateauing in the NPPB concentration is occurring between the different charge fractions as $f$ approaches unity.

In the previous discussion the interaction between two coated algae was either attractive or repulsive and served as a microcosm to the entire system. Since all the cells were coated evenly, either flocculation occurred between all the cells and there was 100% harvesting efficiency or the interaction was completely repulsive and none of the cells could be harvested. This gap in harvesting efficiency values can be filled in if we do not make the approximation that each algae always has the same number of NPPB. For example, putting in the first 1000 NPPB may go only to the first three algae cells they come across, and these cells can flocculate while the rest remain bare. From Figure 4.6 we know it takes 38 NPPB per algae for the minimum force to become negative for monomer charge fraction ($f$) equal to 1, 62 NPPB/algae for $f = 0.75$, 173 for $f = 0.5$, and 2945 for $f = 0.25$. Let us assume that as soon as the minimum of the force is attractive, the algae can aggregate. Then if we have four separate containers comprised of the same amount of algae and place 1000 NPPB for each of the $f$ in the different container, we should see 26 flocculated cells for $f = 1$, 16 for $f = 0.75$, 5 for $f = 0.5$, and none for $f = 0.25$. If only flocs can be harvested, then the harvesting efficiency is simply the number of flocculated algae divided by the total number that are present in each of these containers. We can put together a harvesting picture that will closely mimic experimental results. Figure 4.7 demonstrates what this would look like for a container with $25\times10^6$ algae cells (the same number in one mL of solution in lab set up). Since the

NPPB required per algae for $f = 1$ and 0.75 are on the magnitude, their harvesting efficiency profiles are similar.

Now that we have shown the behavior and scale of our theoretical predictions of the NPPB concentration and the harvesting efficiency for different monomer charge fractions has a resemblance to experimental data, we are in a position to explain how the brush structure influences that harvesting efficiency. The number of NPPB per algae required before the minimum of the total force becomes attractive is mainly dependent on the value of the algae pair interaction and the algae – NPPB interaction forces at the equivalent $D$ where this minimum occurs (it is not till too many NPPB are added when the NPPB – NPPB force has a roll). The values of these relevant parameters are summarized in Table 4.1.

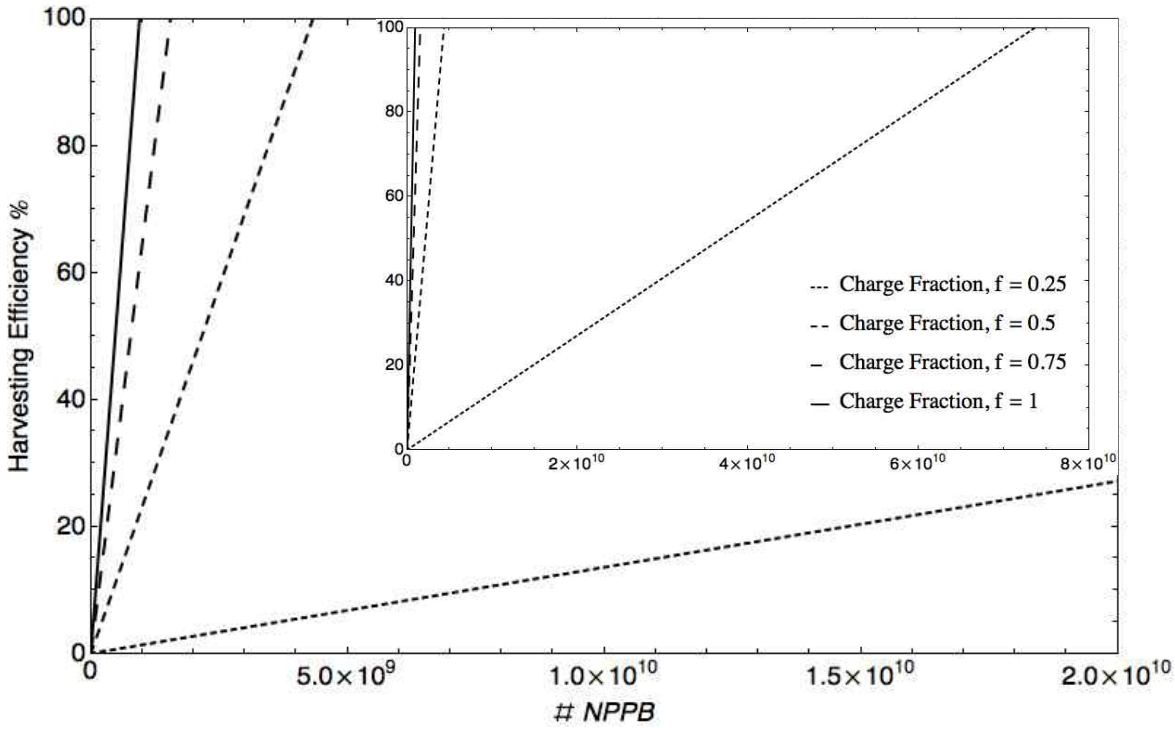


Figure 4.7. Theoretical harvesting efficiency versus the number of NPPB. Total number of algae cells = $25\times10^6$. Inset used to show entire range of harvesting efficiency versus number of NPPB.

Table 4.1 gives us more insight to the results in Figure 4.6 and Figure 4.7. Much more NPPB are required to induce flocculation between coated algae cells for $f = 0.25$ since the algae – NPPB force is much smaller compared to the other charge fractions.

This observation is compounded by the fact that the force between the two algae cells is greater for this charge fraction since the algae surface separation is much smaller. It is also clearer why the NPPB required for equal harvesting efficiencies for $f = 0.75$ is closer to the results for $f = 1$ than to $f = 0.5$. The relevant forces for $f = 0.75$ resemble the former more than the latter. Furthermore, if we used a collinear model where there is only one NPPB adsorbed between two algae, we observe from Table 4.1 that for $f$ greater than or equal to 0.5 the force from a bridging NPPB is enough to outweigh the algae repulsion force.

Table 4.1. Theoretical values when the total force of the interaction between coated NPPB is at a minimum for constant $N = 250$ varying the monomer charge fraction.

| $f$ | 0.25 | 0.5 | 0.75 | 1 |
|---|---|---|---|---|
| Algae Surface Separation (nm) | 475 | 496 | 531 | 538 |
| Algae – Algae Force (nN) | 23.01 | 22.88 | 22.72 | 22.68 |
| Algae – NPPB Force (nN) | -2.90 | -44.54 | -107.21 | -158.05 |

The foundation to these observations can be uncovered in the behavior of the brush length. Recall that the characteristic length of the brush in the polyelectrolyte regime scales as $\sim f^{1/2}$ and therefore changes at a rate proportional to $0.5f^{-1/2}$. As $f$ increases from 0.5 to 0.75, the characteristic length increases at a greater rate than when $f$ goes from 0.75 to 1. The effect is two-fold.

First, it has an effect on the adsorption well depth that determines the minimum algae – NPPB force via Eq. ( 4.8 ). Remember that the brush acts much like a spring (Section 1.3). The length of the polymer spring for $f = 0.75$ is closer to the length of the spring for $f = 1$ than for $f = 0.5$. However, the chain for $f = 0.75$ has less charge along the backbone than the chain for $f = 1$ meaning less coulombic repulsion between the monomer units and less osmotic pressure from the confined counter ions as the brush constricts. Therefore, the polymer brush can compress to a greater percentage of its original length before the elasticity of the chain begins to cause the interaction to be repulsive as compared to $f = 1$ (this is evident in Figure 9 from Section 3.10.1). This allows the chain for $f = 0.75$ to compensate for its lower charge fraction than $f = 1$ by being able to expose a greater percentage of its charge to the algae surface. While this compensa-

tion is not enough for the algae – NPPB force between the two structures to be equal, it causes the results to be more closely related. For $f$ = 0.25, the chain is only able to compress to roughly 10% of its original height before the minimum force is reached, much less than the other structures. This causes the depth of the algae – NPPB interaction adsorption well to be far less since its charge fraction is also lower.

Secondly, the brush length also affects the algae – algae separation. This separation is equal to the bridging length of an NPPB adsorbed onto both surfaces. As this gap approaches the Debye length, the repulsion between the two algae begins to diminish exponentially. The longer the brush, the closer this separation is to the Debye length. Once again, the value of the separation for $f$ = 0.75 is closer to the value for $f$ = 1 than for $f$ = 0.5 even though the difference in charge is the same because its brush length (and therefore bridging gap) is closer to the former.

### 4.3.2. Results for Varying $N$ at Constant Monomer Charge Fraction = 0.75

We can also examine how adding more monomers under constant charge fraction influences the total force between two coated algae cells. Figure 4.8 displays the value of the minimum total force at different values of NPPB per algae. When there are few NPPB on the algae surface, the repulsive force between the identically charged algae cells causes the total force to be repulsive as well. As more NPPB coat the surface, the adsorption of the NPPB layer onto the adjacent algae wall becomes stronger, prompting the value of the minimum of the total force for some $D$ to be attractive.

Figure 4.8 also provides the number of NPPB required to coat the algae surface when this transition occurs. Since we are dealing with a higher charge fraction where each monomer has a valency of 0.75, we do not expect the overestimation of the NPPB concentration required for this critical shift of the total force as described earlier for the case where $f$ = 0.25. Instead, it is more probable that this concentration is slightly underestimated since the NPPB number per algae when this transition occurs signifies when the very minimum of the total force first becomes attractive. From Figure 4.1b we observe that the NPPB per algae for $N$ = 250 and $f$ = 0.75 should have an analogous value to the ratio for $N$ = 250 and $f$ = 1, which we approximated as 55 NPPB per algae.

This number is in close proximity to the theoretical prediction of 62 NPPB per algae for the minimum force to become negative. However, as *N* is decreased this correlation between experimental and theoretical data starts to fade. For instance, Figure 4.2b shows that the nanoparticle concentration for close to 100% harvesting efficiency when $N = 65$ should be around $2.1\times10^{10}$ No./mL. If we take the algae density again to be around $25\times10^{6}$ No./mL, the NPPB required per algae is about 840. Since experimentally and theoretically the NPPB concentration for equal harvesting is inversely related to the degree of polymerization, we expect that as *N* approaches 50 the NPPB per algae should approach and exceed 840. While the NPPB per algae as *N* approaches 50 are around the same order of magnitude, the number underestimates experimental data by a factor of 2. More investigation is required to explain this phenomenon.

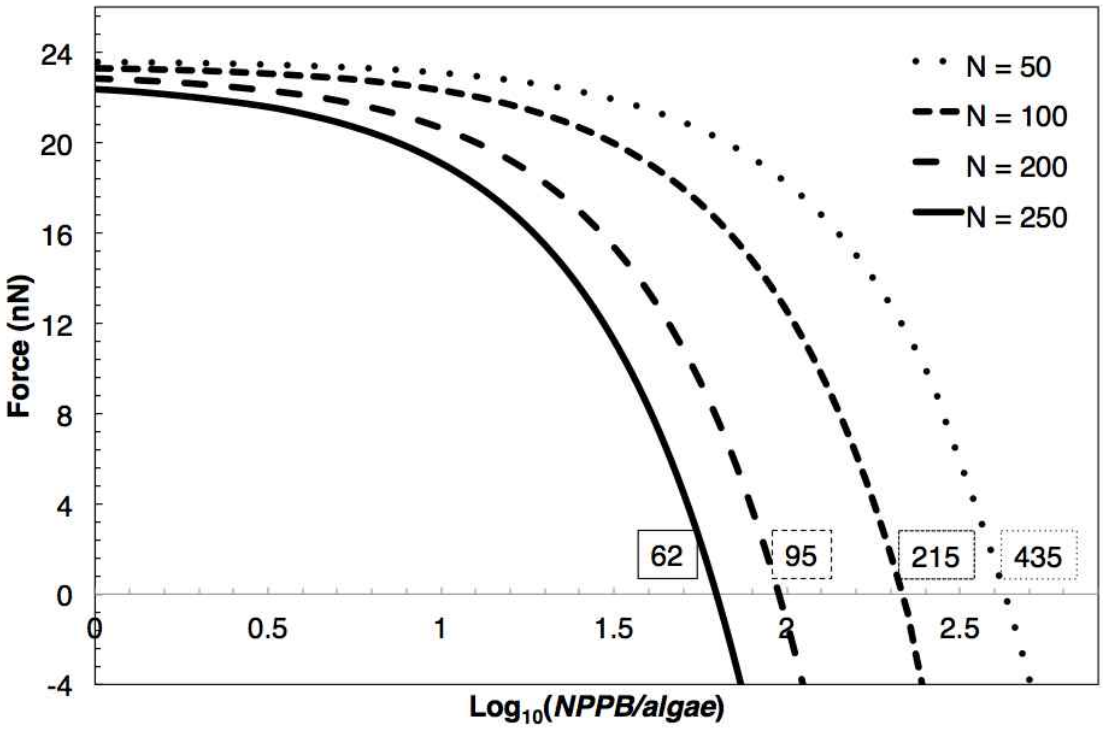


Figure 4.8. The minimum force in nano-Newtons versus the NPPB per algae varying the degree of polymerization *N*. The NPPB/algae are logarithmically plotted for comparison purposes. The numbers outlined by a box denote the un-scaled value for NPPB/algae when the force becomes attractive. The monomer charge fraction is held constant at 0.75.

The NPPB per algae required scales nonlinearly with the degree of polymerization, though the effect is less pronounced then for changing the monomer charge fraction at constant $N$. When the number of monomers is doubled from 50 to 100, the NPPB per algae required for the minimum force to become attractive halves. However, when $N$ is doubled again from 100 to 200 the NPPB per algae decreases by a factor of 0.44. Finally, as $N$ is increased by a factor of 1.25 from 200 to 250, the NPPB concentration decreases by a factor of 0.65. From these results we observe that as $N$ is increased by some factor $x$, the NPPB per algae required is reduced by a larger factor $y$. We can write this expression more explicitly as: $x < 1/y$ as $N \rightarrow 250$. This inequality becomes more disproportionately weighted toward $1/y$ as $N \rightarrow 250$. The rate at which the NPPB required decreases is greater than the rate at which $N$ increases. Physically this corresponds to obtaining the same harvesting efficiency for much less NPPB when one monomer is added to $N = 200$ than when it is added to $N = 50$. As $N$ approaches 250 this effect is more prominent. There is some basis to this theoretical outcome in experimental results. In Figure 4.2b, we can qualitatively see the comparison. As $N$ is approximately doubled from 65 to 124, the change in the nanoparticle concentration is much less than when $N$ is doubled again from 124 to 245. The rate at which $N$ increases is less than the rate at which the NPPB concentration decreases in this case. A similar conclusion can be drawn when comparing the scaling of the NPPB concentration between $N = 124$ and 198.

Like in Figure 4.7 we can provide a plot of the harvesting efficiency for different $N$ if we assume that once a floc of algae is created it can be harvested. Placing $25\times10^6$ algae cells in four separate containers, Figure 4.9 gives the harvesting efficiency as the NPPB is increased for each of the different brush structures. This diagram should be directly compared to Figure 4.2b. As in experimental results, the harvesting efficiency for $N = 200$ more closely resembles the results for $N = 250$ than for $N = 100$. This is due to the fact that adding 50 monomers to each chain for $N = 200$ is a much smaller difference than subtracting 100 monomers from each chain. Therefore the physical difference between the number of monomers for $N = 200$ and 250 is minor compared to the difference between $N = 100$ and 200. The relationship between the other brush structures at

different harvesting efficiencies emulates the theoretical scaling between *N* and the NPPB per algae at the minimum force discussed previously.

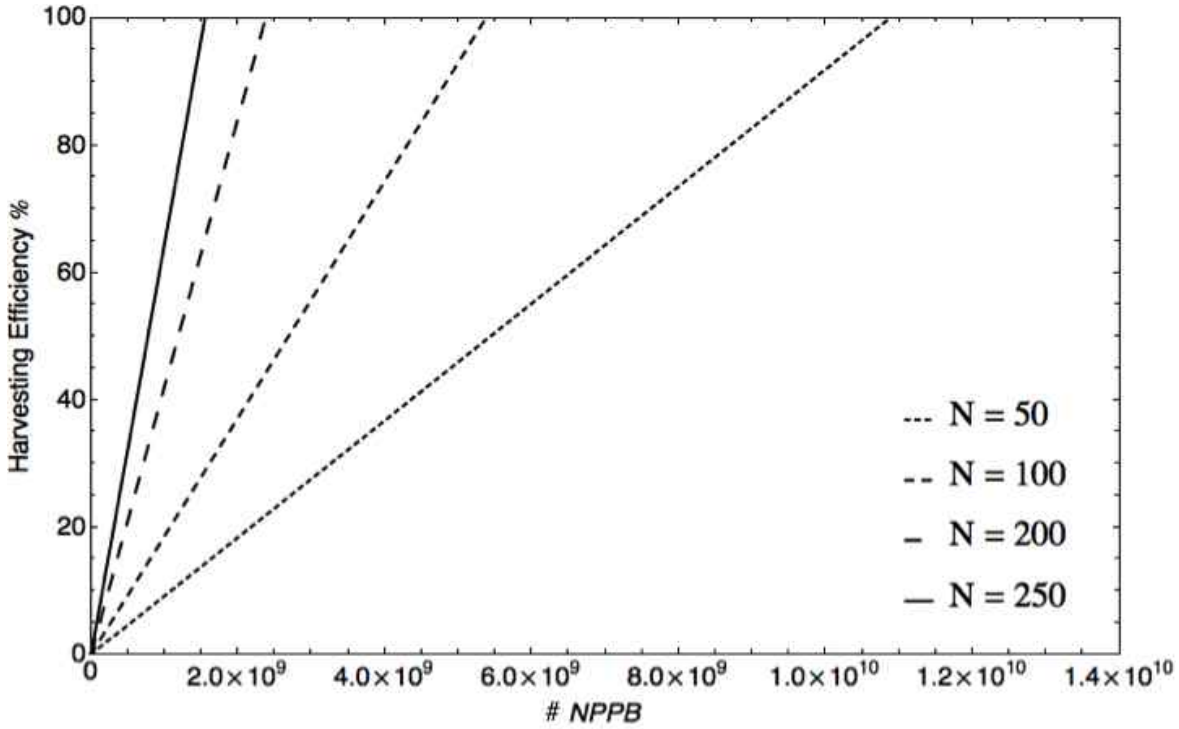


Figure 4.9. Theoretical harvesting efficiency versus the number of NPPB for different *N*.

Now that the theoretical and experimental results have been compared, we set out to uncover the fundamental physics that defines these observations. More specifically we want to explain the relationship between the brush structure and the harvesting efficiency. As before, the transition where the minimum of the total force becomes attractive is defined by the value of the algae pair and algae – NPPB interaction forces at the equivalent *D* where this minimum occurs. The value of the relevant parameters are presented in Table 4.2. See Section 3.10.2 for SCFT results depicting the depth and position of the adsorption well that determines the algae surface separation and algae – NPPB force at the total force minimum.

From Table 4.2 it is evident that the nonlinearity between the scaling of the NPPB concentration between the different degrees of polymerization is a product of the exponential decay of the algae – algae force and not the algae – NPPB force at the minimum value. The algae – NPPB force, which corresponds to the free energy of interaction well

depth between the brush and the algae via Eq. ( 4.8 ), varies linearly with *N*. For instance, doubling the degree of polymerization from 50 to 100 results in a decrease in the algae – NPPB force by a factor of 1.7 (force at 100 divided by force at 50). This same factor is reproduced when the degree of polymerization is doubled again from 100 to 200. Therefore, increasing the number of monomers along the chain by the same factor regardless of the original *N* will decrease the algae – NPPB force at the minimum by an identical ratio.

Table 4.2. Theoretical values when the total force of the interaction between coated NPPB is at a minimum for constant charge fraction $f = 0.75$ varying *N*.

| *N* | 50 | 100 | 200 | 250 |
|---|---|---|---|---|
| Algae Surface Separation (nm) | 342 | 384 | 454 | 531 |
| Algae – Algae Force (nN) | 23.62 | 23.40 | 23.08 | 22.72 |
| Algae – NPPB Force (nN) | -32.02 | -53.57 | -90.96 | -107.21 |

The behavior of the length of the polymer brush in the polyelectrolyte regime is the root of this conduct. To understand this, let us again use the parallel of the brush to a spring. Consider spring "1" of length *L* and a spring "2-3" consisting of two of spring 1 hooked up in series (Figure 4.10). Placing an equal weight at the top of both produces a force *F* on both springs such that $F_{2\text{-}3} = F_2 = F_3 = F_1$ and the equilibrium displacement of spring 1 is equal to half the displacement for spring 2-3. In order for this to be true, the spring constant of spring 1, $k_1$, must be double $k_{2\text{-}3}$. Thus, it takes twice the amount of force to displace spring 1 by the same amount as spring 2-3. Now if our spring length *L* scales as $\sim N$, the force also scales as $\sim N$. If we replace the springs with the polymer brushes of different *N*, which are all of the same material and charge fraction, and exchange the mass with the approaching algae surface instead, the force at some displacement of the brush scales as $\sim N$, as well. For instance, doubling the degree of polymerization results in increasing the repulsive force counteracting the compression of the brush by a factor of $2C$ given equivalent displacements of the brushes from their equilibrium height. Here *C* is the brush length scaling constant associated with *N*. The algae – NPPB force is increased by a factor of $2C$ at each displacement, as well. Therefore when *N* is doubled from 50 to 100 the algae – NPPB force at the minimum is

decreased by the same factor as when *N* is doubled from 100 to 200 since the repulsive force of the compressed brush scales as ~ *N*. Less of the cationic monomers along the backbone are able to adsorb onto the negatively charged algae surface before the interaction becomes repulsive.

Since the NPPB – algae force scales linearly with *N*, it must be the algae pair interaction force that causes the nonlinear relationship between *N* and the value of the minimum of the total force and therefore the NPPB required per algae for flocculation to occur. This force decreases exponentially as $e^{-\kappa D_{alg-alg}}$, where $1/\kappa$ is the Debye length and $D_{alg\text{-}alg}$ is the algae – algae surface separation. Recall that the minimum of the total force results from bridging of the two algae cells by the NPPB layer. Since the brush length scales as ~ *N*, this bridging gap approaches the Debye length as *N* increases and the total force falls off exponentially. This causes the nonlinearity between *N* and the minimum of the total force.

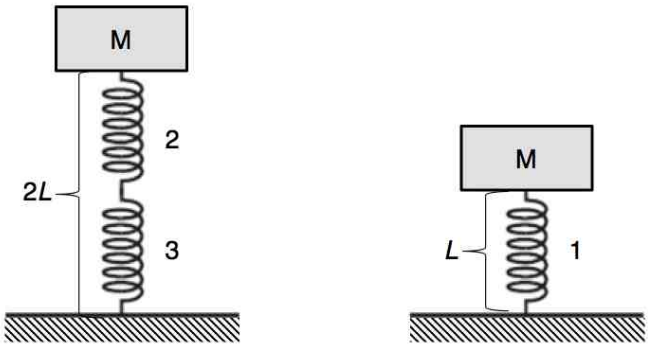


Figure 4.10. Depiction of spring 1 and two spring 1 hooked up in series with a mass *M* placed on top of both.

4.4. Comparing Theoretical Models

The discussion has surrounded the predictions of the scaling behavior of the NPPB concentration at equal harvesting efficiencies varying *f* and *N*. It would be useful to visually compare how the scaling behavior for these variables using the different theoretical models presented in Section 4.2.1 (termed Matching Charge, or MC Theory) and Section 4.3 (termed Free Energy, or FE Theory) relate to one another and to experimental data. For experimental data, we can use the NPPB concentrations depicted in Figure 4.1b and Figure 4.2b at approximately 100% harvesting efficiencies. As *f* varies

from 0.75 to 1 and as $N$ varies from 198 to 245, the NPPB concentrations are considered identical at equal harvesting efficiencies. For the experimental data varying $N$, the NPPB concentration at 95% harvesting efficiency will be used since not all studied $N$ reach 100% harvesting efficiency.

Before the NPPB concentrations at varying $N$ are studied though, we examine the NPPB concentrations at 100% harvesting efficiency for the two theoretical models and experimental results varying $f$. In Figure 4.11 the normalized NPPB concentrations are plotted for the different monomer charge fractions. Since the NPPB concentrations are normalized by the maximum value in the set, each of the three different series has a value of unity at $f = 0.25$. The error bars represent the order of absolute uncertainty discussed earlier for MC Theory. While these error bars show the possible variation in the NPPB concentration for MC Theory, it should be noted that they have a common error factor such that the scaling behavior would still remain linear with respect to $f$. Finally, we mention that while the scales of the normalized NPPB concentrations may not match up, the important piece of information to gather is the magnitude of the change in the dependent variable as $f$ varies.

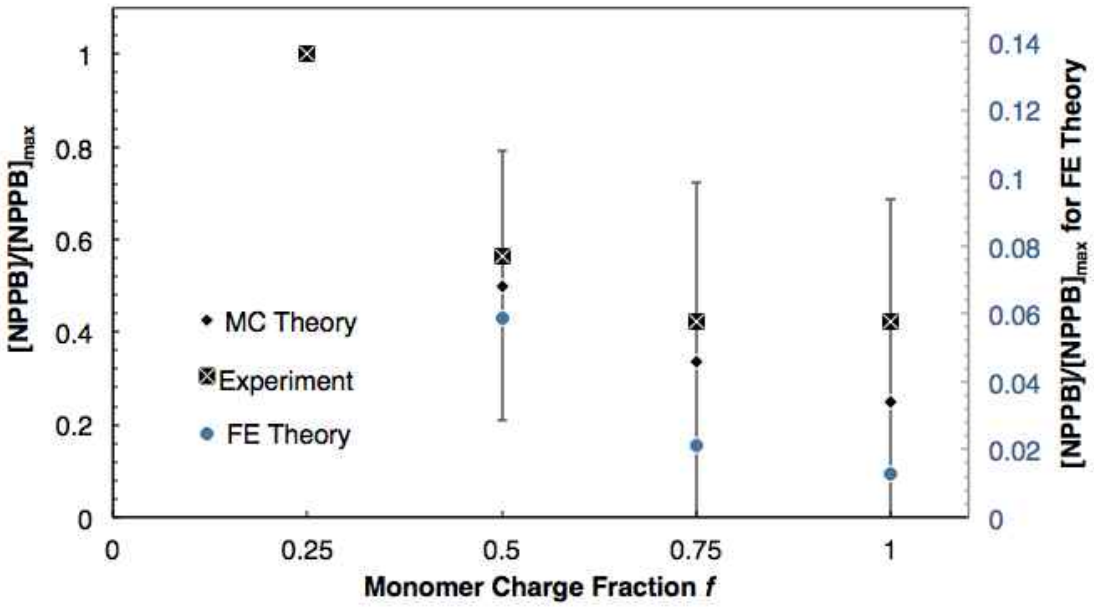


Figure 4.11. NPPB concentration normalized by the maximum value in the set for varying $f$. MC Theory data represents the model in Section 4.2 and includes the order of the margin of error denoted by the error bars. FE Theory data is graphed on the secondary axis (blue) and represents the model in Section 4.3.

MC Theory shows better scaling agreement with experiment for the scaling of *f* between 0.25 and 0.75, but FE Theory gives more accurate results for the scaling of *f* from 0.75 to 1. Despite the FE Theory sharing nonlinear scaling behavior with experimental results with respect to *f*, the predicted slope is too steep for the change in the NPPB concentration as *f* increases from 0.25 to 0.5 and from 0.5 to 0.75. We discussed previously that this may attributed to an error in lower charge fraction states arising from distributing the charge evenly between monomers, diluting the electrostatic relaxation of the free energy that occurs as opposite charges come in close proximity in the same layer. We also assumed that even coating occurs. The lower charge fractions may be able to be in closer proximity to one another, meaning that a disproportionate amount could be localized between algae surfaces where they can lower their overall free energy by forming a bridge between two algae surfaces rather than with just one. The significance of these two assumptions diminishes as we reach higher charge fraction when *f* increases from 0.75 to 1. FE Theory accurately predicts that the slope begins to level off as the algae – NPPB binding force becomes much greater than the repulsion between the algae (ref Table 4.1) and the behavior of the brush for $f = 0.75$ is much closer to the brush with $f = 1$ than to $f = 0.5$.

The relationship between the scaling behavior of MC Theory and experimental results also demonstrates that even the linear slope over predicts the change in NPPB varying *f* at equal harvesting efficiencies. As *f* increases from 0.25 to 0.5 and from 0.5 to 0.75, the net effect still results in a decrease in the NPPB required. However, the rate at which this change happens is still less than the case where adding an NPPB to the system was equivalent to adding a number of charges. We discussed that unless the effective charge radius around a NPPB is greater than the radius of the algae, the number of cells one NPPB can at most aggregate is two. So while adding more charge may increase the binding force created by a bridging interaction between algae – NPPB – algae, incorporated in FE Theory, the number of algae one NPPB can aggregate is still only two. Then as *f* increases from 0.75 to 1 the NPPB – algae binding force has already reached a threshold where it is sufficient in both structures such that very few

NPPB are required to attract and bridge two algae, as predicted by FE Theory. Yet only two can be bridged, leading to zero slope in the scaling of the experimental results.

Next we look at the scaling of the normalized NPPB concentration to the degree of polymerization, *N*. Figure 4.12 illustrates the normalized NPPB varying the degree of polymerization for both theoretical models and the experimental results. The similarity between the results for the two theoretical models are to be expected since we already discussed that the algae – NPPB force scales linearly with *N*. The nonlinearity as *N* approaches 250 in FE Theory is a result of the decay of the algae – algae repulsion as the NPPB diameter approaches the Debye length. Once again the error bars represent the order of magnitude of the absolute uncertainty for MC Theory measurements.

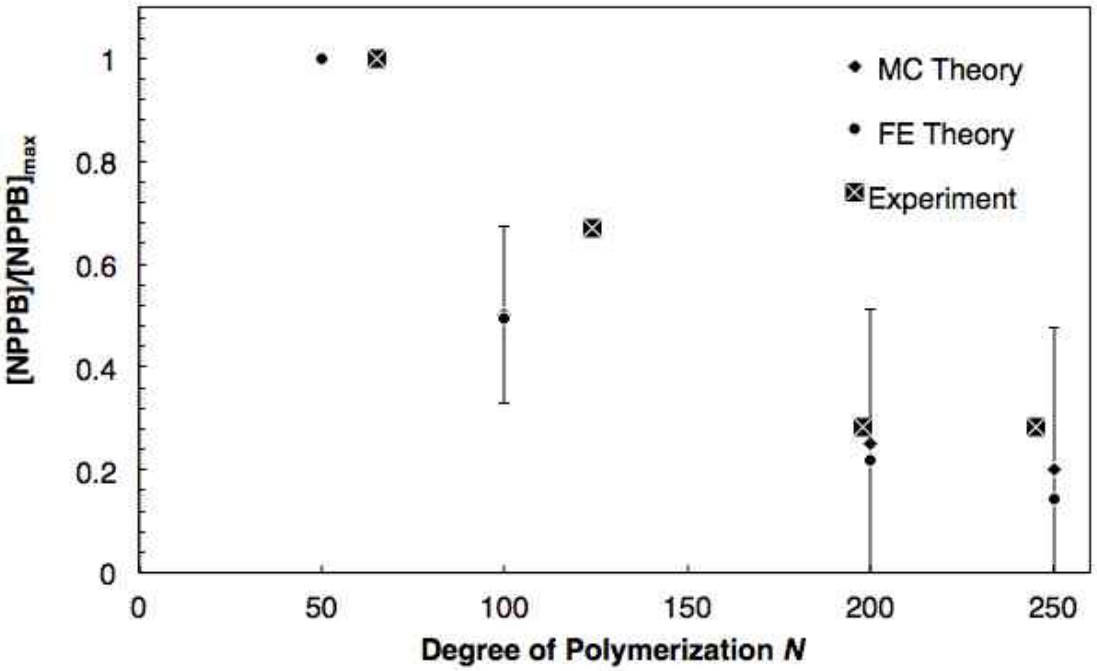


Figure 4.12. NPPB concentration normalized by the maximum value in the set for varying *N*.

The rate of change in the experimental results for the normalized NPPB concentration more closely mirrors the theoretical models than compared to the scaling for *f*. When the bridging gap, given in Table 4.2, is still only about one third of the Debye length the rate of the algae – algae repulsion does not fall off as quickly as the linear decrease of the NPPB – algae attraction. However, once this gap begins to approach the characteristic range of decay for the algae – algae repulsion from *N* = 124 to 198

experimentally and from 100 to 200 in FE Theory, the slope falls off quicker. Once again, we observe a threshold where the slope from $N = 198$ to 245 is zero. In the scope of MC Theory, where the magnitude of the slope also falls off, we see that this could be a result in the small difference in the extra amount of charge added to the system as $N$ increases from 200 to 250. Using FE Theory, we argue that a threshold is reached where the algae – NPPB force is sufficient enough at these bridging gaps where once again only a very few are required to induce flocculation and the harvesting efficiency is limited by the fact that one NPPB can at most aggregate two algae.

## 4.4. Conclusions

It is evident from the above analysis that the behavior of the polymer brush for different polymer parameters has a direct influence on the harvesting efficiency. Optimization of the brush architecture will allow lower NPPB concentrations to reach higher harvesting efficiencies. First off, matching the charges of the NPPB and algae demonstrated that adding more charge per NPPB led to lower NPPB required for equal harvesting efficiencies. However, the influence of this charge is limited by the effective charge radius determined by the diameter of the NPPB and the Debye length. One NPPB can only flocculate (and therefore harvest) two algae. Stretching the effective charge radius past the radius of algae would allow more algae harvested per NPPB. This can be achieved through several means, including increasing the charge, the grafting density, the degree of polymerization, or the core radius. However, the approach of synthesizing and NPPB so that its size is on the order of several micrometers is impractical. We observed that very few NPPB are required per algae in Section 4.3 for most charge fractions and degree of polymerizations before the bridging force between two algae via a NPPB becomes attractive. Therefore only a few bridging points on an algae surface are needed before a large floc is formed. Since large NPPB particles would require a large amount of mass to synthesize, on a mass per volume concentration basis NPPB on the order several micrometers is wasteful.

Adjusting this model to include a probability distribution of coating algae with NPPB explained experimentally observed decays in the harvesting efficiency at certain

NPPB concentrations at some threshold. As the number of NPPB started to saturate the algae surfaces, the probability distribution approached uniformity. Once this began to happen, the rate at which algae passed the certain NPPB concentration threshold required to harvest them diminished for each of the brush structures at each increment of added NPPB. Higher $N$ and $f$ led to harvesting efficiencies closer to 100% at this transition, causing a less persistent trail off at higher harvesting efficiencies compared to lower $N$ and $f$. Optimization of the brush structure would lead to harvesting efficiencies close to 100% well before this transition.

One unrealistic piece of this model is that the number of NPPB per algae in the Poisson distribution is unbounded. In reality, there is some transition where the algae surface is covered with enough NPPB that addition of another one is energetically disallowed due to the like charge repulsion between two NPPB particles. Instead, a cap should be placed on the number of NPPB per algae allowed. A further discussion of possible solutions will be discussed in Chapter 5.

Using the free energies of interaction led to conclusions on the optimal charge fraction and degree of polymerization, as well. As $f$ is increased for constant $N$, the brush length scales as $\sim f^{1/2}$. The means that the brush length for $f = 0.75$ is much more similar to the brush length for $f = 1$ than $f = 0.5$. The brush for $f = 0.75$ is able to expose a greater percentage of its charge than for $f = 0.5$ since more of its cationic monomers are able to adsorb to the algae surface before the brush becomes too constrained. However, $f = 1$ was still able to expose more charge due to its greater monomer charge fraction. Also, the longer brush length for $f = 1$ resulted in a greater bridging gap between two algae cells at the total force minimum. For bridging to occur, less NPPB per algae are required to overcome the repulsive force between algae. Optimization requires greater monomer charge fractions, which would again suggest that increasing the grafting density would cause lower NPPB concentrations for equal harvesting efficiencies. As $N$ is increased for constant $f$, the brush length and the value of the algae – NPPB force at the minimum total force scaled as $\sim N$. Increasing $N$ should lead to higher harvesting efficiencies at lower NPPB concentrations. This effect should trail off when

the polymer free end to end brush diameter approaches the Debye length as the repulsive algae – algae force exponentially decays as $e^{-\kappa D_{alg-alg}}$.

# CHAPTER 5
# SUMMARY AND CONCLUSIONS

Our main goal was to find the relationships between the harvesting efficiencies and the brush structure. We have proposed some answers to this question in the previous chapter. Here we will summarize the results and recommend the optimized brush structures.

## 5.1. Summary of General Conclusions and Recommendations to Experiment

Biofuel derived from biomass has the potential to reduce our reliance on fossil fuels for energy. Microalgae serves as a promising source of biomass for many reasons, including its ability to grow quickly and in non-arable land, to contain high lipid content by weight, and to produce high value derivatives that can offset the cost of the final fuel product. However, a major hurdle that is keeping microalgal biofuel from being cost competitive with petroleum-based fuels is the energy intensive and expensive dewatering step required to concentrate the naturally dilute cultures of microalgae before lipid harvesting.

Due to their low specific mass, small cell size, and negatively charged surfaces, microalgae form a stable suspension in solution. Sedimentation and filtration are not feasible for a continuous cycle industrial process. Centrifugation is only economically realistic at lab scales. Flocculation is one method that has garnered more attention recently in concentrating algae cells so that they can be dewatered. The flocculation agent is generally synthesized out of readily available materials and can perform quick and efficient concentration of algae cells. However, this flocculation agent must eventually be separated from the harvested algae cells in order to avoid downstream contamination of the final fuel product. Furthermore, recyclability of the flocculation agent would help drive down the cost of harvesting, as well.

Our experimental collaborators have developed a flocculation agent that inexpensively and efficiently leads to high harvesting efficiencies of algae and solves the problems associated with flocculation. It is both recyclable and is able to be separated from the aggregated microalgae cells once it is no longer needed. The flocculation agent is a cationic polymer brush with a paramagnetic nanoparticle core. An in depth theoretical study was conducted in order to understand how certain structural parameters of this nanoparticle polymer polyelectrolyte brush (NPPB) influence the harvesting efficiency.

Once the natures of all the pair interactions between the relevant bodies in the system were determined, various models were employed to model harvesting efficiency. The first method involved in determining when the effective charge, the charge that produces the electrostatic field felt by another algae, was completely screened. We observed in Chapter 2 that the repulsion between two similarly charged algae cells was a result of the strong electrostatic double layer repulsion at most surface separations. Negating the effective charge on an algae cell through cationic charge screening between the two surfaces would eliminate the repulsion and allow microalgae to form clusters. When the NPPB is added to the system, the positively charged monomers along the chain backbone serve to screen the anionic effective charge on an algae surface by adsorbing onto the surface. In this model neglecting the Debye screening length, when the number of positive charges provided by the polymer equaled the number of negative charges on the algae surface, cells could flocculate since the effective charge was completely screened in the model. Making the assumption that any size cluster of algae cells had enough NPPB to be manipulated by the magnet, the percent of flocculated algae was able to be directly translated into a harvesting efficiency. We examined the effect that changing the degree of polymerization $N$ and the monomer charge fraction $f$ on the NPPB had on the harvesting efficiency. Since the number of positive charges in the system was directly proportional to either $N$ or $f$ when the other was held constant, the required NPPB concentration at an equal harvesting efficiency scaled linearly with $N$ or $f$ also. However, the experimental results showed a nonlinear scaling behavior when these two brush parameters were independently varied. We understood

the limitations of this model. In reality, adding one NPPB represented adding a certain amount of charge localized around a single particle. Therefore the effective screening range of one NPPB was limited by the Debye length and the size of the NPPB. This effective screening range was less than the algae radius, signifying that one NPPB could at most flocculate two algae. Furthermore, we determined that one algae could accommodate about 40 NPPB before their effective screening ranges intersected.

To model harvesting efficiency using the free energies calculated in Chapter 2 and Chapter 3, we used two bare algae as a reference and then coated both with a uniform density of NPPB. We could then determine the number of NPPB per algae required for the force between the two bodies to become attractive at some surface separation. When the force becomes attractive, the two algae are able to aggregate at this surface separation. Making the assumption that algae were not coated evenly, i.e. the first 100 NPPB may go only to the first two algae these NPPB come across, and that the number of NPPB in a cluster of algae cells was enough to feel the pull of the magnet led to a way to determine harvesting efficiencies versus the number of NPPB added to a system. The assumption that the algae are not evenly coated is based on the strong energy of adsorption between the NPPB and the algae surface, which is many times $k_BT$. An NPPB placed in the system would irreversibly adsorb to the first algae surface it comes in close proximity to. Therefore we expect this assumption to be closely related to physical reality. We then studied the effect that altering $N$ and $f$ had on the theoretical harvesting efficiency and compared this to experimental data.

The behavior of the polymer brush in response to independent variations in $N$ and $f$ influenced the scaling of the number of NPPB at equal harvesting efficiencies for the different brush structures. The algae surface separation when the force was at its minimum coincided with the situation when the polymer brush was adsorbed at its minimum free energy of interaction well depth onto both algae surfaces. The NPPB bridges the two algae particles. Therefore the value of the total force minimum versus the number of NPPB added to the system at the transition when the force becomes attractive was dependent on two parameters of the interaction. The first is the length of this bridging gap determining the force between the two similarly charged algae. The second is

the magnitude of the energy well depth that determined the strength of the algae – NPPB attraction. For constant *N* and varying *f*, the brush length scales as ~ $f^{½}$. Thus as *f* is increased, the length of the brush increases. This means that the bridging gap widens and the surface separation between the two algae cells begins to approach the Debye length, $1/\kappa$. The repulsive force falls off exponentially as $e^{-\kappa D_{alg-alg}}$, signifying that as the brush length causes the NPPB diameter to approach $1/\kappa$ when *f* is increased the total force decays proportional to this rate, as well. Since the brush length scales as ~ *N*, adding more monomeric units for constant *f* also produces a similar effect, but much more pronounced. For the algae – NPPB force, higher monomer charge fractions also resulted in greater sequestering of the algae charge on the surface and a higher binding energy. For constant *f* the algae – NPPB force scales linearly with *N* since the brush height scales as *N*. When understanding this effect in the context of springs, doubling the spring length means decreasing the necessary force required to displace the spring to an equal distance by one half. Therefore brushes with higher charge fractions and degree of polymerizations as *f* approaches one and *N* approaches 250 have lower (more attractive) NPPB – algae adsorption forces.

These observations lead to recommendations for the optimal brush structure. When the degree of polymerization results in a brush length such that the free polymer end-to-end diameter is less than the Debye length, higher charge fractions are needed to hold the bridged algae together in order to overcome the algae – algae repulsive force. However, if the degree of polymerization results in a brush such that this bridging gap is close to or greater than the Debye length lower charge fractions are required. This can be achieved by increasing the grafting density and/or increasing *f*. Since the monomer charge fraction is easy to control, the optimal brush structure would be one where *f* = 1 and the end-to-end brush diameter is close to or greater than the Debye length. This can be achieved by increasing the diameter of the nanoparticle core size and/or the degree of polymerization. Furthermore, we observed that unless the effective charge radius of an NPPB is larger than the radius of an algae cell, one NPPB can only flocculate two algae at most. Creating an NPPB that could bridge two algae and be large enough such that its effective charge radius was larger than the algae radius

would allow it to flocculate more than two algae cell at a time. This can also be done by increasing the diameter of the NPPB through increases in *N* or the core diameter. However, very few NPPB are required per algae in order for the bridging force of an NPPB to outweigh the repulsion between two algae surfaces as this gap distance. In fact, for most brush structures Table 4.1 and Table 4.2 demonstrate that the attraction of one NPPB is strong enough to hold two algae surfaces together. Large flocs can be formed through the bridging of only a several NPPB between algae surfaces. Therefore, a more efficient and economically feasible route for algae harvesting is to utilize smaller NPPBs rather than synthesize nanoparticles with dimensions of a few micrometers.

## 5.2. Future Work

So far we have been working off the hypothesis that harvesting efficiency is dependent on the number of algae cells that can form aggregates in solution. As a consequence, the capability to concentrate the cells has thus far been solely a result of the ability of the NPPBs to lower the energy barrier between algae. However, given the experimental harvesting set up, it is quite possible that the force of the magnet plays a role in the harvesting efficiency.

The methods outlined above predict whether clusters of algae and NPPB particles will form. In the proposed harvesting set up though, these clusters must be able to be manipulated by the external magnetic field. Magnetophoresis describes the movement of magnetically susceptible particles in a medium caused by a magnetic field gradient. The magnetophoretic force for our paramagnetic NPPB is proportional to the volume of the particle *V* and the applied field gradient via the following relationship:

$$F \sim V|\nabla B|^2$$

In order for clusters to be congregated by the magnet, we hypothesize that the magnetophoretic force must overcome the random Brownian forces dispersing the cluster. Only clusters large enough where this relationship holds will be harvested. Harvesting efficiency is now dependent on the ability of NPPB and algae to form clusters, the size of that cluster, and the number of NPPB in the cluster. How many NPPB per cluster are required could be elucidated. This might be tested experimentally by measuring harvest-

ing efficiency for different strength magnets.

We also mentioned previously that the theoretical NPPB required per algae to reach certain harvesting efficiencies does not correctly predict the correct experimental values in Section 4.3. The reason for the underestimated theoretical values with varying $N$ was unclear. More investigation is required to explain this difference. One possible avenue would be to use molecular simulations such as Monte Carlo or Molecular Dynamics to explicitly depict a system. A potential energy function between all the species has already been outlined in this document. One possible difficulty in Monte Carlo calculations is the lack of movement between clusters. Once a group of algae and NPPB form, the event may be so stable that there could be no movement among separate clusters. Moreover, irreversible binding may lead to slow equilibration and thus non-equilibrium behavior that is not captured by equilibrium Monte Carlo. Molecular dynamics automatically incorporates the ability of separate clusters to interact with one another, but could be difficult given the strengths of the attractions.

In Section 4.2, we discussed how the number of algae one NPPB can flocculate is limited to two. This is a result of the effective range of the electrostatic attraction of the NPPB to another algae being less than the dimension of an algae cell. Using SCFT, one could predict the degree of polymerization and the monomer charge fraction required to have the effective charge radius extend beyond the radius of an algae particle for different core diameters and salt concentrations. Then, a cost-benefit analysis could be done where the NPPB structure that minimizes the cost but still has an effective charge radius that extends beyond two flocculated algae radius could be determined. An NPPB with this structure could flocculate up to four algae. This could be compared to the cost of having a smaller NPPB with an effective charge radius less than the algae radius that can only flocculate two algae. The balance would be between the added amount of material for the former case between the larger amount of NPPB needed to be added in the latter.

A limitation of the free energy model for harvesting efficiencies in Section 4.3 was the assumption of even coating around the algae surface. As with the model in Section 4.2, an interesting addition to the model in 4.3 would be an inclusion of a distribution

function for the NPPB on an algae. However, this time it would be the distribution of a NPPB on the surface of one cell. For instance, we discussed how for lower monomer charge fractions a disproportionate amount could be localized at a position where they could form a bridge between two algae. This could possibly be completed using a Boltzmann factor where the reference location for the NPPB would be in a binding site where it did not electrostatically interact with other NPPBs. This may lead to more accurate predictions of the number of NPPB per algae to induce flocculation.

In a more general scope, examining the correct NPPB distribution between multiple algae could lead to a more accurate model as well. Recall in Section 4.2.2 where we introduced the Poisson distribution to account for the probabilistic nature of NPPB coating a large number of algae. The number of NPPB per algae did not have a maximum threshold, but was kept uncapped. A more realistic model would cap the number of available sites per algae. Once that threshold for a certain algae was reached, it could no longer take on any more NPPBs.

A possible threshold could be found from the number of NPPB effective charge areas that could fit on an algae surface. In Section 4.2 we mentioned that the effective charge area surrounding a NPPB was determined by the characteristic range of electrostatic forces in a medium, given as the Debye length. This suggested that a single algae surface had approximately 40 binding sites where an NPPB could adsorb and not feel any other NPPB. If any more NPPB were added they would interact with another NPPB on the surface and the electrostatic repulsion would make further binding energetically unfavorable. The cap could be set at the maximum number of these binding sites. The number of binding sites would be determined by the number of NPPB effective charge areas that could fit on an algae surface before they begin to overlap for a given $f$ or $N$. In order to determine the effective charge radius that governs the effective charge area, we could consider all the charge located at the first moment of distribution for the monomer volume fractions, given as the brush height. The effective radius would then be the radius of the NPPB core to the brush height plus the Debye length. The brush height for all the structures has already been determined in Section 3.10.

It is possible to link theoretically predicted harvesting efficiencies with the Bernoulli probability distribution using this cap. Now, instead of $A$ in Eq. ( 4.6 ) being the number of algae it becomes the number of possible binding sites on an algae surface. There is some total number of NPPB added to a given number of algae. The question then becomes: What is the probability that a given number of $k$ NPPB is/are adsorbed to an algae surface? We can use the results in Section 4.3 to determine how many NPPB are required on an algae surface before the bridging attraction provided by the NPPB is greater than the repulsion between two algae, given again as $k^*$. For instance, if the adsorption force from only one NPPB is more attractive than the algae pair repulsion, we could conclude that only one NPPB per algae are required before a bridging network begins to form. Once this network forms between algae cells, large enough flocs are created in order to be harvested. The harvesting efficiency is equal to the probability that an algae will posses the cutoff number of adsorbed NPPB required before flocculation occurs. It is possible that for low values of $k^*$ compared to the number of binding sites that the correction might not prove significant since the number of possible binding sites is much greater than the number currently filled.

For experimental results, we observed that there was little to no dependence on $f$ and $N$ once a certain threshold was reached. In our case, this corresponded to when $N$ was greater than 200 and $f$ greater than 0.75. When forming these bridging networks discussed above, we mentioned that for some structures only one NPPB is needed to bridge two algae cells since the algae – NPPB attractive force outweighs the algae – algae repulsion. Once a certain $f$ and/or $N$ is reached, the attractive force becomes greater than the repulsive force and a threshold is passed were addition of any more monomer units or charge along those units does not change the physical requirement of needing only one NPPB per algae to create a bridging network. This could explain the little to no dependence on $f$ and $N$ once $f > 0.75$ and $N > 200$. Theoretically we can investigate when this transition occurs.

A main source of uncertainty in our calculations was the surface charge density of the algae cell. In our current model, we backed out the surface charge from the zeta potential. However, instead of making several assumptions in order to perform this cal-

culation, the surface charge density could be a parameter determined from experiment. Recall that once we knew the surface charge density we could estimate the critical ionic strength when the algae – algae repulsion would be screened and flocculation could occur. We could reverse the process and design an experiment where an algae culture is titrated with 1:1 salt concentration. The critical ionic strength at which the majority of the algae begin to precipitate out of solution would then be recorded and the surface charge density could be determined using our current model.

Finally, in Figure 1.6a the experimental harvesting efficiencies using the NPPB were compared to harvesting efficiencies using free polymer. For the free polymer, after a coagulant concentration of approximately 0.2 mg/mL was reached the harvesting efficiency began to decrease upon the addition of any more coagulant agent. An investigation into the physical processes that govern the interaction between algae species and free polymer would lead to further information on the efficiency of the NPPB coagulation agent via a contrast with the free polymer. It is possible that since the free polymer is not grafted to a nanoparticle, its charge is not localized around a single point. Therefore, its effective charge area is much more spread out on a mg/mL basis. Adding more free polymer after a certain point would lead to repulsion between coated algae cells due to the similarly charge polymer adsorption layers, and flocs would begin to disband.

REFERENCES CITED

[1] World population prospects, the 2012 revision. *UN Department of Economic and Social Affairs*, **2013**. Retrieved October 1, 2014 from http://esa.un.org/wpp/.

[2] Smalley institute grand challenges. *Smalley Institute; Rice University*, **2008**. Retrieved October 1, 2014 from https://smalley.rice.edu/content.aspx?id=246.

[3] International energy outlook. *U.S. EIA*, **2014**. Retrieved October 1, 2014 from http://www.eia.gov/forecasts/ieo/.

[4] A. Pollack. White house promotes a bioeconomy. *NY Times*, **2012** (April 26). Retrieved October 2, 2014 http://www.nytimes.com/2012/04/26/business/energy-environment/white-house-promotes-a-bioeconomy.html?_r=0.

[5] J.A. Foley, N. Ramankutty, K.A. Brauman, E.S. Cassidy, J.S. Gerber, et al. Solutions for a cultivated planet. *Nature* **2011**, *478*, 337.

[6] R.H. Wijffels, M.J. Barbosa. An outlook on microalgal biofuels. *Science* **2010**, *329*, 796.

[7] Y. Chisti. Biodiesel from microalgae beats bioethanol. *Trends in Biotechnology* **2008**, *26*, 126.

[8] P.T. Pienkos, L. Laurens, A. Aden. Making biofuel from microalgae. *American Scientist* **2011**, *99*, 474.

[9] V.H. Smith, B.S.M. Sturm, F.J. deNoyelles, S.A. Billings. The ecology of algal biodiesel production. *Trends in Ecology and Evolution* **2010**, *25*, 301.

[10] J. Sheehan, T. Dunahay, J. Benemann, P.G. Roessler. *A look back at the U.S. Department of Energy's Aquatic Species Program – biodiesel from algae* **1999**. Report NREL/TP-580-24190, NREL, Golden, CO. Available at http://www.nrel.gov/docs/legosti/fy98/24190.pdf.

[11] The third generation: Algal fuel. (n.d.). In *Biofuels and Bioenergy*. Retrieved June 2, 2014, from http://refuelingthefuture.yolasite.com/third-generation-biofuels.php.

[12] S. Kumar, E. Hablot, J.L.G. Moscoso, W. Obeid, P.G. Hatcher, et al. Polyurethanes preparation using proteins obtained from microalgae. *J. Mater. Sci.* **2014**, *49*, 7824.

[13] F.B. Metting. Biodiversity and application of microalgae. *J. Ind. Microbiol.* **1996**, *17*, 477.

[14] Y. Chisti. Biodiesel from microalgae. *Biotechnology Advances* **2007**, *25*, 294.

[15] D.R. Georgianna, S.P. Mayfield. Exploiting diversity and synthetic biology for the production of algal biofuels. *Nature* **2012**, *488*, 329.

[16] C.Y. Chen, K.L. Yeh, R. Aisyah, D.J. Lee, J.S. Chang. Cultivation, photobioreactor design and harvesting of microalgae for biodiesel production: A critical review. *Bioresource Technology* **2011**, *102*, 71.

[17] X. Zhang, Z. Jiang, L. Chen, A. Chou, H. Yan, Y.Y. Zuo, X. Zhang. Influence of cell properties on rheological characterization of microalgae suspensions. *Bioresource Technology* **2013**, *139*, 209.

[18] N. Uduman, Y. Qi, M.K. Danquah, G.M. Forde, A. Hoadley. Dewatering of microalgal cultures: A major bottleneck to algae-based fuels. *J. Renewable Sustainable Energy* **2010**, *2*, 012701.

[19] D. Vandamme, I. Foubert, K. Muylaert. Flocculation as a low-cost method for harvesting microalgae for bulk biomass production. *Trends in Biotechnology* **2013**, *31*, 233.

[20] S. Salim, L. Gilissen, A. Rinzema, M.H. Vermue, R.H. Wijffels. Modeling microalgal flocculation and sedimentation. *Bioresource Technology* **2013**, *144*, 602.

[21] A. Schlesinger, D. Eisenstadt, A.B. Gil, H. Carmely, S. Einbinder, J. Gressel. Inexpensive, non-toxic flocculation of microalgae contradicts theories: Overcoming a major hurdle to bulk algal production. *Biotechnology Advances* **2012**, *30*, 1023.

[22] S. Sanyano, P. Chetpattananondh, S. Chongkhong. Coagulation-flocculation of marine *Chlorella sp*. for biodiesel production. *Bioresource Technology* **2013**, *147*, 471.

[23] L. Kuang, H. Liang. Manuscript in progress. **2014**.

[24] H. Deng, X.L. Li, Q. Peng, X. Wang, J.P. Chen, Y.D. Li. Monodisperse magnetic single-crystal ferrite microspheres. *Angewandte Chemie-International Edition* **2005***, 44*, 2782.

[25] T.K. Tam, J. Zhou, M. Pita, M. Ornatska, S. Minko, E. Katz. Biochemically controlled bioelectrocatalytic interface. *JACS* **2008***, 130*, 10888.

[26] B. Button, L.H. Cai, C. Ehre, D.B. Hill, J.K. Sheehan, R.C. Boucher, M. Rubinstein. A periciliarly brush promotes the lung health by separating the mucus layer from airway epithelia. *Science* **2012**, *337*, 937.

[27] D. Ding, K. Li, Z. Zhu, K.Y. Pu, Y. Hu, X, Jiang, B. Liu. Conjugated polyelectrolyte-cisplatin complex nanoparticles for simultaneous in vivo imaging and drug tracking. *Nanoscale* **2011**, *3*, 1997.

[28] M. Karg, S. Jaber, T. Hellweg, P. Mulvaney. Surface plasmon spectroscopy of gold-poly-N-isopropylacrylamide core-shell particles. *Langmuir* **2011**, *27*, 820.

[29] S. T. Milner. Polymer brushes. *Science* **1991**, *251*, 905.

[30] The term “polymer brushes” can be somewhat ambiguous in regards to the interface in which the brushes are attached. The term can be applied to polymers attached to the interface between two different mediums, as well. However, only solid interfaces will be considered.

[31] J. Lindqvist, D. Nystrom, E. Ostmark, P. Antoni, A. Carlmark, M. Johansson, A. Hult, E. Malmstrom. Intelligent dual-responsive cellulose surfaces via surface-initiated ATRP. *Biomacromolecules* **2008**, *9*, 2139.

[32] Y. Zou, J.N. Kizhakkedathu, D.E. Brooks. Surface modification of polyvinyl chloride sheets via growth of hydrophilic polymer brushes. *Macromolecules* **2009**, *42*, 3258.

[33] W.J. Yang, T. Cai, K.G. Neoh, E.T. Kang. Biomimetic anchors for antifouling and antibacterial polymer brushes on stainless steel. *Langmuir* **2011**, *27*, 7065.

[34] P. Pincus. Colloid stabilization with grafted polyelectrolytes. *Macromolecules* **1991**, *24*, 2912.

[35] The following treatment is true for most values of *f*. In a practical sense, it is only limited in the case when there is only one end charge present.

[36] D. Leckband, J. Israelachvili. Intermolecular forces in biology. *Quarterly Review of Biophysics* **2001**, *34*, 105.

[37] W.B. Russel, D.A. Saville, W.R. Schowalter. *Colloidal Dispersions*; Cambridge Univ. Press: Cambridge, MA, **1989**.

[38] E.H. Harris. *The Chlamydomonas Sourcebook, a Comprehensive Guide to Biology and Laboratory Use*; Academic Press, Inc.: San Diego, CA, **1989**.

[39] Zeta potential. (n.d.). In *Wikipedia*. Retreived August 1, 2014, from http://en.wikipedia.org/wiki/Zeta_potential.

[40] D. Vandamme, I. Foubert, K. Muylaert. Flocculation as a low-cost method for harvesting microalgae for bulk biomass production. *Trends in Biotechnology* **2013**, *31*, 233.

[41] B.V. Derjaguin, L. Landau. Theory on the stability of strongly charged lyophobic sols and of the adhesion of strongly charged particles in solutions of electrolytes. *Acta Physicochim. URSS*. **1941**, *14*, 633.

[42] E.J. Verwey, J.Th.G. Overbeek. *Theory of Stability of Lyophobic Colloids*; Elsevier: Amsterdam, **1948**.

[43] J. Israelachvili. *Intermolecular and Surface Forces* (3ed.): Elsevier: Amsterdam, **2011**.

[44] H. Hamaker. The London – van der Waals attraction between spherical particles. *Physica* **1937**, *4*, 1058.

[45] C. Likos. Effective interaction in soft condensed matter physics. *Phys. Reports* **2001**, *348*, 277.

[46] E.M. Lifshitz. The theory of molecular attractive forces between solids. *Soviet Phys. JETP* (*Engl. Transl.*) **1956**, *2*, 73.

[47] I.E. Dzyaloshinksii, E.M. Lifshitz, L.P. Pitaevskii. General theory of van der Waals forces. *Adv. Phys.* **1961**, *10*, 165.

[48] K. Roberts, M. Gurney-Smith, and G.J. Hills. Structure, composition, and morphogenesis of the cell wall of *Chlamydomonas reinhardi*. *J. Ultrastructure Research* **1972**, *40*, 599.

[49] J.P. Keener, J. Sneyd. Cellular homeostasis. *Mathematical Physiology*; Springer: New York, NY, **1998**.

[50] P. Somasundaran. Dielectrophoresis of biological cells. *Encyc. of Surface and Colloid Science* (2ed.); Taylor and Francis: New York, NY, **2006**.

[51] E. Lee, R.L. Heng, L. Pilon. Spectral properties of selected photosynthetic microalgae producing biofuels. *J of Quantitative Spectroscopy and Radiative Transfer* **2013**, *114*, 122.

[52] A.R. Denton. Effective interactions and volume energies in charge-stabilized colloidal suspensions. *J Phys.*: *Conden. Matter*. **1999**, *11*, 10061.

[53] M. Medina-Noyola, D.A. McQuarrie. On the interaction of spherical double layers. *J. Chem. Phys.* **1980**, *73*, 6279.

[54] D.S. Gorman, R.P. Levine. Cytochrome F and Plastocyanin: Their sequence in the photosynthetic electron transport chain of *Chlamydomonas reinhardi*. *PNAS* **1965**, *54*, 1665.

[55] D. Dougherty, D.R.D.A.C. Neta, R.F. McFeeters, S.R. Lubkin, F. Breidt, Jr. Semi-mechanistic partial buffer approach to modeling pH, the buffer properties, and the distribution of ionic species in complex solutions. *J. Agric. Food Chem.* **2006**, *54*, 6021.

[56] A.K. Dolan, S.F. Edwards. Theory of the stabilization of colloids by adsorbed polymer. *Proc. R. Soc. Lond. A* **1974,** *337*, 509.

[57] J.M.H.M. Scheutjens, G.J. Fleer. Statistical theory of the adsorbtion of interacting chain molecules. *Journal of Phys. Chem.* **1979***, 83*, 1619.

[58] P.J. Flory. *Principles of Polymer Chemistry*; Cornell University Press: Ithaca, NY, **1953**.

[59] O.A. Evers, J.M.H.M. Scheutjens, G.J. Fleer. Statistical thermodynamics of block copolymer adsorption. *Macromolecules* **1990**, *23*, 5221.

[60] P. Iakovlev. Core shell particles: Experiments and self-consistent field modeling. PhD Thesis, Agricultural University Wageningen, The Netherlands, **1992**.

[61] D.A. Knoll, D.E. Keyes. Jacobian-free Newton-Krylov methods: a survey of approaches and applications. *J. Comp. Phys.* **2004**, *193*, 357.

[62] C.T. Kelley. *Iterative Methods for Linear and Nonlinear Equations*; Society for Industrial and Applied Mathematics: Philadelphia, PA, **1995**. Accessed online at http://www.siam.org/books/textbooks/fr16_book.pdf.

[63] V. Eyert. A comparative study on methods for convergence acceleration of iterative vector sequences. *J. Comp. Phys.* **1996**, *124*, 271.

[64] C.M. Wijmans, J.M.H.M. Scheutjens, E.B. Zhulina. Self-Consistent field theories for polymer brushes. Lattice calculations and an asymptotic analytical description. *Macromolecules* **1992**, *25*, 2657.

[65] Iron(II,III) oxide. In *Sigma-Aldrich* **2014**. Retrieved August, 2014, from http://www.sigmaaldrich.com/catalog/product/aldrich/637106?lang=en&region=US.

[66] D. Leckband, J. Israelachvili. Intermolecular forces in biology. *Quarterly Reviews of Biophysics* **2001**, *34*, 105.